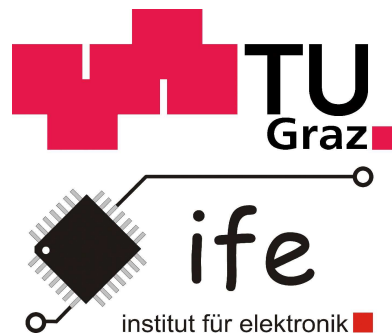


Improvement of the Operating Range of Electric and Hybrid Electric Vehicles



DI Christian Schuß

Institute of Electronics
Graz University of Technology

A thesis submitted for the degree of
Doctor of Engineering Sciences (Dr. techn.)

July 2014

Supervisors: Univ.-Prof. DI Dr. Wolfgang Pribyl,
Ass.-Prof. DI Dr. Bernd Eichberger

Statutory Declaration

I declare that I have authored this thesis independently, that I have not used other than the declared sources/resources and that I have explicitly marked all material which has been quoted either literally or by content from the used sources.

.....
(date)

.....
(signature)

Eidesstattliche Erklärung

Ich erkläre an Eides statt, dass ich die vorliegende Arbeit selbstständig verfasst, andere als die angegebenen Quellen/Hilfsmittel nicht benutzt und die den benutzten Quellen wörtlich und inhaltlich entnommenen Stellen als solche kenntlich gemacht habe.

Graz, am

.....
(Unterschrift)

Abstract

This thesis investigates opportunities to extend the electrical driving distance of battery-powered electric vehicles (BEVs) as well as hybrid electric vehicles (HEVs). The outcome of this research is to develop an electric range extender (ERE) which can be installed into these types of vehicles. The ERE consists of photovoltaic (PV) modules and a monitoring system.

Solar energy is considered as the most promising energy resource in the future, especially to substitute fossil energy resources such as oil, gas and coal. In conventional vehicles with internal combustion engines, all required electricity is produced with fossil fuels by alternators. It is worth noting that photovoltaics produce direct current (DC). If photovoltaics are integrated into the roofs of vehicles with high-voltage batteries like HEVs, the fuel consumption of these types of cars can be reduced. Similarly, in the case of BEVs the operating range can be extended.

Recently, HEVs have gained greater interest due to features such as regenerative braking and pure-electric propulsion. Hand in hand with the rise of functionalities, the amount of electronics has increased and so has the weight of modern automobiles. As a result, the required amount of fuel is still high, even though the latest technologies are used. This thesis discusses the opportunities to reduce rather than increase consumption levels with electronics.

Additionally, attention is paid how to control the photovoltaics which are deployed on the roof of BEVs and HEVs. In here, a monitoring system is used which provides information to the energy management system (EMS) of the vehicle about the output power level of PV modules. Since the area on vehicles for solar energy production is limited, the interconnection of PV cells is modified if unfavourable environmental conditions occur. Hence, the output performance of photovoltaics is optimised and a significant contribution to the required electricity of BEVs and HEVs is established.

The thesis' contributions are: the design, implementation and evaluation of an ERE to improve the performance of EVs and HEVs.

Keywords: automotive, consumption, energy, instrumentation, interconnection, photovoltaic, sensing, solar

Kurzfassung

Diese Dissertation behandelt verschiedene Möglichkeiten, wie die elektrische Reichweite von Elektrofahrzeugen als auch von Hybridfahrzeugen erhöht werden kann. Das Ergebnis dieser Forschung ist ein elektrischer Reichweitenverlängerer (ERE), welcher in Automobile installiert werden kann. Der ERE besteht aus Solarmodulen und Überwachungseinheiten.

Solarenergie gilt als die am vielversprechendsten erneuerbare Energiequelle für die Zukunft und gewinnt zunehmend an Interesse um den Verbrauch fossiler Energieträger wie Öl, Gas und Kohle zu reduzieren. In herkömmlichen Fahrzeugen mit Verbrennungsmotoren wird die gesamte elektrische Energie mit Hilfe von Lichtmaschinen und mittels Treibstoff produziert. Hier sind Solarzellen eine Überlegung wert, da mit ihnen direkt Strom erzeugt werden kann. Der Kraftstoffbedarf kann verringert werden, wenn Solarzellen in das Dach von Automobilen mit Hochvoltbatterien integriert werden. Hierbei, sind vor allem Hybridfahrzeuge besonders gut geeignet. Gleichmaßen, kann im Fall von Elektrofahrzeugen die elektrische Reichweite erhöht werden.

In jüngster Zeit ist das Interesse an Hybridfahrzeugen deutlich gestiegen. Der Grund für diesen Anstieg sind die vielfältigen Funktionen dieser Fahrzeuge wie zum Beispiel regeneratives Bremsen und rein-elektrisches Fahren. Hand in Hand mit dem Anstieg der Anzahl an Funktionen ist auch die Anzahl an Elektronik gestiegen, was somit eine Erhöhung des Gewichtes dieser Fahrzeuges zu Folge hatte. Infolgedessen ist der Kraftstoffbedarf noch immer hoch, auch wenn modernste Technik zum Einsatz kommt. Diese Dissertation behandelt Möglichkeiten wie mit Hilfe von Elektronik der Kraftstoffverbrauch reduziert anstatt erhöht werden kann.

Des Weiteren wird die Kontrolle und Steuerung der Solarzellen besprochen, welche am Dach von Elektro- und Hybridfahrzeugen angebracht werden können. In diesem Zusammenhang wird eine Überwachungseinheit verwendet, die wertvolle Information über die momentane, verfügbare Ausgangsleistung der Solarmodule an das Energiemanagementsystem (EMS) des Fahrzeuges liefert. Da der Platz an Dächern von Automobilen für die Produktion von Solarenergie begrenzt ist, wird die Zusammenschaltung der Solarzellen dynamisch verändert, im Speziellen wenn unvorteilhafte Wetterverhältnisse eintreten. Aus diesem Grund ist es möglich, das Ausgangsverhalten der Solarzellen zu optimieren und einen signifikanten Beitrag zu der benötigten elektrischen Energie in Elektro- und Hybridfahrzeugen zu leisten.

Das Ergebnis dieser Dissertation sind der Entwurf, die Implementierung und Evaluierung eines elektrischer Reichweitenverlängerers um die Leistung von Elektro- und Hybridfahrzeugen zu verbessern.

Schlüsselwörter: Abtastung, Automobil, Instrumentierung, Photovoltaik, Solarenergie, Verbindung, Verbrauch

Acknowledgements

This thesis is based on research work carried out at the Institute of Electronics in the Faculty of Electrical and Information Engineering, Graz University of Technology and at the Electronics Laboratory of the Faculty of Information Technology and Electrical Engineering, University of Oulu, during 2010–2014.

Firstly, I would like to express my deepest gratitude to both my thesis advisors, Prof. Wolfgang Pribyl (Joanneum Research) and Prof. Bernd Eichberger (Graz University of Technology), for the support, guidance and patience during these years. Thank you. My thanks also go to Prof. Timo Rahkonen (University of Oulu), Prof. Juha Kostamovaara (University of Oulu) and Dr. Antti Mäntyniemi (University of Oulu) for their help and feedback on my research studies. I would also like to thank all my co-workers for creating a pleasant working environment.

I wish to thank Prof. Erich Leitgeb (Graz University of Technology) for reviewing my thesis and for accepting the opponent role at my doctoral thesis defence, and Dr. Mark Jackson for revising the English of the manuscript.

Extending my gratitude to research partners, I would like to especially thank Harald Gall, Klaus Eberhart and Hannes Illko for the fruitful research cooperation and discussions. I would also like to thank all my former co-workers at ams AG.

This research was supported financially by Infotech Oulu Graduate School. Financial support has also been received from the following two foundations: Nokia Oyj:n Säätiö and Tauno Tönningin Säätiö. This research would have not been possible without their generous support.

I would like to mention my beloved father Gottfried (+2009) who introduced me to electronics a long time ago. He was the inspiration behind studying electronics. My thoughts also include my dear grandmother Hilda (+2014). Finally, I would like to thank and mention my family, my lovely fiancée Maija and my friends for their love, support and help throughout all the years.

Abbreviations

AGM	Absorbent Glass Mat
AUTOSAR ...	Automotive Open System Architecture
B-ISG	Belt-Driven Integrated Starter Generator
C-ISG	Crankshaft-mounted Integrated Starter Generator
CAN	Controller Area Network
CAN-B	Lowspeed-CAN
CAN-C	Highspeed-CAN
CMPPT	Current-Based Maximum Power Point Tracking
CPU	Central Processing Unit
DAQ	Data Acquisition
DC	Direct Current
DCA	Dynamic Charge Acceptance
DSP	Digital Signal Processor
DST	Daylight Saving Time
ECU	Electronic Control Unit
EMI	Electromagnetic Interference
EMS	Energy Management System
ERE	Electric Range Extender
ESC	Electronic Stability Control
BEV	Battery-Powered Electric Vehicle
EDR	Enhanced Data Rate
EU	European Union
GDP	Gross Domestic Product
HEV	Hybrid Electric Vehicle
ISG	Integrated Starter Generator
ISM	Industrial Scientific and Medical
ICE	Internal Combustion Engine
LIN	Local Interconnect Network
MCU	Microcontroller Unit

MOST	Media Oriented Systems Transport
MPP	Maximum Power Point
MPPT	Maximum Power Point Tracking
NIC	Network Interface Controller
NRZ	Non-Return To Zero
ODTB	On-Demand Top-Bottom
OSI	Open System Interconnection
P-HEV	Parallel Hybrid Electric Vehicle
PDM	Power Distribution Management
PSM	Power Supply Management
PV	Photovoltaic
RCP	Rapid Control Prototyping
S-HEV	Series Hybrid Electric Vehicle
S/P-HEV	Series-Parallel Hybrid Vehicle
SOC	State Of Charge
SOH	State Of Health
SOF	State Of Function
STC	Standard Test Conditions
TDE	Total Development Environment
VMPPT	Voltage-Based Maximum Power Point Tracking
WSN	Wireless Sensor Network

Contents

1	Introduction	1
1.1	Motivation for the Research	1
1.2	Research Scope and Methodology	3
1.3	Thesis Outline	4
1.3.1	Chapter 2 - Electrification of Automobiles	4
1.3.2	Chapter 3 - Principles of Photovoltaics	4
1.3.3	Chapter 4 - Electric Range Extender (ERE)	4
1.3.4	Chapter 5 and Chapter 6 - Discussion and Conclusion	4
2	Electrification of Automobiles	5
2.1	Amount of Electronics in Automobiles	5
2.2	Development of Automotive Electronics	6
2.3	Configuration of the Powertrain of Automobiles	7
2.3.1	Configuration and Classification of HEVs	7
2.3.2	Configuration of BEVs	11
2.3.3	Functionalities within the Powertrain	11
2.4	Energy Storage Devices in Electric and Hybrid Electric Vehicles	12
2.4.1	Storage Elements in BEVs and HEVs	12
2.4.2	Energy Management Systems of Automotive Batteries	13
2.5	Communication and Data Exchange in Automobiles	14
2.5.1	Bus Communication Systems	14
2.5.2	Controller Area Network (CAN)	14
2.5.3	Local Interconnect Network (LIN)	15
2.5.4	FlexRay-Bus	15
2.5.5	Media Oriented Systems Transport (MOST) Bus	16
2.5.6	Bluetooth	16
2.5.7	Load balancing within ECUs	16
2.5.8	Data Management in Real-Time Systems	17
3	Principles of Photovoltaics	19
3.1	Power Density of Energy Sources	19
3.2	Output Behaviour of Photovoltaics	19
3.3	Basic Structure of the Photovoltaic Energy Harvesting System	21
3.4	Maximum Power Point Tracking (MPPT) Algorithms	22
3.4.1	Examples for MPPT Techniques	22
3.4.2	Perturb and Observe (P&O) Algorithm	22
3.4.3	Voltage-based MPPT (VMPPT) and Current-based MPPT (CMPPT)	23
3.4.4	Changes in Ambient Conditions	24
3.4.5	Choice of the suitable MPPT Algorithm	24
3.5	Simulation Models for PV Cells	25
3.5.1	Purpose of Simulating Photovoltaics	25
3.5.2	Different Types of Simulation Models	25
3.5.3	PV Simulation Model: Ideal Model	26
3.5.4	PV Simulation Model: Simplified Model	27
3.5.5	PV Simulation Model: Practical Model	27
3.5.6	PV Simulation Model: Double Exponential Model	28

4	Electric Range Extender (ERE)	29
4.1	Purpose of the Electric Range Extender	29
4.2	Integration of Photovoltaics in Automobiles	29
4.3	Space for Photovoltaics on Top of Vehicles	32
4.4	Power of Photovoltaics on Top of Vehicles	33
4.5	Shape of the Roof of Today's Automobiles	36
4.5.1	Roof of the Toyota Prius	36
4.5.2	Roof of the Toyota Auris	37
4.5.3	Roof of the Nissan Leaf	38
4.5.4	Roof of the Citroën C-Zero	39
4.5.5	Comparison of the Amount of Space and Power	40
4.6	The Effective Area of Photovoltaics	41
4.6.1	Orientation of Photovoltaics towards the Sun	41
4.6.2	Calculation of the Effective Area of Photovoltaics	42
4.6.3	Statistical Evaluation of the Calculated Effective Area of Photovoltaics	44
4.6.4	Normalisation of the Effective Area of Photovoltaics	48
4.6.5	Measurement of the Theoretical Output Power of Photovoltaics	50
4.7	System Structures of Photovoltaics	53
4.7.1	Parallel Connections of Photovoltaics	53
4.7.2	Series Connections of Photovoltaics	54
4.7.3	Amount of PV Cells in PV Modules	55
4.7.4	Interconnection of Photovoltaics on the Experimental Vehicle	58
4.8	Static and Dynamic Environmental Conditions	60
4.8.1	Test Profiles for MPPT Algorithms	60
4.8.2	Static Environmental Conditions	62
4.8.3	Optical Sensor Unit	63
4.8.4	Dynamic Environmental Conditions	64
4.8.5	Comparison between Static and Dynamic Environmental Conditions	71
4.9	Monitoring System for Photovoltaics	72
4.9.1	Purpose and Development of the Monitoring System	72
4.9.2	First Generation of the Monitoring System	73
4.9.3	Second Generation of the Monitoring System	76
5	Discussion	80
5.1	Summary of the Results and Contribution of the Doctoral Thesis	80
5.2	Example Calculation	82
5.2.1	Background for the Calculation	82
5.2.2	PV Simulation Model of the Photovoltaics in this Research Work	83
5.2.3	Estimation of the Output Power of the PV Installation	85
5.2.4	Impact of Different Ways of Aligning PV Modules	91
5.2.5	Impacts on the Estimation of the Output Power	94
5.2.6	Use of the Solar Energy in HEVs and BEVs	96
6	Conclusion	97

List of Figures

1	Illustration of a parking slot	1
2	Illustration of pollution due to individual traffic in urban areas	2
3	System topologies of HEVs	7
4	Planetary gear set	8
5	System topology of BEVs	11
6	Principle of regenerative braking	11
7	OSI layer model for automotives	14
8	Concept of a load balancer with ECUs along automotives	17
9	Example for a data dependency graph	18
10	Characteristic behaviour of the output power of a PV cell (I-V curve)	19
11	I-V curve under different ambient conditions	20
12	Basic structure of a photovoltaic energy harvesting system	21
13	Working principle of the P&O algorithm	22
14	Working principle of VMPPT and CMPPT	23
15	Problem of the P&O algorithm with fast changing ambient conditions	24
16	PV simulation model: Ideal model	26
17	PV simulation model: Simplified model	27
18	PV simulation model: Practical model	27
19	PV simulation model: Double exponential model	28
20	Connection of range extender and ultracapacitor, structure 1	30
21	Connection of range extender and ultracapacitor, structure 2	30
22	PV cell within experiments	32
23	Shape of the roof of the Toyota Prius	33
24	Possible amount of PV cells on the roof of a Toyota Prius	34
25	Angles of PV cells on the roof of the Toyota Prius	36
26	Shape of the roof of the Toyota Auris	37
27	Shape of the roof of the Nissan Leaf	38
28	Shape of the roof of the Citroën C-Zero	39
29	Illustration of the optimal orientation of one PV cell towards the sun	41
30	Effective PV cell areas on top of a Toyota Prius	44
31	Effective area of PV cells on top of a Toyota Auris	45
32	Effective area of PV cells on top of a Nissan Leaf	46
33	Effective area of PV cells on top of a Citroën C-Zero	47
34	Experimental vehicle	50
35	Illustration of the measurement setup	51
36	Illustration of parallel connections of photovoltaics	53
37	Illustration of series connections of photovoltaics	54
38	Schematic of the evaluation platform for different types of interconnections	55
39	Alignment of PV modules on the roof of the experimental vehicle	58
40	MPPT test profile 1, sequence with n repetitions	61
41	MPPT test profile 2, static and dynamic sections	61
42	Static environmental conditions, full day example	62
43	Static environmental conditions, part of a day example	62
44	Block diagram of the optical sensor unit	63
45	Spectrums of light sources and spectral sensitivity of photovoltaics	63
46	Block diagram of the environmental monitoring unit	65
47	Typical shading in a street in urban and residential areas	66
48	Dynamical environmental conditions, measurement 1	67
49	Dynamical environmental conditions, measurement 2	68
50	Typical shading under a highway bridge	69

51	Dynamical environmental conditions, measurement 3	70
52	Components of the monitoring system, first generation	73
53	Experimental system structure of six PV cells	73
54	Complete structure of the monitoring system, first generation	75
55	Complete structure of the monitoring system, second generation	76
56	System structure 9 x 1 (in $n_{cells,l} \times n_{cells,w}$)	76
57	System structure 3 x 3 (in $n_{cells,l} \times n_{cells,w}$)	77
58	System structure 9 x 1 (in $n_{cells,l} \times n_{cells,w}$), improved version	77
59	System structure 3 x 3 (in $n_{cells,l} \times n_{cells,w}$), improved version	78
60	Principle of obtaining variations in the monitoring system	78
61	I-V curves from the data sheet of the PV manufacturer	83
62	Difference between simulated and obtained I-V curves	83
63	Input parameter 1: Solar radiation level (λ)	84
64	Input parameter 2: PV cell temperature (T_c)	84
65	Output power of one PV cell (P_{mpp}), whole day	85
66	Sun elevation angle (α), whole day	85
67	New calculated effective area ($A_{eff,new}$) with $\psi = 180^\circ$, whole day	86
68	New calculated effective area ($A_{eff,new}$) with $\psi = 0^\circ$, whole day	86
69	New calculated effective area ($A_{eff,new}$) with $\psi = 90^\circ$, whole day	87
70	New calculated effective area ($A_{eff,new}$) with $\psi = 270^\circ$, whole day	87
71	Variations in effective areas [%], whole day	88
72	Output power of PV cells in different rows, whole day	88
73	Different alignments of PV modules, configuration (a)	91
74	Different alignments of PV modules, configuration (b)	92
75	Different alignments of PV modules, configuration (c)	93
76	P-V curve of one PV cell at different temperatures	95

List of Tables

1	Overview of hybridisation types with functions and voltage levels	9
2	Classification of HEVs based on the system topology and the system type .	10
3	Specific energy density of various energy sources for automobiles	13
4	Example for parameters of a data dependency graph	18
5	Power densities of harvesting technologies	19
6	Working principle of the P&O algorithm	23
7	Possible use of EREs in different HEVs	31
8	Parameters of one PV cell	32
9	System structures of conventional, high-cost, high-power PV modules	35
10	Longitudinal angles of PV cells on the roof of a Toyota Prius	36
11	Longitudinal angles of PV cells on the roof of a Toyota Auris	37
12	Longitudinal angles of PV cells on the roof of a Nissan Leaf	38
13	Longitudinal angles of PV cells on the roof of a Citroën C-Zero	39
14	Comparison of opportunities on different HEVs and BEVs	40
15	Calculated effective areas of PV cells on top of a Toyota Prius	42
16	Calculated effective areas of PV cells on top of a Toyota Auris	42
17	Calculated effective areas of PV cells on top of a Nissan Leaf	43
18	Calculated effective areas of PV cells on top of a Citroën C-Zero	43
19	Normalised effective areas of PV cells on top of a Toyota Prius	48
20	Normalised effective areas of PV cells on top of a Toyota Auris	48
21	Normalised effective areas of PV cells on top of a Nissan Leaf	49
22	Normalised effective areas of PV cells on top of a Citroën C-Zero	49
23	Normalised effective areas of PV cells on top of a Toyota Prius (9 rows) . .	50
24	Comparison of ΔA_{eff} with ΔP_{th}	52
25	Series interconnection of six PV cells, 4 PV modules	56
26	Series interconnection of four PV cells, 6 PV modules	56
27	Parallel interconnection of six PV cells, 4 PV modules	57
28	Parallel interconnection of four PV cells, 6 PV modules	57
29	ΔP_{th} at $\alpha = 40^\circ$ for PV cells	59
30	ΔP_{th} at $\alpha = 40^\circ$ for PV modules	59
31	Disconnection logic for the experimental system structure of six PV cells . .	74
32	Shadow in the system structure 9 x 1 (in $n_{cells,l} \times n_{cells,w}$)	79
33	Different temperatures of PV cells in different rows	94
34	Variation in output power in the MPP at different PV cell temperatures . .	94
35	Comparison of additional all-electric driving distances for HEVs and BEVs	96

1 Introduction

Ever since I remember, I have been fascinated by renewable energy resources. From 2009 on, I started to study them, in particular solar energy. In 2010, I completed my diploma thesis entitled *Improvement of the efficiency of an electric car by the use of electronics* [1]. The work was funded by austriamicrosystems AG and was accomplished within the E³-Car Project, an Europe-wide collaboration effort. My work discussed the opportunities of installing photovoltaic (PV) cells on the roof of battery-powered electric vehicles (BEVs) and hybrid electric vehicles (HEVs). This dissertation is a continuation of my diploma thesis, elaborating the opportunities of a PV installation in much more detail and proposes the use of monitoring units (MUs) together with PV modules as an electric range extender (ERE).

1.1 Motivation for the Research

Solar energy is considered as the most promising energy resource in the near future, in particular to substitute energy gained from fossil resources such as oil, gas and coal [2], [3]. BEVs are the future for individual transportation, especially in urban areas. A fast introduction to the market of this type of vehicles is delayed due to the problem how to overcome the costs of high-voltage batteries. Recently, HEVs attracted interest and could function as the transition from today's conventional vehicles with internal combustion engines (ICEs) to BEVs [4], [5]. At present, a fast introduction and widespread use of BEVs is unlikely [6].

Photovoltaics produce direct current (DC) at relatively-low voltages. Connected in series, the output voltage level is suitable to supply small appliances in cars or recharge the high-voltage battery in parked conditions. However, the area to deploy PV cells and modules on the roof of automobiles is limited [7], [8]. Hence, the focus lies on optimising the degree of efficiency of the PV installation and to maximise the benefits for the driver of the vehicle. The on-board power supply needs to be protected so that no failures of the photovoltaics can harm the performance of the car and influence the safety of the driver [8].

The roofs of vehicles represent a notable area, as illustrated in Figure 1. Beside the opportunity to install photovoltaics on houses and garages, surfaces of automobiles could be assigned for renewable energy production. Therefore, no new areas would need to be dedicated for the collection of solar energy [3]. If photovoltaics are integrated, for example into HEVs, the energy can be used efficiently within the energy management system (EMS) and supply basic loads within the vehicle [5], [8].



Figure 1: Illustration of a parking slot

In conventional vehicles, all required electricity is produced with fuel by alternators. Commonly, the degree of efficiency of alternators is about 70 % which decreases to about 40 % at higher speeds [9], [10]. BEVs and HEVs make use of regenerative braking to extend the electrical driving distance. In these vehicles, solar energy can be used to enhance driving distances and lower requirements for battery capacities [5]. The two different batteries in BEVs, the auxiliary battery and the high-voltage battery, offer several opportunities either to introduce photovoltaics in a smaller or larger scale [5], [6].

Traffic is one of the major problems in urban areas which affects the wellbeing of humans. Individual transportation is considered to be a locally generated problem and so, a local solution needs to be found [11]. Pure-electric driving and start-stop operation of ICEs are the key to reduce car emissions and air pollution within cities [11], [12], as illustrated in Figure 2. It is well known that climate and weather conditions are influenced by the city. In US cities, ambient temperature is about 0.7 °C higher than the annual mean value in the surrounding country-side. Furthermore, the solar radiation (λ [W/m²]) is up to 20 % lower in urban than in rural areas [11], [13]. These environmental circumstances have to be taken into account for the estimation of solar energy production within cities.



Figure 2: Illustration of pollution due to individual traffic in urban areas

Widespread car usage is considered to increase the rate of asthma. In particular, children are harmed by emissions of conventional vehicles with ICEs. Similarly, if pregnant women are exposed to high levels of traffic emissions, they are more likely to give birth to infants with heart defects. For example, European scientists have associated 36,000 to 129,000 adult deaths per year to traffic pollution [14]. Furthermore, noise from traffic causes health problems for humans. It is estimated the cost to the gross domestic product (GDP) is in the range of 0.2–2 % in the European Union (EU). Solutions to lower noise levels are expensive or for example, protect only humans indoors (insulated windows in houses) and not pedestrians [11].

The overall target of this research is to reduce pollution and fuel consumption, and improve the electrical driving range of vehicles. The motivation of this work is to lower emissions locally, which means at car level by integrating photovoltaics into the roof of automobiles. In here, electric and hybrid electric vehicles are of interest due to the amount of opportunities to use gained solar energy. It is worth noting that automobiles represent a new, dynamic working environment for photovoltaics. Therefore, the goal of this research is to study the circumstances of BEVs and HEVs to optimise output power levels of photovoltaics.

1.2 Research Scope and Methodology

The scope of the research work presented in this thesis is on integrated photovoltaics on the roof of electric and hybrid electric vehicles. Compared to work in the diploma thesis [1], this dissertation proposes using PV cells with monitoring units [5], presents considerations on the type of interconnections of PV cells to PV modules [15], and takes into account the non-linear, curved shape nature of vehicles roofs for PV installations [8].

PV cells are connected in series to small PV modules to increase the open-circuit voltage (V_{oc} [V]). In here, the performance of a system structure of six PV cells [5] is compared with the output power behaviour of a system structure with nine PV cells [8]. Similarly, this work evaluates the usage of MUs placed in each corner of the roof of vehicles [5] with the utilisation of MUs next to PV cells [8].

The whole system, PV modules and monitoring units, is referred as an intelligent electric range extender (ERE), the main contribution of this thesis. ERE provides status information of the photovoltaics to the EMS. Specifically, the ERE takes into account different solar radiation levels due to shadows, which can occur in driving and parking conditions. As a result, PV cells are disconnected from the interconnection if the illumination of single PV cells is much lower than from other ones. This method improves the degree of efficiency and is essential, since the area for solar energy production in automobiles is limited.

The methodology used in this work is an empirical design and engineering approach for developing, testing and evaluating the proposed ERE. This work discusses the following research questions: which type of photovoltaics are suitable for use in automobiles; which type of interconnections are the most beneficial for all circumstances that occur in cars; which opportunities to use the gained solar energy can be offered to electric and hybrid electric vehicles; what impact has the non-linear, curved shape nature of the roof of BEVs and HEVs has on the output performance of photovoltaics; which alternatives are available to reduce the energy consumption of electronics; what are the advantages and disadvantages of using a monitoring unit as a trigger for the control algorithm?

1.3 Thesis Outline

1.3.1 Chapter 2 - Electrification of Automobiles

In this chapter, an investigation on the installed amount of ECUs in today's automobiles is presented. In future, the tendency is towards a higher level of required electricity in passenger vehicles. This chapter elaborates the different system architectures of HEVs and different degrees of hybridisation. Furthermore, BEVs and their system architecture are discussed. Additionally, a detailed overview about different energy storage elements is presented. The focus lies on the auxiliary battery for the 14 V on-board power supply and the high-voltage battery which is required for electric propulsion of the vehicle. At the end of the chapter, a summary of different bus communication standards is given.

1.3.2 Chapter 3 - Principles of Photovoltaics

This chapter provides a background to use photovoltaics in automobiles efficiently. In terms of energy harvesting, the different power densities of energy sources are discussed. Afterwards, the behaviour of the output power of PV cells is elaborated. In here, the focus lies on the I-V (Current-Voltage) curve which illustrates the non-linear characteristics of photovoltaics. The relevant parameters are given, which are a useful evaluation on the quality of different PV technologies. Moreover, management strategies are presented, which allow the maximum amount of power to be obtained. Finally, various PV simulation models are shown, which allow the modelling of PV cells as a power source for different types of applications.

1.3.3 Chapter 4 - Electric Range Extender (ERE)

This is the main chapter of the thesis, in which the electric range extender is presented. At first, calculations are discussed that allow the evaluation of the effective area of photovoltaics on top of vehicles due to the different orientation of individual PV cells towards the sun. It is demonstrated that the calculated effective area corresponds to the amount of output power which can be obtained from photovoltaics in practise. Here, the variations in output performances are discussed which occur under different solar altitude angles. Furthermore, an investigation is presented which focuses on the different opportunities to establish interconnections of PV cells. At the end of this chapter, the difference between static environmental conditions, if the vehicle is parked, and dynamic environmental conditions, in case the vehicle is driving in urban and residential areas, are elaborated.

1.3.4 Chapter 5 and Chapter 6 - Discussion and Conclusion

The last section of this thesis presents a brief summary of the major findings and contributions of this research work. The focus of this summary lies in Chapter 4 in which the electric range extender is presented. At the moment, the roof of vehicles is not ideal for PV installations and if photovoltaics are deployed on top of today's vehicles, variations in output performances can be expected. These influences can be addressed with the suggestions of this work to improve and optimise the output power from the PV installation on the roof of BEVs and HEVs. A complete calculation is presented to provide an estimate on the amount of solar energy during a partly cloudy, partly sunny day. Finally, an outlook on future work is provided.

2 Electrification of Automobiles

2.1 Amount of Electronics in Automobiles

Electronic control units (ECUs) are the key elements of automobiles. Over the last few decades the amount of ECUs has increased significantly and is as many as 75 – 80 in today’s vehicles [16–19]. In upper class cars the amount is even higher than that. This progressivity has resulted in an increased electricity consumption of automobiles [16], [17]. In future, attention needs to be paid so that these components reduce rather than increase the energy consumption of vehicles, as is the situation today [8].

In 1970, the use of ECUs began by separating automotive electronics into their own units. Around 1980, a network was established to link ECUs with each other and the amount of wiring increased. In 1994, an upper class vehicle had between 20 and 30 ECUs. Back then, ECUs contained CPUs similar to a 8 bit Intel 8051 [20]. Today, automobiles have much faster CPUs with much more memory available [21]. In future, multicore ECUs are considered to encounter the rising demands of automobiles [18], [19]. Requirements for fast computation speeds are given by the EMS of powertrains from BEVs and HEVs, driver assistance systems and real-time image processing [22–25]. The overall target is to reduce the amount of ECUs by higher levels of parallelism, allowing one ECU to fulfil several functions at the same time [18].

The necessity for electronics in automobiles is given, for example in the powertrain, security solutions and comfort systems [17], [22–28]. The challenge lies in the complexity of automobiles and the opportunities they offer to their users [27]. Increased functionalities on the one hand and less amount of energy seem to be controversial, but not impossible to combine. A reduction of the amount of energy is an important matter due to the predicted increase of electronics in the near future [16], [17]. For example, HEVs contain much more electronics than conventional vehicles with ICEs [4], [6], [17], [28], [29].

Estimations for an average vehicle predicts that for an extra 50 kg weight of wiring or an extra demand on power of 100 watts, fuel consumption will increase by 0.2 litres per 100km travelled [16]. Generating electric power is considered as a strong part of fuel consumption. An output of 1 kW from the alternator requires between 1–1.4 litres of gasoline per 100 km [6]. Solutions to lower power consumption require a combination of different technical disciplines and compromises on costs and time-to-market [27].

In automobiles, knowledge from electrical, software, communication and mechanical engineering is combined. Here, more than 80 % of innovations are a result of software engineering [27]. In future, it is essential that automobiles meet lower emission rates to reduce negative health impacts for humans [11], [13], [14]. Hence, the amount of ECUs needs to be chosen in such a way that efficiency of automobiles is optimised rather than reduced, even though ECUs offer several benefits. The focus lies on HEVs for a reduction in CO₂-emissions in the near future [28], [30].

2.2 Development of Automotive Electronics

In 2003, the automotive open system architecture (AUTOSAR) was founded by various automotive manufacturers and suppliers. The target of the initiative was to establish an open system architecture for the development of future applications for automobiles. Instead of company-specific solutions, generativity in terms of standardised interfaces and electronics design is considered to simplify the development process and lower development costs. Model-based design approaches are suitable to reduce the time-to-market and therefore, ECUs need to support the AUTOSAR software [17].

Instead of one ECU fulfilling just one function, in the future, few ECUs will be needed to carry out various functions simultaneously [17–19]. Rapid Control Prototyping (RCP) offers a fast transition from design concepts to experimental verifications. The total development environment (TDE) is based on MATLAB/Simulink[®] which is suitable to perform RCP and ensure long time stability of the development. At first, a theoretical model with linear and non-linear equations is defined. Afterwards, extensions for a real-time operation are included into the model. After the source code is generated, the code is transferred to a platform with a digital signal processor (DSP) and tested [31].

RCP is an opportunity to verify possible solutions. Thus, the focus lies on the functionality and not on hardware constraints. Moreover, the target hardware for RCP should offer a several times faster CPU and much more memory. As such, the hardware of the RCP replaces the ECU completely. The necessary reduction which is needed to adopt the development for an ECU is left for the final design phase [31]. However, in the development of hardware and software, scenarios need to be avoided in which customers become test drivers [20].

2.3 Configuration of the Powertrain of Automobiles

2.3.1 Configuration and Classification of HEVs

In today's automobiles the usage of mechanics and electronics is often combined whilst improvements require a wide understanding of the different topologies, due to the linkage between subsystems [6], [27], [28]. In the case of HEVs, a classification can be made in two ways: Once based on the system architecture or topology, and once according to the degree of hybridisation. In general, system topologies can be categorised into series, parallel, and series-parallel HEVs [1], [4], [17], [28], [30], [32], [33]. Different levels of hybridisation can be classified into micro-, mild-, medium-, and full-HEV [5], [6], [28], [30], [33].

Figure 3 illustrates the main system topologies of HEVs. P_m is the mechanical power delivered from the ICE which influences the fuel consumption of the vehicle; P_g is the electrical power provided from the electric generator; P_b is the electrical power to charge/discharge the high-voltage battery; P_e is the electrical power exchanged between the power converter and the electric motor; and P_d , $P_{d,1}$, $P_{d,2}$ are power levels to and from the drive train [1], [4], [17], [28], [30], [32], [33].

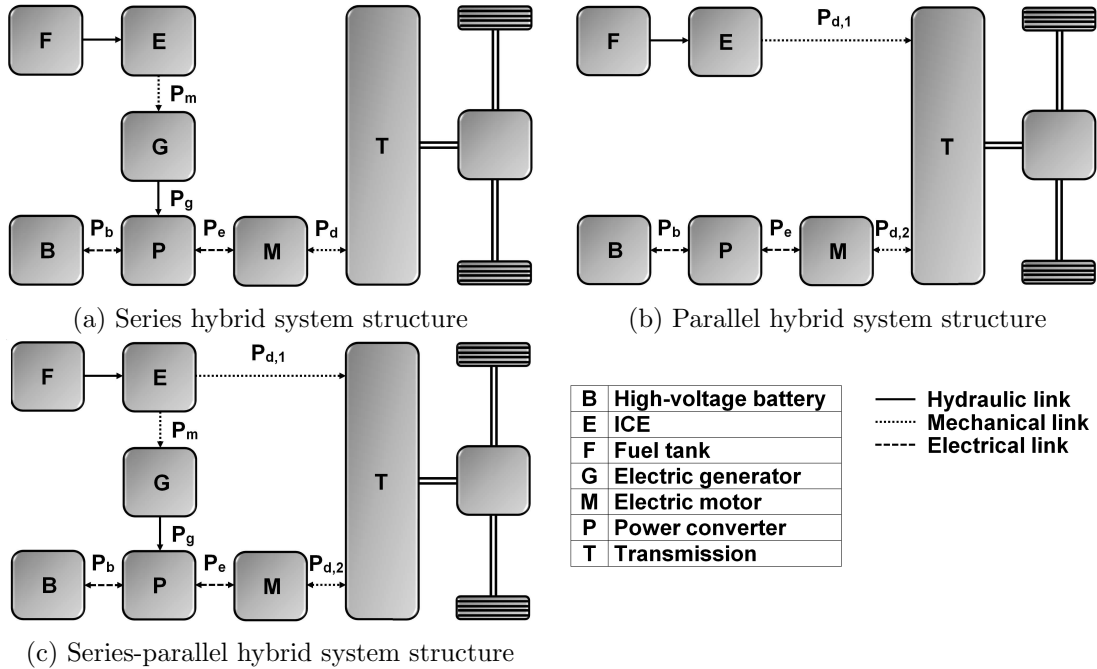


Figure 3: System topologies of HEVs

(a) Series HEV (S-HEV)

In S-HEV architectures, two electric engines are present: one which converts the mechanical output of the ICE into electricity and one which provides the propulsion of the vehicle; as illustrated in Figure 3 (a). In this system structure, the ICE is not used for propulsion directly, since there is no mechanical connection to the transmission present. This type of configuration is considered as an advantage as the powertrain is simplified. Disadvantages lie in the lower system efficiency, since the energy needs to be converted several times. Moreover, all three engines need to be sized for the maximum level of sustained power. Commonly, the S-HEV architecture is implemented in diesel locomotives and busses, but is not considered for passenger vehicles [1], [4], [17], [22], [28], [30], [32], [33].

(b) Parallel HEV (P-HEV)

In P-HEV topologies, both the ICE and electric motor are connected to the transmission and can provide power for the propulsion at the same time; as shown in Figure 3 (b). It is also possible that either the ICE or the electric motor alone supply the propulsion power. Compared to the S-HEV, only one electric engine is present, since the electric generator is removed. The electric motor can be also used as an electric generator to charge the high-voltage battery during regenerative braking or when the power provided by the ICE is greater than the power required. This systems topology achieves lower emissions and fuel consumption [1], [4], [17], [22], [28], [30], [32], [33].

(c) Series-Parallel HEV (S/P-HEV)

S/P-HEVs can be seen as a combination of S- and P-HEV. Their system structure is illustrated in Figure 3 (c). The planetary gear set, which is shown in Figure 4, provides an additional mechanical link in the vehicle. In here,

- the electric motor and transmission shaft are connected to the planetary ring gear set,
- the ICE is connected to the carrier, and
- the electric generator is connected to the sun gear.

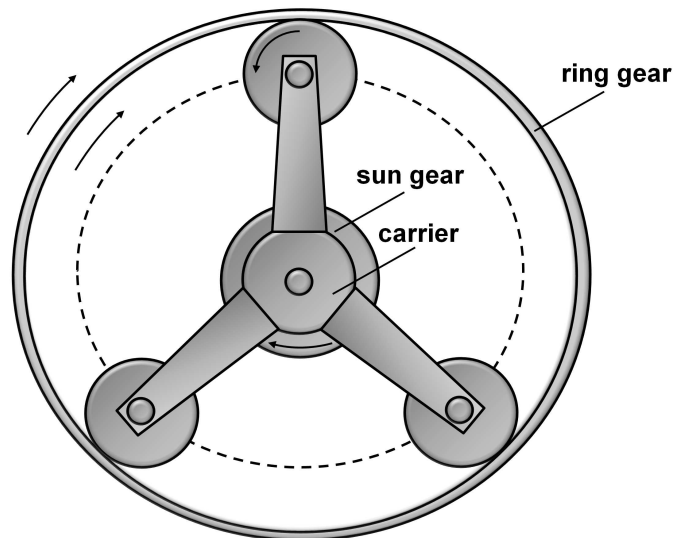


Figure 4: Planetary gear set

One share of the available power can be used for propulsion, while the other part can be applied to the generator to produce electricity. This electricity can be used to charge either the high-voltage battery or power the electric motor. Furthermore, S/P-HEVs offer other features from S-HEVs and P-HEVs however, the downside of S/P-HEVs is higher costs due to three engines and the planetary gear set. [1], [4], [17], [28], [30], [32], [33].

As mentioned above, classification of HEVs into several categories can be established based on the degree of hybridisation and installed system power, and according to the possibilities [5], [6], [22], [28], [30], [33], [34]. Table I presents an overview of different hybridisation types with functions and voltage levels [6], [34].

Table 1: Overview of hybridisation types with functions and voltage levels

hybrid system type	voltage level	main hybrid functions		
		regenerative braking	motor assist	electric drive
none (ICE)	14 V	no	no	no
micro-HEV	14–42 V	minimal	minimal	no
mild-HEV	42–120 V	moderate	moderate	no
medium-HEV	144 V	yes	yes	moderate
full-HEV	200 V	yes	yes	yes

(a) Micro-HEV

HEVs in this category are equipped with integrated starter generators (ISGs) as alternators. The amount of power from ISGs, either belt-driven (B-ISG) or crankshaft-mounted (C-ISG), is limited and is used to support the ICE during startup. Additionally, automatic start/stop operation is implemented to switch off the ICE when at a standstill. The capacity of ISGs is typically in the range of 2–4 kW and allows regenerative braking on a small scale. As a result, the fuel consumption can be reduced in the range of 2–10 % [6], [22], [28], [30], [33], [34].

(b) Mild-HEV

At lower engine speeds, the electric engine supports the ICE, for example by the help of a motor assist offering a boost function for propulsion during acceleration. Mild-HEVs have higher system voltage levels than micro-HEVs. Therefore, the electric engine recovers more energy during braking to charge the battery. This results in fuel savings in the range of 10–20 % [6], [28], [30], [33], [34].

(c) Medium-HEV

If the system voltage level is further increased, as it is the case of medium-HEV, the opportunity to charge the high-voltage battery during regenerative braking becomes optimised. The electric engine also provides propulsion at higher speeds. Fuel savings are located in the range of 20–30 % [6], [34].

(d) Full-HEV

Pure-electric propulsion requires high system voltage levels of over 200 V which becomes a reality with this type of HEV. This is in particular beneficial in urban areas. However, the primary energy resource is still the fuel tank. Commonly, the capacity of the high-voltage battery is limited and in the range of a few kWh which restricts the electric-only driving distance. Recently, plug-in full HEVs have become popular due to new high-voltage batteries with a higher capacity. In contrast to conventional full-HEV, the high-voltage battery can be charged during parking conditions with electricity. Hence, the fuel consumption of the vehicle can be further reduced. Similarly, an additional high-voltage battery can be installed and charged externally to enhance the pure-electric driving range [1]. Full-HEVs offer all features of other hybridisation types with the highest benefits to reduce fuel consumption; possible possibly in the range of of 30–50 % [6], [22], [28], [30], [33], [34].

Unfortunately, it is not possible to apply every hybrid system type to the different hybrid system architectures. Table 2 summarises which hybrid system types such as micro-, mild-, medium-, and full-HEV can be considered for use in S-, P-, and S/P-HEVs [33]. As seen from Table 2, P-HEVs offer the highest flexibility for different degrees of hybridisation.

Table 2: Classification of HEVs based on the system topology and the system type

hybrid system topology	hybrid system type			
	micro-HEV	mild-HEV	medium-HEV	full-HEV
S-HEV	no	no	yes	yes
P-HEV	yes	yes	yes	yes
S/P-HEV	no	no	yes	yes

2.3.2 Configuration of BEVs

BEVs have a simplified powertrain, since an ICE and fuel tank are not required. Additionally, only one electric engine is present which can either function as an electric motor or electric generator, as illustrated in Figure 5 [33]. The high-voltage battery is the only source of energy for propulsion which means that BEVs always offer pure-electric propulsion of about 100–200 km. The driving range depends on the capacity and on the state of charge (SOC) of the high-voltage battery [7], [28], [30]. At present, the high-voltage battery is the main cost factor which results in the high initial costs of BEVs [1], [29]. The advantages of BEVs are local zero-emission and high energy efficiency [28], [30], [33].

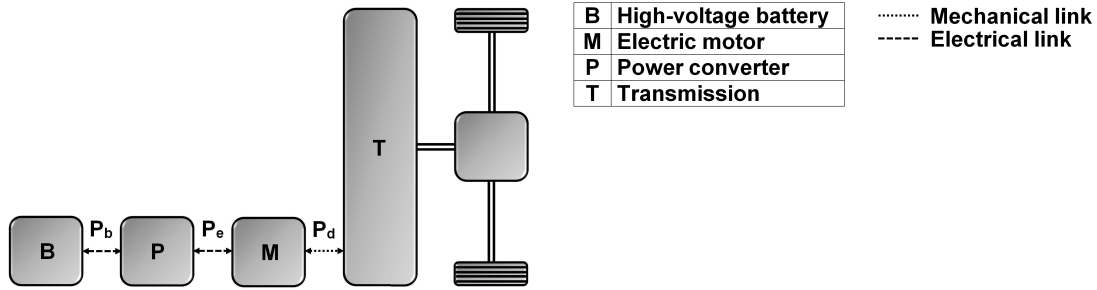


Figure 5: System topology of BEVs

2.3.3 Functionalities within the Powertrain

As mentioned above, micro-HEVs are the first degree of hybridisation of conventional vehicles with ICEs. A further classification into micro-1-HEVs and micro-2-HEVs can be established based on the capability to gain energy during regenerative braking [29]. Basically, all required electricity of vehicles is provided by the ICE; with the exception of plug-in full HEVs in which high-voltage batteries can be charged with electricity from the power grid [6], [22], [28], [30], [33], [34].

Depending on the hybrid system type, electricity can be gained during braking which is then referred as regenerative braking. Here, the possibility is given to convert part of the kinetic energy of the automobile into electrical energy and thus, the obtained electricity is used to charge the battery of the vehicle. Higher the voltage of the system battery, the more energy can be recovered, as illustrated in Figure 5 [17].

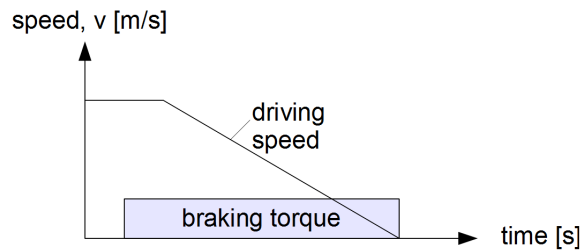


Figure 6: Principle of regenerative braking

ECUs play a key role in determining how much the fuel consumption can be reduced in HEVs. In the powertrain, the EMS decides whether the produced electricity is used to charge the battery or applied to the electric motor directly for propulsion of the vehicle. Several ECUs are needed to manage the entire powertrain: management of the battery, management of the combustion and electrical engine(s), management of the transmission and braking [17], [26]. As a result, ECUs have an impact on the performance and functionality of the entire car [17].

2.4 Energy Storage Devices in Electric and Hybrid Electric Vehicles

2.4.1 Storage Elements in BEVs and HEVs

In the previous section, different hybrid systems are discussed and due to these different implementations, the capacity of the batteries varies. Furthermore, the amount of batteries varies as well as the voltage level of the on-board power supply. In general, there are two batteries in HEVs, the auxiliary battery with an operating voltage of 14V and the high-voltage battery with an operating voltage up to 200 V [6], [29], [34], [35].

Commonly, hybrid system topologies include one or two electrical engines, an ICE, an auxiliary battery and a high-voltage battery. During phases of regenerative braking, the high-voltage battery is charged, since the dynamic charge acceptance (DCA) of the auxiliary battery is limited which means that the auxiliary battery cannot be charged quickly. This limitation of DCA of auxiliary batteries is also present, even though the battery is not completely charged [6], [29]. The DCA depends on the SOC of the battery. In particular a few minutes after a discharge pulse has occurred, the DCA is limited [36].

Lead/acid batteries, with liquid or absorptive glass-fibre mat electrolyte, are considered for the use of auxiliary batteries in micro-HEVs. Advanced absorbent glass mat (AGM) batteries have a better DCA, thus, their usage includes mild-HEVs as well as medium-HEV. In comparison to lead/acid batteries, advanced AGM batteries show a three-fold longer shallow-cycle life. However, the battery has to withstand temperatures of around 70 °C, which is a drawback of AGM batteries. Furthermore, moving batteries to different locations with lower environment temperatures results in higher costs for the manufacturing of vehicles [6].

Cyclic wear is associated as the major cause of failure for auxiliary batteries which also tends to be a particular problem for batteries in HEVs, especially for micro-HEVs. During key-off, small currents slowly lower the SOC of the battery however, these currents can be higher due to failures or defects in ECUs. The amount of ECUs can also have an impact on the discharge during standing times as well. ECUs for comfort systems consume energy at irregular times and thus, the battery is used as a buffer when more energy is required. Charges and discharges of the battery are typically very shallow but can become significant over the years [37–39]. The main factors which determine the cycle life of batteries can be summarised as follows:

- the depth of discharge
- the charge rate
- the operating temperature
- the average SOC

Electrolytic double-layer capacitors, commonly referred as supercapacitors or ultracapacitors, are considered as a solution to satisfy the short term energy demands of automobiles. Supercapacitors have a long shallow-cycle life, since no electrochemical reactions takes place during charging and discharging cycles. However, the energy density of these types of capacitors is weak and is thus considered as one of the disadvantages of these devices. Additionally, the voltage of ultracapacitors sags proportional to the SOC [35], [37].

Currently, research is conducted for potential applications of supercapacitors within automobiles. In upper class vehicles, a single lead/acid battery does not meet the energy requirements. Thus, two batteries are installed: one for cranking the engine and one for cycling loads. Furthermore, the energy management system needs to consider the opportunity of distributed energy storages if fuel cells, batteries and supercapacitors are used simultaneously as a power source [40].

In BEVs and HEVs, high-voltage batteries need to provide a high specific power and energy, a high DCA and a long operating life at a suitable cost level. Here, the operating life indicates the possible amount of deep discharge cycles or how long batteries stay in service before replacement is required [41]. The following list presents battery materials which are of interest for BEVs and HEVs [41], [42]. Table 3 presents the specific energy density of energy sources [Wh/kg] which are relevant for automobiles. It can be seen that the energy per unit mass of gasoline is much higher than from different battery types. In general, specific energy density values range from 45 to 300 Wh/kg for primary batteries and from 30 to 240 Wh/kg for secondary or rechargeable batteries [42].

- Lead-acid (Pb-acid)
- Nickel-cadmium (NiCd)
- Nickel-metal-hydride (NiMH)
- Lithium-ion (Li-ion)
- Lithium-polymer (Li-poly)

Table 3: Specific energy density of various energy sources for automobiles

Energy source	Specific energy [Wh/kg]
Gasoline	12,500
Pb-acid	30–50
NiCd	45–80
NiMh	60–120
Li-ion	110–180
Li-poly	110–180

2.4.2 Energy Management Systems of Automotive Batteries

Energy management can be divided into different categories. The simplest implementation measures the SOC of batteries and presents measurement results to the driver. For a real energy management of the battery, an intervention in the control circuit is required. Here, the engine is set to a minimum rotation speed to establish a suitable charge current for the battery. In addition, loads are switched off according to the properties of the on-board power supply. HEVs demand the highest implementation level of an energy management system [17], [39].

Based on the main objective, the monitoring of the battery can also be divided into categories. The target can be to obtain the SOC, the state of health (SOH) which is the information of the remaining life time of the battery, or the state of function (SOF) which is an important piece of information, for example, for starting the engine. Furthermore, with the aid of an ECU, temperature, voltage and battery current can be measured. By the help of these input parameters and simulation models, the ECU can compute the required output variables for the set point of the control circuit to suitably charge and discharge the battery [17], [39].

The efficiency of the energy management depends on the accuracy of simulation models. Uncertainties occur due to different battery types which are used in automobiles. An extreme solution could be to use only one type of battery and this battery is installed in all vehicles. However, a better solution is a communication interface which provide information about the battery type to other ECUs. In this case, car workshops are needed for battery replacements [17], [39].

A power supply management (PSM) unit is used to control the on-board power generation with the target to optimise the amount of available electricity, to extend the operating life of the battery, to improve the performance of the vehicle and to reduce fuel consumption. In particular for HEVs, advanced strategies are needed to carry out PSM in a successful way. Power demand management (PDM) allocates a certain amount of energy based on priorities and requirements. Therefore, the setup and order of priorities needs careful consideration. Advanced PDM algorithms carry out scheduling dynamically rather than statically [6].

2.5 Communication and Data Exchange in Automobiles

2.5.1 Bus Communication Systems

The open system interconnection (OSI) model is suitable to describe the network architecture, which is present in automobiles. Commonly, network protocols are classified into different layers, which provide several features to carry out different tasks. Each layer is supposed to handle a well-defined function. The OSI model can be applied for ECUs which are open for communication with other ECUs. Figure 7 illustrates the seven different layers of the OSI model and the groups of these layers in the automotive industry [17], [39], [43].

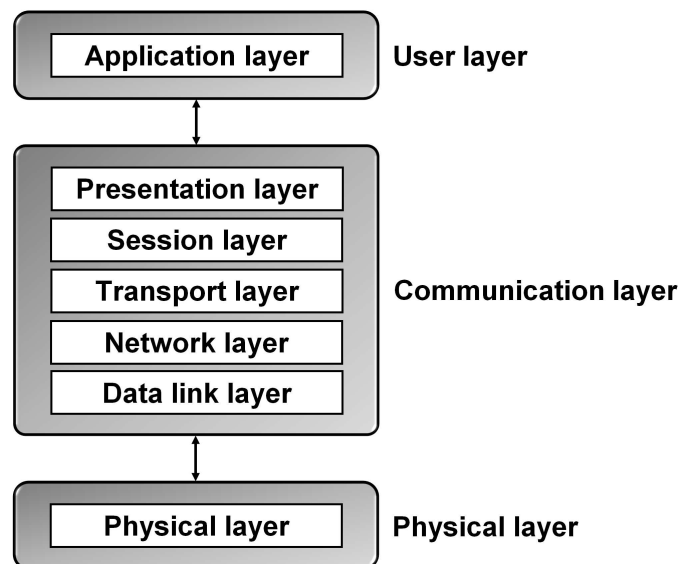


Figure 7: OSI layer model for automobiles

2.5.2 Controller Area Network (CAN)

At present, the most widespread bus communication system in everyday use is the CAN-Bus. In 1991, CAN-Bus was the first bus communication system implemented in series. In the powertrain, information needs to be exchanged over fast data rates, faster than in the comfort area. Thus, two system were introduced which operate at different rates, the highspeed-CAN (CAN-C) and the lowspeed-CAN (CAN-B), respectively [17], [39], [44].

CAN-C is designed for real-time operation and provides data rates up to 1 MBit/s. The focus of CAN-C lies in engine control and driving stability systems such as electronic stability control (ESC). CAN-B operates at data rates between 5 kBit/s and 125 kBit/s. This is a suitable data rate for many comfort systems such as air conditioning, window openers, navigation system, and mirror positioning, as the data rate is high enough [17], [39], [44].

In the CAN-Bus topology, there is no central ECU which is required to establish the bus communication system. Thus, new ECUs can be attached to the bus in an easy way and each ECU which is connected to the bus architecture can transmit and receive data. It is worth noting that a faulty ECU does not affect the linear structure. At the physical layer, data is transmitted in the form of two logical states whilst non-return to zero (NRZ) is used for coding. CAN-C and CAN-B can be installed in automobiles with a two-wire line, namely CAN_H and CAN_L. For cost reductions, CAN-B also works with a one-wire line [17], [39], [44]. Data communication via the CAN-Bus can be simulated to analyse the load of the bus [45].

2.5.3 Local Interconnect Network (LIN)

A low-cost variant of the CAN-Bus was introduced due to the increased usage of mechatronic systems in automobiles. In 1998, the specification of the LIN-Bus was established while in 2001, it was used for the first time in series. The focus of this bus communication system is the interconnection of sensors and actuators. The LIN-Bus topology is usually a line structure and provides data rates up to 20 kbit/s with a possible amount of 16 devices on the bus [17], [39], [44].

The electrical interface is simple and inexpensive. With lower requirements, less advanced microcontrollers units (MCUs) are suitable for implementation of the LIN-Bus. In general, a differentiation is made to the master, which is the gateway to the CAN-Bus, and slaves. The communication is synchronised while the clock is given by the master unit. On the physical layer, the voltages on the LIN-Bus range between 0 and the voltage of the auxiliary battery [17], [39], [44].

2.5.4 FlexRay-Bus

The FlexRay-Bus was developed especially for critical control operations within automobiles. The focus of this bus communication type lies on the security of the data transmission. Thus, FlexRay allows real-time operation and meeting time deadlines. FlexRay-Bus offers high data rates, is fault tolerant, and flexible related to applications and possible extensions. Main application areas include the powertrain and automotive systems, which require a high rate of security. Therefore, a second pair of wires can be used as a redundant communication path [17], [39].

The data communication protocol is divided into two slots, a static and a dynamic slot. In general, data rates up to 10 MBit/s are supported. If both channels are combined for transmission, under ideal conditions data rates up to 20 MBit/s can be achieved. The system topology of the FlexRay-Bus can be established in different ways. The amount of ECUs which can be interconnected varies and depends on the choice of the systems architecture. Commonly, up to 24 ECUs can be connected with each other. It is worth noting that additional hardware is required in the form of a host processor, a communication controller, a bus driver and an optional bus guardian to support a communication over the FlexRay-Bus [17], [39].

2.5.5 Media Oriented Systems Transport (MOST) Bus

The MOST-Bus was developed in particular for infotainment systems in automobiles and was introduced in 1998. This bus communication type is primarily installed in upper class vehicles. Electromagnetic interference (EMI) needs to be taken into account due to the high data rates of the MOST-Bus. These data rates are needed for the transmission of large amounts of data such as audio and video files. The data rate of this bus communication system varies from 24.8 MBit/s (MOST25), 50 MBit/s (MOST50), up to 150 MBit/s (MOST150) [17], [39].

An interconnection of up to 64 devices is possible. The layer model of the MOST-Bus includes a physical layer which can be an optical or electrical connection depending on the required data rate. The upper layers are a MOST network interface controller (NIC) which controls the physical layer, whilst the MOST network service manages the access to the MOST NIC. On top of the MOST network service are the applications of the MOST device [17], [39].

2.5.6 Bluetooth

Bluetooth substitutes infrared communication as wireless communication. The development started in 1994, and the first version was introduced in 1998. The primary focus of Bluetooth in automobiles lies on the interconnection of mobile entertainment devices such as car radios, mobile phones, headsets or computers. Bluetooth is also capable for maintaining applications which need to be carried out at car repair stations [17], [39].

The feature named as enhanced data rate (EDR) offers data rates up to 3 MBit/s instead of 1 MBit/s with reduced power consumption. Bluetooth operates on the industrial, scientific, and medical (ISM) radio band at 2.4 GHz. Thus, disturbances need to be taken into account from garage door openers and other devices, which are operating within this frequency band. Disturbances are avoided by dividing the band into 79 channels with a frequency distance of 1 MHz and frequency hopping [16], [17], [39].

2.5.7 Load balancing within ECUs

The five main bus communication systems found in automobiles offer different data rates and are used separately or combined over gateways in vehicles [17], [46]. However, undersizing or oversizing of ECUs can result in a negative effect. If ECUs are oversized for their purpose and requirements, their costs and power consumption can be too high compared to the objectives they need to fulfil. Load balancing can therefore be used to divide the workload efficiently. As a result, more work can be processed and operations are faster [46].

Load balancing of static and dynamic workloads is complicated in large distributed systems such as automobiles. Optimisation algorithms are needed which minimise the load imbalance on the one hand and communication overhead on the other. In static cases, the workload is known in advance and can be distributed among ECUs connected to the bus communication system. In dynamic cases, parallel computation is used with ECUs in the nearest neighbourhood [46].

The advantages of load balancing consist in the reduction of the response time and the establishment of redundancy. If the workload is divided between ECUs, the response time of one of these ECUs is reduced due to the lower load factor. Moreover, if one ECU fails, the remaining ECUs can compute the operation to its end without a notable downtime. As long one ECU is faulty, data transmission is stopped to this particular ECU [46].

Load balancing requires knowledge on the workload of the CPUs of ECUs in advance [46]. Therefore, a load balancer can be integrated into a star network, as shown in Figure 8 [43]. The components of a load balancer are a load detector, which acts like a trigger if a load imbalance is detected; a load estimator, which predicts the workload of ECUs; and a mediator, which collects information about the loads imbalance on the monitored network. Load distribution algorithms are applied to set the acceptance rate of new data for an ECU [46].

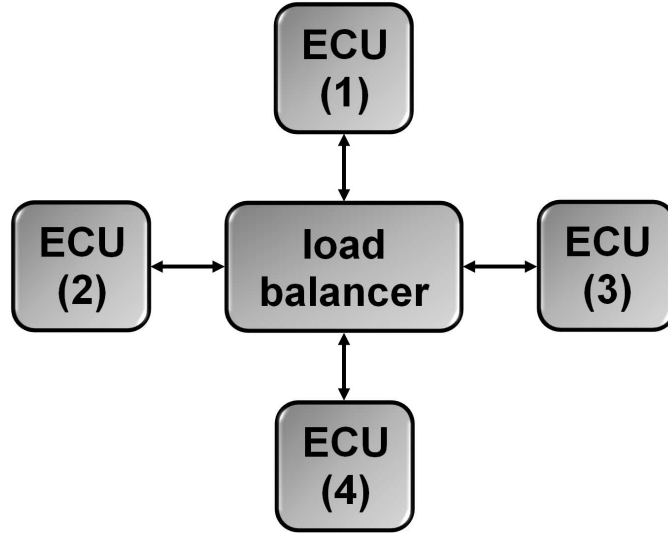


Figure 8: Concept of a load balancer with ECUs along automobiles

An overloaded ECU can have a significant impact on the performance of the entire network. CPUs of ECUs can be downsized if the workload is equally distributed along the network. The performance of a load balancer can be improved if the length of jobs is taken into consideration and if tasks are carefully dispatched from frequently overloaded ECUs. The best operation mode is achieved when all ECUs within the interconnection are fully utilised without any ECU in saturation [46]. Furthermore, load balancing can be helpful to lower the power consumption of CPUs [47].

2.5.8 Data Management in Real-Time Systems

As mentioned above, the amount of ECUs has increased and so has the computation power of their CPUs along with the amount of installed memory. As a result, the complexity of the software, which runs on ECUs, has raised. Furthermore, strict law regulations need to be fulfilled in the automotive industry. Restrictions on emission levels require the powertrain to be observed and controlled at all time. Emissions under different driving conditions are analysed and parameters are adjusted to meet these limit values. For a successful control of the powertrain, data is required and different ECUs along the powertrain and other vehicle systems need to communicate with each other [17], [39], [48].

Basically, there two constraints for real-time operation in automotive systems: time limits for the computation of data and freshness of data. Thus, the amount of needless computations should be reduced as much as possible. Therefore, on-demand updating algorithms can be applied which consider the need to update information. The problem for this type of algorithms lies in the assumption that the recalculation of parameters always produces new results. If calculations are carried out periodically, the computation effort can be unnecessary in cases where the result of the calculation is the same as in the calculation before [48].

On-demand top-bottom (ODTB) algorithms neglect unnecessary computations and enhance CPU utilisation levels. ODTB algorithms reduce the amount of recalculations down to zero once steady state is reached. Data dependency graphs visualise the connection of parameters and calculations of different ECUs with each other. Table 4 presents different parameters of an automobile whilst Figure 9 illustrates the data dependency of these parameters. Every time data is requested due to a trigger event, the timestamp of the data is checked [48]. This check decides the relevance for an update and whether recalculations and computations are need to be made or not [48], [49].

Table 4: Example for parameters of a data dependency graph

1	lambda probe status variable
2	lambda probe status for lambda ramp
3	enable lambda calculations
4	lambda factor
5	basic fuel factor
6	basic fuel and lambda factor

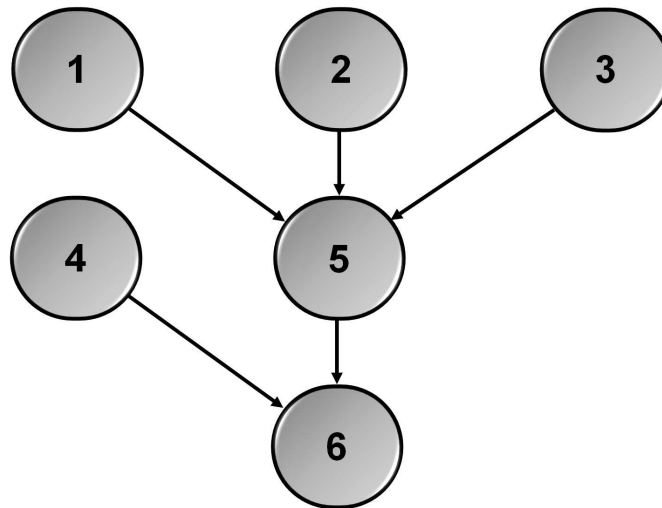


Figure 9: Example for a data dependency graph

In general, ECUs can be interconnected over many different bus communication systems and gateways. In the network, ECUs depend on the data and information from other ECUs. For example, an air conditioning system requires the position of the window opener. Hence, ECUs cannot be just left out, their presence has an impact on other ECUs which can be located in different subsystems [17], [39], [48].

3 Principles of Photovoltaics

3.1 Power Density of Energy Sources

Energy harvesting is popular for applications such as embedded systems and wireless sensor network (WSN) nodes to prolong the operating life time [50]. Table 5 presents the potential of energy harvesting sources in terms of available power density. It is worth noting that photovoltaics offer a much higher power density in comparison to other power sources [51]. This makes the use of PV cells attractive, in particular, if the area for energy production is limited and the application requires a significant amount of power.

Table 5: Power densities of harvesting technologies

Harvesting technology	Usage information	Power density
PV cells	outdoors at noon	15 mW/cm ²
Piezoelectric	inserted in shoes	330 μ W/cm ³
Thermoelectric	10 °C gradient	40 μ W/cm ³
Acoustic noise	100 dB	960 nW/cm ³

3.2 Output Behaviour of Photovoltaics

As mentioned above, photovoltaics as a power source are of interest due to their high power density [51]. One of the disadvantages of photovoltaics lies in their strong non-linear behaviour. The I-V (Current-Voltage) curve, shown in Figure 10, describes the characteristic behaviour of the output power [8], [15], [52–54]. This illustration is important, since the slope of the curve varies between different types of PV cells [15]. Only one point exists, in which the maximum amount of power can be obtained, referred as the maximum power point (MPP) [8], [15], [52–54].

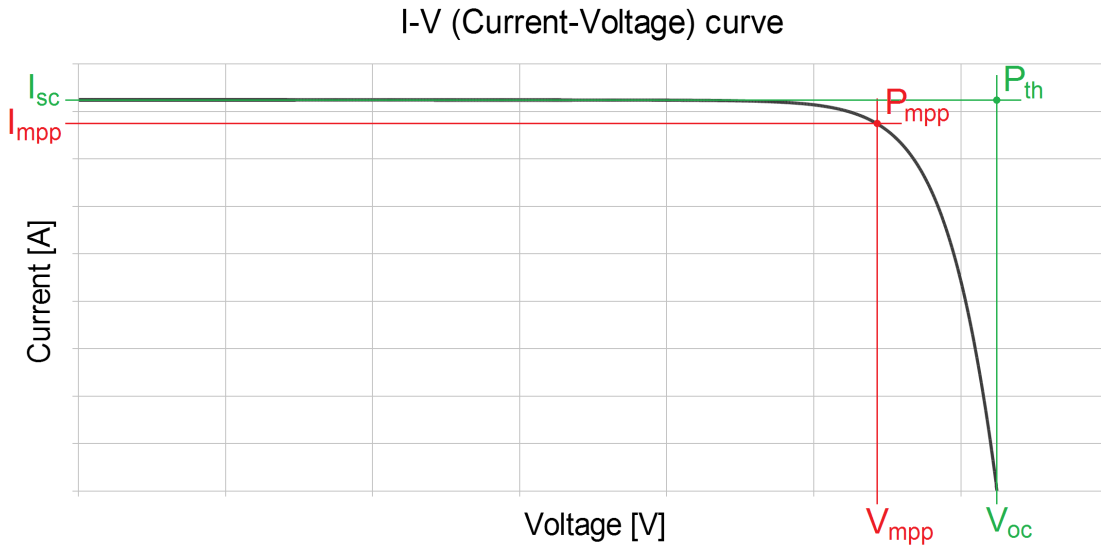


Figure 10: Characteristic behaviour of the output power of a PV cell (I-V curve)

The fill factor (FF) is suitable for evaluating the slope of PV cells and can be obtained as follows:

$$FF = \frac{V_{mpp}I_{mpp}}{V_{oc}I_{sc}} = \frac{P_{mpp}}{P_{th}} \quad (1)$$

where V_{oc} [V] is the open-circuit voltage, I_{sc} [A] is the short-circuit current, V_{mpp} [V] is the voltage in the MPP, I_{mpp} [A] is the current in the MPP, P_{th} [W] is the theoretical amount of power, and P_{mpp} [W] is the power in the MPP [8], [15], [52–54]. The goal is that the operating voltage (V_{op} [V]) equals the voltage in the MPP (V_{mpp}). For example, if the operating voltage is set to a different voltage level, an output power (P_{out} [W]) is obtained which is less than the power in the MPP (P_{mpp}); summarised as follows:

$$\begin{cases} P_{out} = P_{mpp} & \text{if } V_{op} = V_{mpp} \\ P_{out} < P_{mpp} & \text{if } V_{op} \neq V_{mpp} \end{cases}$$

The position of the MPP varies with changing ambient conditions such as the solar radiation level (λ [W/m²]) and the temperature of the PV cell (T_c [K]) [55], [56]. The I-V curve at different solar radiation levels and temperatures is shown in Figure 11. For example, if the solar radiation level is 600 W/m² and the PV cell temperature decreases by 10 K, the operating voltage (V_{op}) needs to be alternated from $V_{mpp,1}$ to $V_{mpp,2}$. Hence, V_{op} needs to be continuously varied under changing environmental conditions towards the current V_{mpp} .

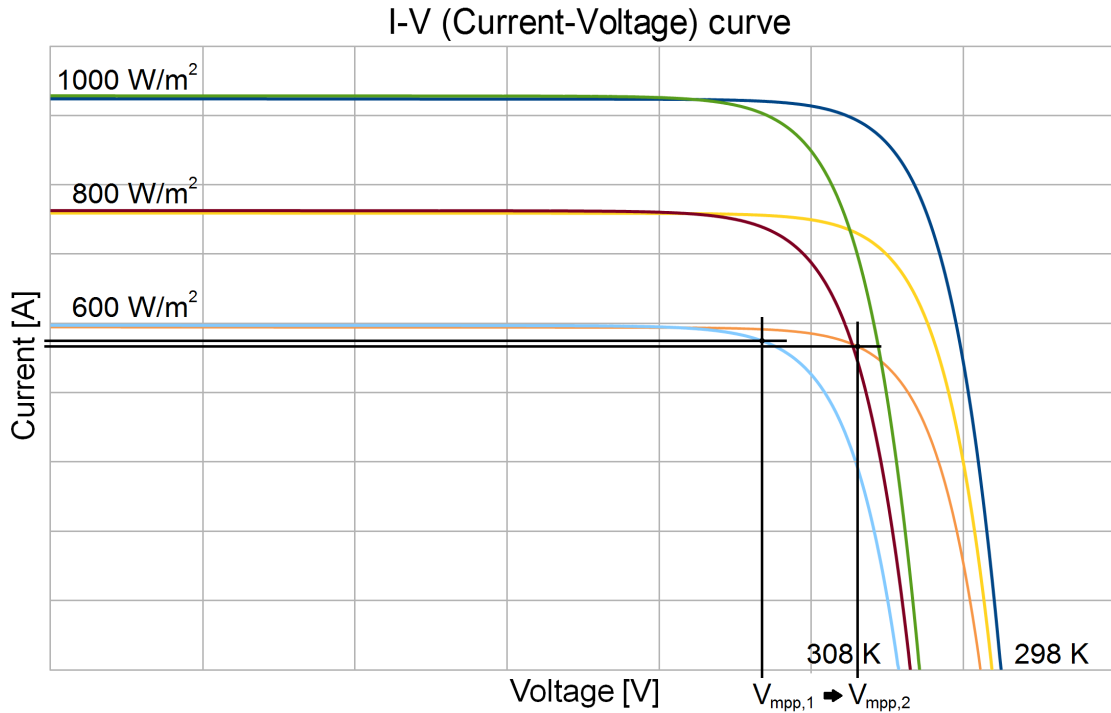


Figure 11: I-V curve under different ambient conditions

3.3 Basic Structure of the Photovoltaic Energy Harvesting System

The simplified system structure contains photovoltaics as power source on the input side, and a power sink, for example a battery, on the output side. Between these two components, a management structure is required which allows collecting the energy from photovoltaics efficiently. In this system part, a MCU is present, which performs maximum power point tracking (MPPT). MPPT ensures operating at or as close to the MPP as possible [55].

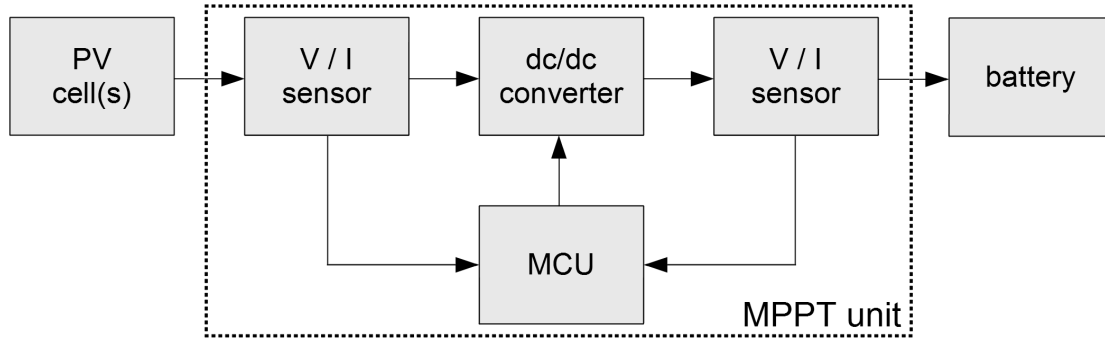


Figure 12: Basic structure of a photovoltaic energy harvesting system

The dc/dc converter is needed to match the voltage from the photovoltaics with the voltage of the battery. For example, a Li-ion battery has a voltage level of about 3.7 V, while a PV cell operates at a voltage of about 0.6 V in the MPP. Moreover, as seen in Figure 11, the open-circuit voltage (V_{oc}) varies if the cell temperature of the PV cell (T_c) changes. These circumstances influence the design requirements of power converters. If temperature variations are taken into account, the dc/dc converter topology can be simplified and the degree of efficiency can be improved. For example, instead of a buck-boost converter, only a buck converter or boost converter can be installed.

3.4 Maximum Power Point Tracking (MPPT) Algorithms

3.4.1 Examples for MPPT Techniques

At least 19 distinct MPPT algorithms have been proposed over the last decades [55]. Depending on the requirements of the application, the approaches differ from each other, for example, in the required amount and type of sensors, the efficiency, and costs of implementing the management strategy. Unfortunately, this large variety on MPPT algorithms complicates the choice of the right method for the application. Moreover, depending on the environmental conditions, some MPPT techniques provide higher efficiency levels than other ones.

3.4.2 Perturb and Observe (P&O) Algorithm

The P&O algorithm can be considered as one of the most popular MPPT algorithm. The MCU varies the duty cycle of the dc/dc converter in order to change the operating voltage and current of the photovoltaics. As a result, the present operation point (P_{out} and V_{op}) is modified with the goal to reach the MPP (P_{mpp} and V_{mpp}), as shown on the P-V (Power-Voltage) curve in Figure 13. For example, if the voltage level is increased, the output power is raised. However, if the voltage level is lowered, the output power is reduced [55].

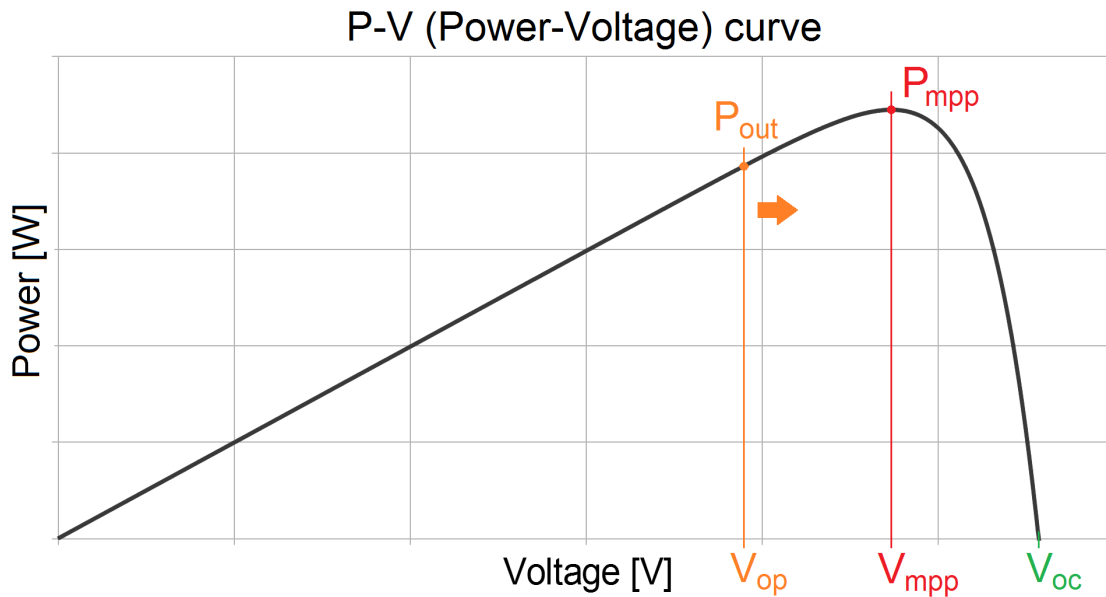


Figure 13: Working principle of the P&O algorithm

Since the exact voltage in the MPP (V_{mpp}) is unknown, it is unclear whether the current operating point is on the left- or right-hand side of the MPP. Hence, the changes from the MCU need to be observed so that positive and negative impacts on the amount of output power can be detected. This observation affects the perturbation in the next iteration. Table 6 summarises possible situations for the P&O algorithm.

Table 6: Working principle of the P&O algorithm

Perturbation	Change in power	Next perturbation
Positive	Positive	Positive
Positive	Negative	Negative
Negative	Positive	Negative
Negative	Negative	Positive

3.4.3 Voltage-based MPPT (VMPPT) and Current-based MPPT (CMPPT)

There is a strong linear correlation between the voltage in the MPP (V_{mpp}) and the open-circuit voltage (V_{oc}), even though changes in solar radiation and temperature level occur. We can make use of this linear relationship and assume the operating voltage (V_{op}) as a fraction of V_{oc} . In the case of voltage-based maximum power point tracking (VMPPT), this fraction can be considered by using the factor M_V , as explained by Equation (2) and as shown in Figure 14. Similarly, we can use a fraction of the short-circuit current (I_{sc}) and a factor M_I to establish current-based maximum power point tracking (CMPPT), as explained by Equation (3) and as illustrated in Figure 14 [55], [57].

$$V_{MPP} \approx M_V V_{oc} \quad (2)$$

$$I_{MPP} \approx M_I I_{sc} \quad (3)$$

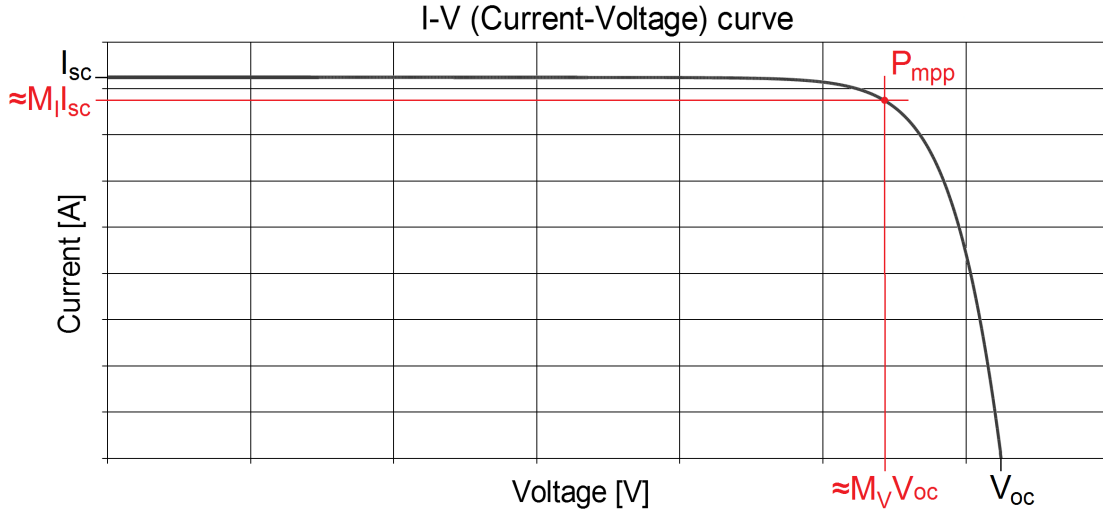


Figure 14: Working principle of VMPPT and CMPPT

The size of the parameters M_V and M_I depends on the PV technology. Typical values for M_V are in the range of 0.7 to 0.8, and for M_I values lie between 0.75 and 0.95. We can determine suitable values, for example, by experiments and simulations. In the case of VMPPT, once we have determined the parameter M_V , we measure the open-circuit voltage (V_{oc}) periodically. Therefore, we disconnect the photovoltaics from the dc/dc converter. However, VMPPT is also possible without these measurements. The parameters V_{oc} and I_{sc} are only approximations; in reality, we never operate exactly in the MPP. However, the advantage of VMPPT and CMPPT are low implementation costs. CMPPT is slightly more difficult to implement than VMPPT [55], [57].

3.4.4 Changes in Ambient Conditions

A part of the MPPT algorithms which are summarised in [55] respond to changes in ambient conditions. Moreover, photovoltaics age over time and the performance decreases in terms of parameters such as the open-circuit voltage (V_{oc}) and the short-circuit current (I_{sc}). Some MPPT algorithms do not consider these kinds of changes. However, for example, if the solar radiation changes quickly, some algorithms can cause failures, as shown on the example of the P&O algorithm in Figure 15.

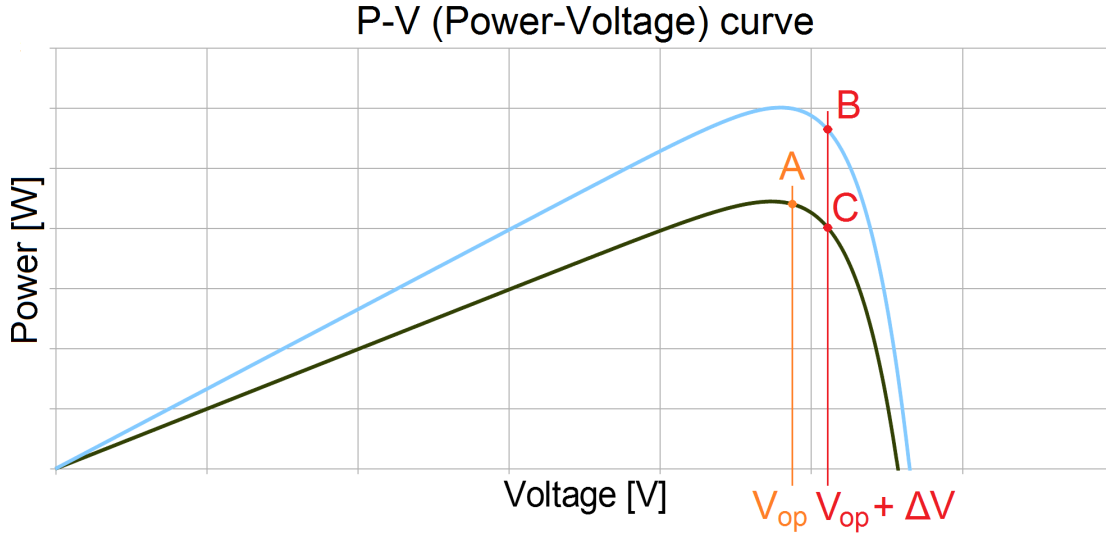


Figure 15: Problem of the P&O algorithm with fast changing ambient conditions

We start in point A and perform a perturbation ΔV . We end up in point B if the ambient conditions change and in point C if the ambient conditions remain unchanged. In point C, we make the right decision and reverse the perturbation due to the decreased power. In point B, we obtain an increase in power and keep the size and sign of perturbation. If the solar radiation continues to increase, we continue to move off the MPP. This problem can be avoided if a more complex version of the P&O algorithm is applied which uses three-point weight comparisons [55].

3.4.5 Choice of the suitable MPPT Algorithm

As mentioned above, the choice of the suitable MPPT algorithm is difficult due to differences in the requirements of MPPT techniques [55]. For example, MPPT algorithm *a* has a better performance than MPPT algorithm *b*, but has a higher power consumption for its hardware. Furthermore, strategy *c* can be more suitable for fast changing ambient conditions than strategy *b*. However, we can classify algorithms based on the following factors:

- control complexity
- power converter structure
- sensed parameters (voltage, current, solar radiation, temperature)
- convergence speed
- periodic tuning

3.5 Simulation Models for PV Cells

3.5.1 Purpose of Simulating Photovoltaics

In this section, different simulation models for photovoltaics are reviewed which allow the inclusion of photovoltaics as a power source in circuit simulations. In general, PV simulation models are required to compute the I-V curve as shown in Figure 10. Furthermore, we can modify the solar radiation level and temperature to calculate the output behaviour under different ambient conditions as illustrated in Figure 11. Consequently, the P-V curve, which is presented in Figure 13, can also be obtained. Altogether, this helps us to verify the output power of our photovoltaics on the one hand and to design suitable electronics such as dc/dc converters on the other.

In general, PV simulation models can be implemented by the use of LabVIEW™ [54], MATLAB/Simulink® [58], and SPICE [59]. For example, in the case of WSN nodes, predictions can be made with the help of simulation models to describe the possible life time enhancement by the use of solar energy as an additional power source. Forecasting the possible energy amount of solar energy requires ambient data such as solar radiation and temperature levels. It is worth noting that in some applications solar energy cannot be used as a primary energy source, because of its non-stable energy output.

A single PV cell provides a certain level of output voltage and current. Increasing the output power requires the connection of two PV cells either in series or in parallel to double the possible output power level. In the simulation, we included two factors which considered the configuration or type of interconnection of the photovoltaics. On one hand, this is the factor of how many PV are connected in series N_s and, on the other hand, N_p which represents the amount of PV cells which are connected in parallel. For a single PV cell, N_s and N_p are equal to 1. Basically, different interconnections do not change the shape of the I-V curve, but the scale of the x-axis (series connection) or y-axis (parallel connection).

3.5.2 Different Types of Simulation Models

We used different types of models that were dependant on the available information from the PV cells. In short, we can obtain the required parameters, such as the open-circuit voltage (V_{oc}) and the short-circuit current (I_{sc}), from the manufacturers datasheet of the photovoltaics. Additionally, we can assume certain parameters with typical values to establish simulations. For a higher degree of accuracy, parameter identification techniques are used to estimate more suitable values for parameters [58], [60].

3.5.3 PV Simulation Model: Ideal Model

The ideal model allows a simulation with only few parameters [58], [61–63]. However, the accuracy of the simulation is reduced and if compared with experimental measurements, an error can be obtained. In this simulation model, the PV cell is considered as a current source which produces a photocurrent (I_{ph} [A]) in direct proportion to the solar radiation level, and a diode; as shown in Figure 16. The output current (I_{out} [A]) is restricted by the diode current (I_d [A]) and can be calculated as follows:

$$I_{out} = N_p I_{ph} - N_p I_d \quad (4)$$

which is, with the Shockley diode equation:

$$I_{out} = N_p I_{ph} - N_p I_s \left(e^{\frac{qV_{out}}{N_s A k T_c}} - 1 \right) \quad (5)$$

where I_s [A] is the saturation current of the PV cell, q is the charge of an electron which is 1.6×10^{-19} C, V_{out} is the output voltage of the circuit, k is Boltzmann's constant which is 1.38×10^{-23} K, and A is the ideality factor of the p-n junction. The photocurrent (I_{ph}) is obtained by

$$I_{ph} = I_{sc,ref} \left(1 + K_I (T_c - T_{ref}) \right) \frac{\lambda}{\lambda_{ref}} \quad (6)$$

where $I_{sc,ref}$ [A] is the short-circuit current of the cell under reference conditions, K_I [%/K] is the current temperature coefficient, $T_{c,ref}$ [K] is the temperature of the PV cell under reference conditions, and λ_{ref} [W/m²] is the solar radiation level under reference conditions. Furthermore, the saturation current (I_s) of the cell is obtained by

$$I_s = I_{rs} \left(\frac{T_c}{T_{ref}} \right)^3 e^{\left(\frac{1}{T_{ref}} - \frac{1}{T_c} \right)} \quad (7)$$

where I_{rs} [A] is the reverse saturation current of the PV cell, and E_g [eV] is the band gap energy of the semiconductor material. The reverse saturation current (I_{rs}) is calculated by

$$I_{rs} = \frac{I_{sc}}{e^{\frac{qV_{oc,ref}(1+K_V(T_c-T_{ref}))}{N_s A k T_c}} - 1}} \quad (8)$$

where $V_{oc,ref}$ [V] is the open-circuit voltage of the cell at reference conditions, and K_V [%/K] is the voltage temperature coefficient.

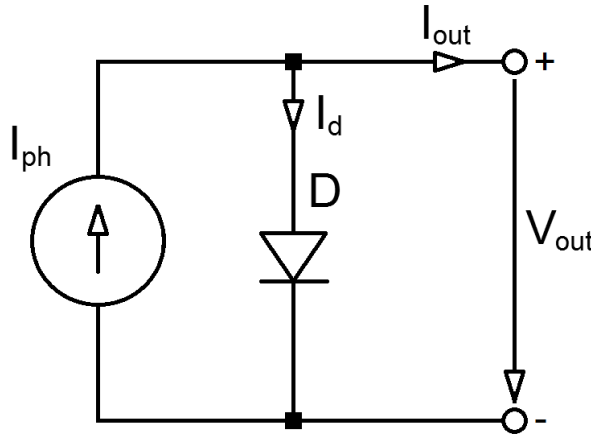


Figure 16: PV simulation model: Ideal model

3.5.4 PV Simulation Model: Simplified Model

For a higher degree of accuracy, a series resistance (R_s) can be considered which represents the internal resistance, in particular, the current path through the semiconductor material, the contacts, the metal grid and current collecting bus. This parameter can vary through different applications of PV cells. The equivalent circuit is shown in Figure 17 [58], [63]. The loss of the series resistance (R_s) is included in Equation (5) as follows:

$$I_{out} = N_p I_{ph} - N_p I_s \left(e^{\frac{q(N_p V_{out} + N_s I_{out} R_s)}{N_p N_s A k T c}} - 1 \right) \quad (9)$$

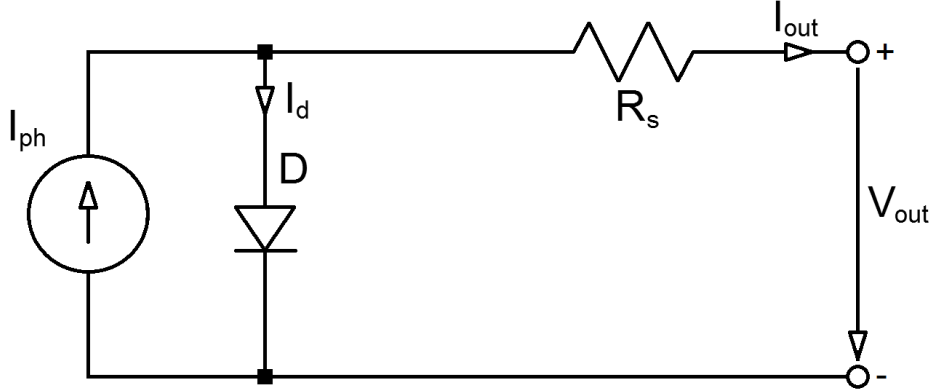


Figure 17: PV simulation model: Simplified model

3.5.5 PV Simulation Model: Practical Model

For monocrystalline PV cells, the practical model provides a good accuracy of simulations. A shunt resistance (R_{sh}) is included into the model, which represents the leakage current of the PV cell. The equivalent circuit of the practical model is shown in Figure 18 [58], [63], [64]. An influence of the shunt resistance (R_{sh}) is considered in Equation (5).

$$I_{out} = N_p I_{ph} - N_p I_s \left(e^{\frac{q(N_p V_{out} + N_s I_{out} R_s)}{N_p N_s A k T c}} - 1 \right) - \frac{N_p V_{out} + I_{out} R_s}{R_{sh}} \quad (10)$$

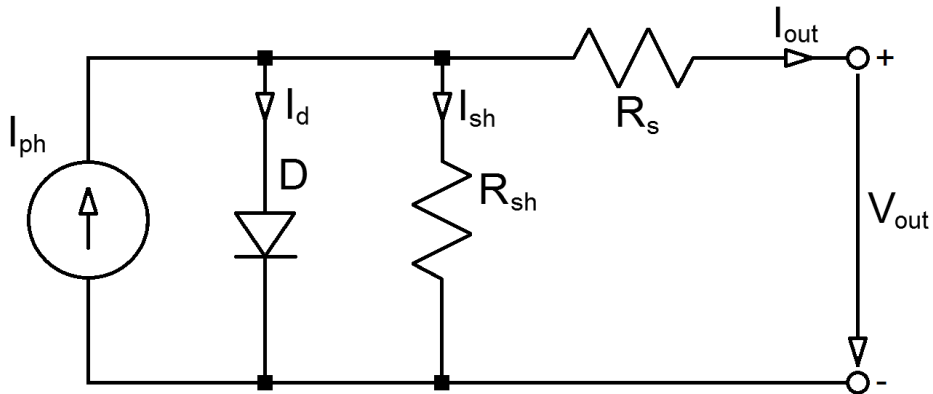


Figure 18: PV simulation model: Practical model

3.5.6 PV Simulation Model: Double Exponential Model

The double exponential model is useful for the simulation of PV cells made out of polycrystalline silicon and can also be used for photovoltaics made out of amorphous silicon [59], [65], [66]. Here, diode D_1 considers the diffusion process of the minority carriers into the depletion layer, and diode D_2 takes into account the recombination in the space region of the p-n junction. The equivalent circuit is given in Figure 19. The consideration of a second diode brings a second diode current into Equation (10) of the practical model. The output current (I_{out}) can now be obtained as follows:

$$I_{out} = N_p I_{ph} - N_p I_{s1} \left(e^{\frac{q(N_p V_{out} + N_s I_{out} R_s)}{N_p N_s A_1 k T_c}} - 1 \right) - N_s I_{s2} \left(e^{\frac{q(N_p V_{out} + N_s I_{out} R_s)}{N_p N_s A_2 k T_c}} - 1 \right) - \frac{\frac{N_p}{N_s} V_{out} + I_{out} R_s}{R_{sh}} \quad (11)$$

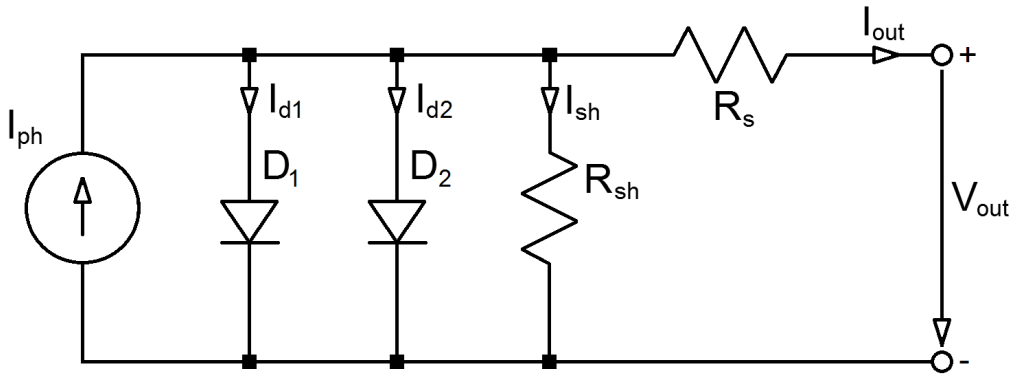


Figure 19: PV simulation model: Double exponential model

4 Electric Range Extender (ERE)

4.1 Purpose of the Electric Range Extender

In conventional vehicles with ICEs, all electricity is produced with the help of an alternator. As discussed in Chapter 2, the amount of electric loads is directly proportional to the fuel consumption. Moreover, the alternator needs to be designed for peak power, since the auxiliary battery is a buffer and can support the on-board power grid only for a restricted period of time. In plug-in full HEV, electricity from the power grid can be used to charge the high-voltage battery beforehand, so that the amount of electricity is reduced which needs to be produced by the ICE during driving.

Photovoltaics produce electricity directly and the gained energy can be supplied to different load units in the vehicle. The function of the powertrain is critical and several ECUs are needed to ensure the safety of the driver [26]. This is why PV energy is more suitable for loads from comfort systems such as air conditioning system, which also demands a significant amount of energy. The opportunities vary, for example, with the type of hybridisation of the HEV. Moreover, the demands of the driver can play a significant role and can be taken into account to optimise the use of photovoltaics. The main idea of installing PV on the top of vehicles is to extend the pure-electric driving distance [5]. This is why the PV installation is referred as an electric range extender (ERE).

4.2 Integration of Photovoltaics in Automobiles

As mentioned above, the amount of output power depends on the environmental conditions such as solar radiation and temperature levels. Additionally, the area for solar energy production on automobiles is limited. Photovoltaics can be deployed, for example, on the roof of a vehicle, however if PV cells fall into shadow, the output power is lowered significantly [67]. Thus, it is not possible to produce enough solar energy for the propulsion of the vehicle directly [7], [8]. Hence, it is advisable to buffer the gained solar energy, for example, in an ultracapacitor.

Figure 20 illustrates one possible way of integrating photovoltaics as a range extender within automobiles [68]. The PV installation is considered as a non-constant power source due to the fluctuations in available power with changing ambient conditions. A suggestion is made to use the range extender as a regenerative load and thereby reduce the overall load for the high-voltage battery [68]. In this way, the required energy from the load units can be obtained as follows:

$$E_{load} = E_{bat} + E_{ere} \quad (12)$$

where E_{load} is the energy demand of load units, E_{bat} is the energy which is provided by the high-voltage battery, and E_{ere} is the energy which is gained from the PV installation. Unfortunately, this way of connecting the range extender to the on-board power supply restricts the possible use of photovoltaics to charge the high-voltage battery. In particular, in parking conditions, photovoltaics can be used to partly charge the high-voltage battery during a longer period of time.

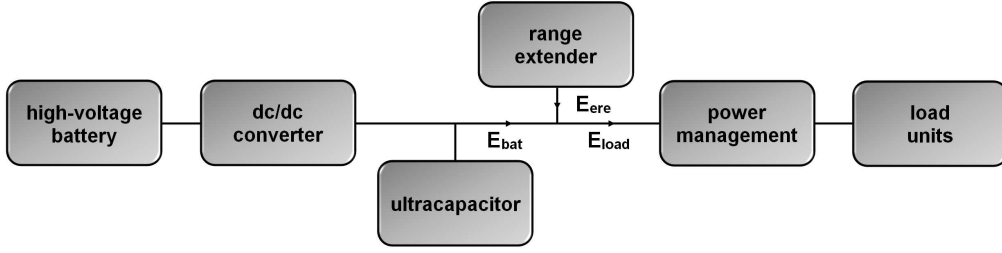


Figure 20: Connection of range extender and ultracapacitor, structure 1

Figure 21 presents the system's topology in which an ultracapacitor is installed between the on-board power supply and the range extender. This proposal can help to compensate variations in the available power from the photovoltaics. For example, the ultracapacitor can be disconnected from the on-board power supply under unfavourable environmental conditions. However, if the stored energy in the ultracapacitor is suitably high enough it can be used to support the high-voltage battery for a particular amount of time. Furthermore, energy from the PV installation can be still collected and is not lost, for example, if the load units do not require power. It is worth noting that the energy demand of load units is much higher during operating conditions than in parking conditions.

In Figure 21, the PV energy is stored in the high-voltage battery if the energy demand of load units is low. E_{ere} can be either routed to the dc/dc converter to charge the high-voltage battery or to load units, as obtained in Equation (13). Here, the power management system plays an important role and can significantly contribute to reduce the amount of losses which occur due the use of the dc/dc converter ($\eta_{dc/dc}$) to charge/discharge the high-voltage battery (η_{bat}).

$$E_{ere} = E_{bat} + E_{load} \quad (13)$$

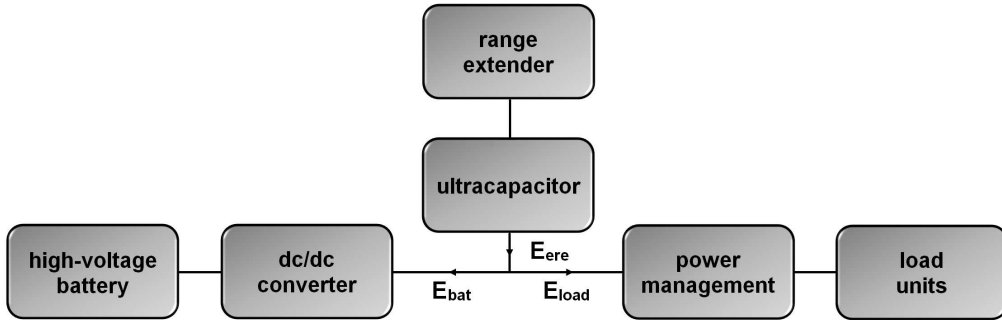


Figure 21: Connection of range extender and ultracapacitor, structure 2

Due to the fluctuations in available power, it is advisable to study the circumstances for photovoltaics on the top of vehicles. In this work, photovoltaics are combined with monitoring units which observe the changes in environmental conditions. A proposal is made that the monitoring system can be also applied to improve the amount of power under unfavourable ambient conditions. Monitoring the amount of solar radiation provides helpful data for the control of PV cells on the one hand, and EMS on the other. Additionally, statements can be made on how much solar energy can be produced over a certain period of time.

The main idea is to use the limited amount of area on automobiles as much as possible. Moreover, the unique circumstances which make the environment for photovoltaics different than on conventional applications, such as the roof of buildings, are taken into account. The monitoring system is an independent system which does not measure the amount of power from photovoltaics directly. In this way, photovoltaics do not have to be disconnected to obtain information on the available amount of power. Table 7 summarises the opportunities for EREs if they are connected to the on-board power grid in the way as illustrated in Figure 21.

Table 7: Possible use of EREs in different HEVs

hybrid system type	voltage level	possible use of ERE
none (ICE)	14 V	minimal
micro-HEV	14–42 V	minimal
mild-HEV	42–120 V	modest
medium-HEV	144 V	good
full-HEV	200 V	best

4.3 Space for Photovoltaics on Top of Vehicles

As mentioned above, the space on automobiles is limited for solar energy production. This chapter evaluates the potential to produce electricity with the help of photovoltaics on today's BEVs and HEVs. In this work, the focus lies on the roof for installing PV cells. Since the area is restricted, the recommendation is made to mount superior PV cells on the vehicle. Figure 22 shows the PV cell which was used within the experiments. The PV cell has a pseudo-square shape and is made out of monocrystalline silicon. Under standard test conditions (STC), which are a solar radiation level (λ) of 1000 W/m^2 and a PV cell temperature (T_c) of $298 \text{ K} = 25 \text{ }^\circ\text{C}$, one PV cell provides an open-circuit voltage (V_{oc}) of about 0.6 V and provides a short-circuit current (I_{sc}) of about 8.6 A . The tolerance limits of the PV manufacturer are $\pm 5 \%$.



Figure 22: PV cell within experiments

Table 8: Parameters of one PV cell

Parameter	Value
P_{mpp} [W]	4.140
V_{mpp} [V]	0.515
I_{mpp} [A]	8.039
P_{th} [W]	5.273
V_{oc} [V]	0.613
I_{sc} [A]	8.602
FF	0.785

$\lambda = 1000 \text{ W/m}^2$; $T_c = 298 \text{ K}$; standard test conditions

4.4 Power of Photovoltaics on Top of Vehicles

On average, the size of the roof of today's EVs and HEVs varies between 1.5 to 2 m². Figure 23 illustrates the experimental vehicle of this research which is a Toyota Prius [1], [5], [8]. It can be seen that the dimensions of the car are not constant from the front to the rear of the vehicle. One PV cell measures 156 times 156 millimetres. In the following step, we calculate the number of PV cells which we can install on top of the Toyota Prius theoretically. However, additional space is required for wiring and interconnecting single PV cells (60 mm in the length and 10 mm in the width). This is why the remaining space is calculated at the end.

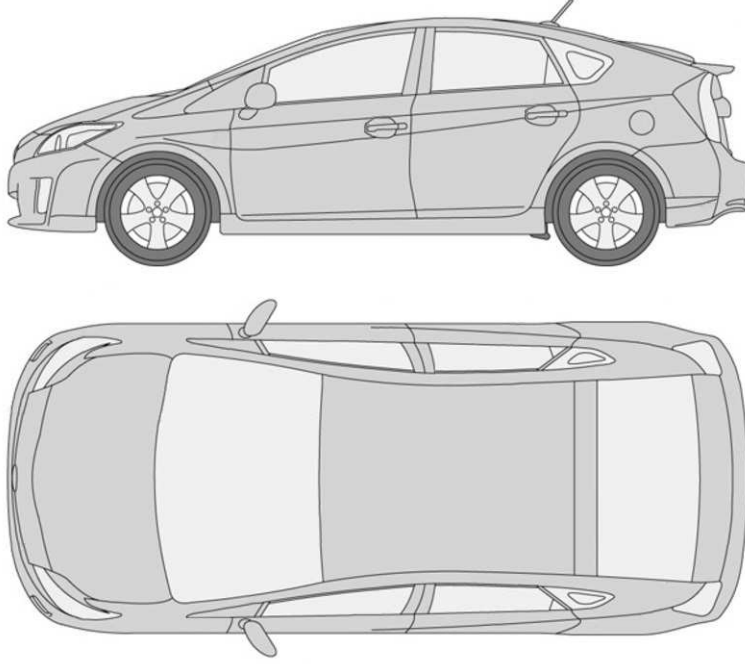


Figure 23: Shape of the roof of the Toyota Prius

Size of the roof of the Toyota Prius:

Length: $l_{roof} = 1680$ mm

Width: $w_{roof} = 1080$ mm

Available area: $A_{roof} = l_{roof} \times w_{roof} = 1.81$ m²

Size of one PV cell:

Length: $l_{PV} = 156$ mm

Width: $w_{PV} = 156$ mm

Covered area of one PV cell: $A_{PV} = 0.024$ m²

Theoretical number of PV cells: $n_{cells} = A_{roof} / A_{PV} = 75$

Amount of PV cells for the Toyota Prius:

PV cells per length: $n_{cells,l} = l_{roof} / l_{PV} = 10$

PV cells per width: $n_{cells,w} = w_{roof} / w_{PV} = 6$

Possible number of PV cells: $n_{cells} = n_{cells,l} \times n_{cells,w} = 60$

Amount of remaining space:

Length: 1680 mm - 1560 mm = 120 mm

Width: 1080 mm - 936 mm = 144 mm

Figure 24 illustrates the PV cells in the way they can be deployed on the roof of the vehicle. Row number (01) is located at the front of the car, the windscreen, while the last row, number (10), is at the rear of the car, the boot. In conventional flat PV modules there is about 1.5 to 2 millimetres space between PV cells, both, horizontally and vertically. At the edge of the array of PV cells, there is an additional space required for wiring and connecting the PV cells to the terminal. As calculated above, it is possible to estimate the remaining space if 60 PV cells are installed on the roof of the Toyota Prius. There will be about 7 millimetres space between the PV cells horizontally and about 27 millimetres vertically. This allows the installation of small sensors next to PV cells which are needed for the monitoring units.

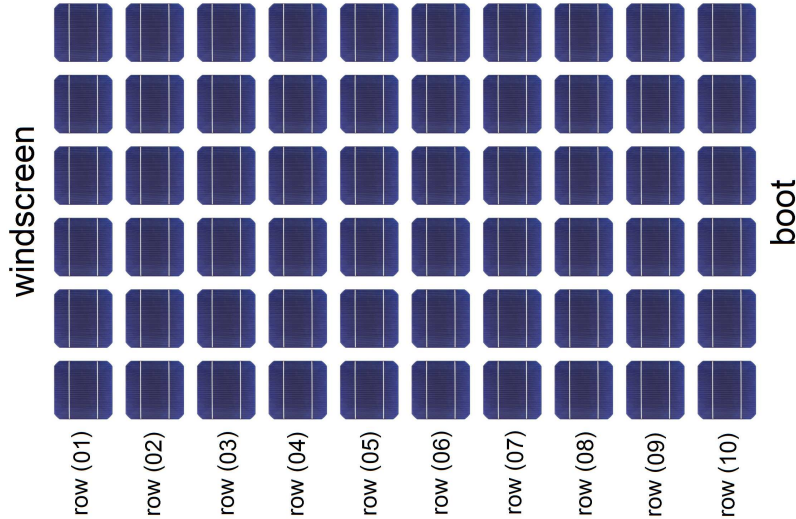


Figure 24: Possible amount of PV cells on the roof of a Toyota Prius

The output power of photovoltaics increases, for example, if two PV cells are connected either in series or in parallel: In series V_{oc} doubles, while in parallel I_{sc} doubles [15]. In the following stage, we can calculate the output power of the entire installation in the MPP, independent from the way interconnections of PV cells are established [8]. Values are given if all PV cells operate under standard test conditions. Afterwards, the amount of available power is compared with the nominal power of conventional available, high-cost, high-power PV modules.

Installed PV power on the roof:

Theoretical power of one PV cell: $P_{th,cell} = 5.273 \text{ W}$

Theoretical power of all PV cells: $P_{th} = 60 \times P_{th,cell} = 316 \text{ W}$

Power in MPP of all PV cells: $P_{mpp} = FF \times P_{th} \approx 248 \text{ W}$

Commonly, high-cost, high-power PV modules contain 36, 48, 54, 60, 72, and 80 PV cells, which are connected in series with each other. The nominal power which is provided in the datasheet of the PV manufacturer is the power in the MPP (P_{mpp}). Table 9 summarises typical parameters of these flat PV modules which are available on the market at the moment. Furthermore, the amount of PV cells in the system structure is provided as well as the amount of PV cell horizontally and vertically. The average power of individual PV cells in modules is lower due to wiring losses and mismatches on output performances of individual PV cells [15].

Table 9: System structures of conventional, high-cost, high-power PV modules

Nominal Power	Amount of PV cells	$n_{cells,l}$	$n_{cells,w}$
140 W	36	9	4
185 W	48	8	6
220 W	54	9	6
245 W	60	10	6
290 W	72	12	6
320 W	80	10	8

In the mentioned PV modules above, the power of one PV cell in a module varies between 3.85 and 4.08 W. For the Toyota Prius, one PV module with 60 PV cells, 10 x 6 (in $n_{cells,l} \times n_{cells,w}$), with a nominal power of 245 W could be used. Unfortunately, due to the curved surface of the roof of the Toyota Prius, it is not possible to mount large flat PV modules. Instead, single PV cells can be mounted onto the roof to avoid stiff structures of PV modules. In [1], the performance of a flexible PV module was analysed. These types of PV modules are suitable for curved surfaces, since they can be curved up to 30 % [1].

However, the investigated flexible PV module is made out of 32 monocrystalline PV cells and provides a short-circuit current (I_{sc}) of 5.1 A [1]. Compared with the performance of flat PV modules, one PV cell of the module provides a power of 2.5 W; which is about 37.5 % less on power. In comparable work, three PV modules are used, each one providing a nominal power of 125 W, combined supplying a nominal power of 375 W [7]. Since the roof of the investigated test vehicle, a Proton Savvy, measures about 1.65 m², PV modules are mounted probably also on other sections of the car, such as the bonnet. However, photovoltaics should be integrated into automobiles in such a way so that no negative impacts on the aerodynamics occur.

4.5 Shape of the Roof of Today's Automobiles

In practice, the output power of the photovoltaics will be lower as calculated before. This is due to the non-linear curved shape nature of the roof of today's vehicles. In particular, on modern vehicles, the orientation of each PV cell towards the sun differs. The target of this work is to investigate the potential of photovoltaics if they are aligned under different longitudinal angles towards the sun. Therefore, three more vehicles are taken into consideration to evaluate the amount of solar energy which can be produced on top of vehicles. The highest difference in orientation ($\Delta\beta$) is given between the first and the last row of PV cells, obtained as follows:

$$\Delta\beta = \beta_{row(01)} - \beta_{row(j)} \quad (14)$$

where $\beta_{row(01)}$ is the orientation of the PV cell in the first row, number (01), with respect to the horizontal plane, for example the street, and $\beta_{row(j)}$ is the orientation of the PV cell in the last row with respect to the horizontal plane. Figure 25 illustrates the measurement of the angles of PV cells. The sign of β is considered to be positive for the front of the car and negative for the rear of the car. The output power of PV modules varies as a result of the different longitudinal angles of PV cells. This work investigates different system structures of photovoltaics in order to minimise mismatches between PV cells in different rows.

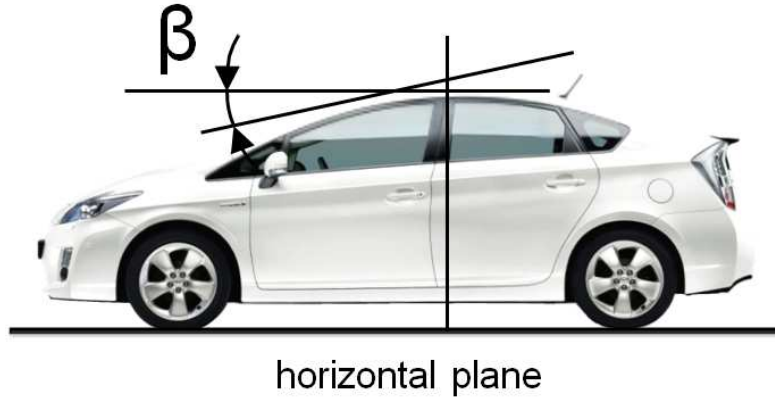


Figure 25: Angles of PV cells on the roof of the Toyota Prius

4.5.1 Roof of the Toyota Prius

Table 10 summarises the longitudinal angles of the experimental vehicle, a Toyota Prius. It can be seen that within each row PV cells have a different angle towards the sun i.e the difference from one cell to the next is non-constant. Additionally, the shape of the roof differs from the front to the rear of the vehicle. The impact on the output performance also varies due to different solar altitudes during the day. Moreover, variations in the amount of output power depend on the position of the car towards the sun. Obtained from Table 10, $\Delta\beta = 26^\circ$.

Table 10: Longitudinal angles of PV cells on the roof of a Toyota Prius

(01)	(02)	(03)	(04)	(05)	(06)	(07)	(08)	(09)	(10)
15 °	12 °	9 °	3 °	2 °	0 °	- 3 °	- 7 °	- 9 °	- 11 °

4.5.2 Roof of the Toyota Auris

The Toyota Auris is a compact hatchback and comparable in price, size and features with the Toyota Prius. However, the shape of the roof of the Toyota Auris differs from the Toyota Prius, as shown in Figure 26. This is why this car has been taken into account in this study. Again, the area of the roof is calculated and the amount of PV cells is estimated. Compared with the Toyota Prius, the Toyota Auris allows one additional row of PV cells to be installed. Even though the roof of the Toyota Auris is longer than the one from the Toyota Prius, the difference in longitudinal angles is lower. Obtained from Table 11, $\Delta\beta = 23^\circ$.

Table 11: Longitudinal angles of PV cells on the roof of a Toyota Auris

(01)	(02)	(03)	(04)	(05)	(06)	(07)	(08)	(09)	(10)	(11)
15 °	8 °	5 °	4 °	0 °	0 °	- 3 °	- 4 °	- 6 °	- 7 °	- 8 °

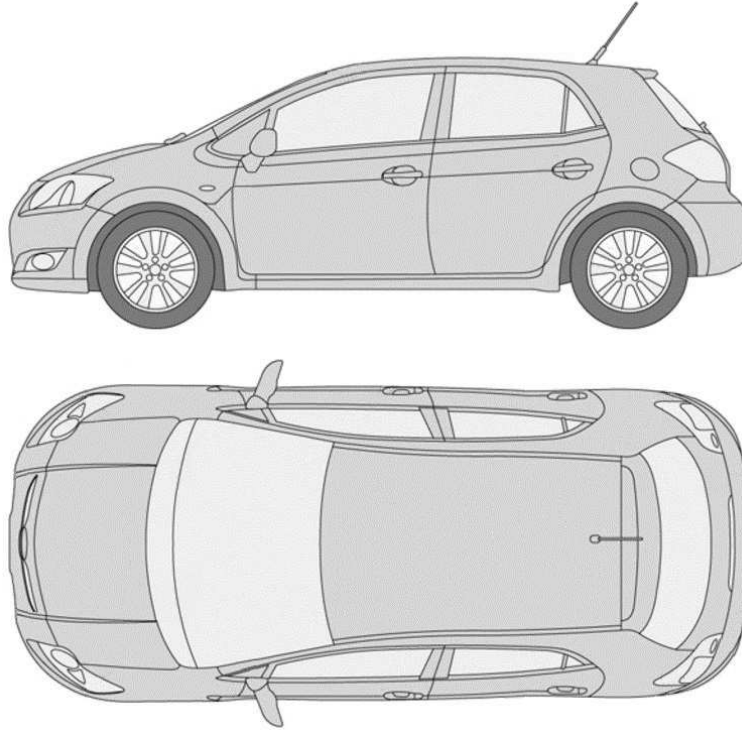


Figure 26: Shape of the roof of the Toyota Auris

Size of the roof of the Toyota Auris:

$$\text{Available area: } A_{\text{roof}} = l_{\text{roof}} \times w_{\text{roof}} = 1810 \text{ mm} \times 1050 \text{ mm} = 1.90 \text{ m}^2$$

Amount of PV cells for the Toyota Auris:

$$\text{Possible number of PV cells: } n_{\text{cells}} = n_{\text{cells},l} \times n_{\text{cells},w} = 11 \times 6 = 66$$

Amount of remaining space:

$$\text{Length: } 1810 \text{ mm} - 1716 \text{ mm} = 94 \text{ mm}$$

$$\text{Width: } 1050 \text{ mm} - 936 \text{ mm} = 114 \text{ mm}$$

4.5.3 Roof of the Nissan Leaf

The Nissan Leaf is a BEV and provides pure-electric propulsion for a range of up to 135 km. At present, it is one of the most known battery-powered electric vehicles and the world's best-selling BEV which is suitable for driving on highways at higher speed levels. The shape of the roof of the Nissan Leaf differs from other cars in that way that it has a long decline over the half of the length of roof. However, the size of the roof is the smallest of the four investigated vehicles. Calculated from Table 12, $\Delta\beta = 18^\circ$.

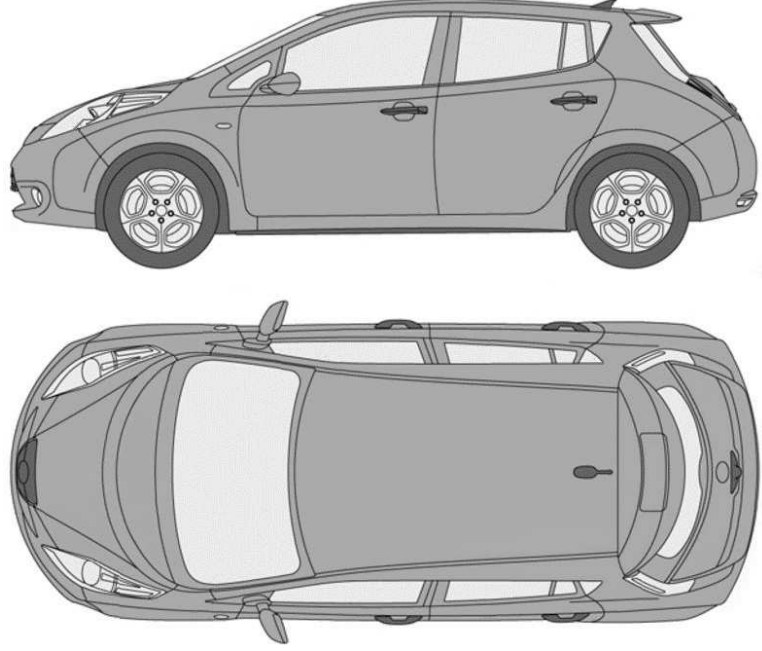


Figure 27: Shape of the roof of the Nissan Leaf

Table 12: Longitudinal angles of PV cells on the roof of a Nissan Leaf

(01)	(02)	(03)	(04)	(05)	(06)	(07)	(08)	(09)	(10)
12°	5°	3°	0°	-3°	-4°	-5°	-5°	-5°	-6°

Size of the roof of the Nissan Leaf:

$$\text{Available area: } A_{\text{roof}} = l_{\text{roof}} \times w_{\text{roof}} = 1742 \text{ mm} \times 923 \text{ mm} = 1.61 \text{ m}^2$$

Amount of PV cells for the Nissan Leaf:

$$\text{Possible number of PV cells: } n_{\text{cells}} = n_{\text{cells},l} \times n_{\text{cells},w} = 10 \times 5 = 50$$

Amount of remaining space:

$$\text{Length: } 1742 \text{ mm} - 1560 \text{ mm} = 182 \text{ mm}$$

$$\text{Width: } 923 \text{ mm} - 780 \text{ mm} = 143 \text{ mm}$$

4.5.4 Roof of the Citroën C-Zero

The Citroën C-Zero is a BEV and similar to the Mitsubishi MiEV and Peugeot iOn as they have the same size [1]. These circumstances allow exchanging batteries between these three vehicles. One of the differences between those vehicles lies in the available extras for customers. The Citroën C-Zero offers an operating range of up to 130 km with a high-voltage battery capacity of 16 kWh and up to 160 km with a high-voltage battery capacity of 20 kWh. Calculated from Table 13, $\Delta\beta = 23^\circ$.

Table 13: Longitudinal angles of PV cells on the roof of a Citroën C-Zero

(01)	(02)	(03)	(04)	(05)	(06)	(07)	(08)	(09)
15°	10°	5°	4°	-1°	-2°	-5°	-7°	-8°

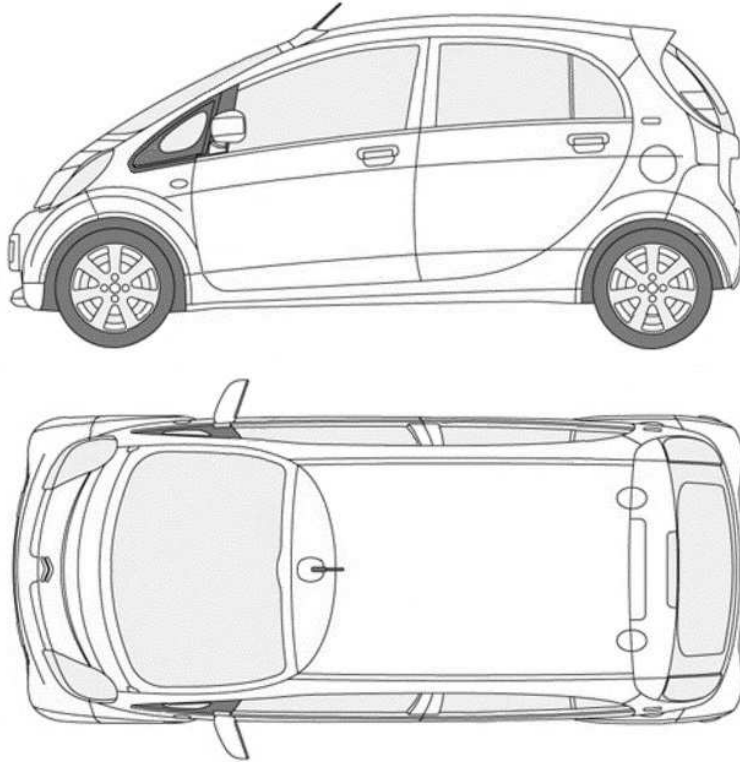


Figure 28: Shape of the roof of the Citroën C-Zero

Size of the roof of the Citroën C-Zero:

$$\text{Available area: } A_{\text{roof}} = l_{\text{roof}} \times w_{\text{roof}} = 1574 \text{ mm} \times 977 \text{ mm} = 1.54 \text{ m}^2$$

Amount of PV cells for the Citroën C-Zero:

$$\text{Possible number of PV cells: } n_{\text{cells}} = n_{\text{cells},l} \times n_{\text{cells},w} = 9 \times 6 = 54$$

Amount of remaining space:

$$\text{Length: } 1574 \text{ mm} - 1404 \text{ mm} = 170 \text{ mm}$$

$$\text{Width: } 977 \text{ mm} - 936 \text{ mm} = 41 \text{ mm}$$

4.5.5 Comparison of the Amount of Space and Power

Here, the opportunities of the different BEVs and HEVs to install photovoltaics are compared with each other. Comparison of the amount of PV cells per m² and nominal power per m² are useful for the next chapter, in which effective areas of PV cells are calculated and impacts of longitudinal angles are analysed. In Table 14, it can be seen that on top of a Toyota Auris 25 % more PV cells can be installed than on the roof of a Nissan Leaf. However, the shape of a Citroën C-Zero can be used in the most efficient way, since the amount of PV cells per m² is the highest.

Table 14: Comparison of opportunities on different HEVs and BEVs

	Toyota Prius	Toyota Auris	Nissan Leaf	Citroën C-Zero
$\Delta\beta$	26 °	23 °	18 °	23 °
l_{roof}	1680 mm	1810 mm	1742 mm	1574 mm
w_{roof}	1080 mm	1050 mm	923 mm	977 mm
A_{roof}	1.81 m ²	1.90 m ²	1.61 m ²	1.54 m ²
$n_{cells,l}$	10	11	10	9
$n_{cells,w}$	6	6	5	6
n_{cells}	60	66	50	54
P_{th}	316 W	368 W	264 W	285 W
P_{mpp}	248 W	273 W	207 W	224 W

PV cells per m²:

$$\text{Toyota Prius: } n_{cells} / A_{roof} = 60 / 1.81 \text{ m}^2 = 33 \text{ PV cells per m}^2$$

$$\text{Toyota Auris: } n_{cells} / A_{roof} = 66 / 1.90 \text{ m}^2 = 34 \text{ PV cells per m}^2$$

$$\text{Nissan Leaf: } n_{cells} / A_{roof} = 50 / 1.61 \text{ m}^2 = 31 \text{ PV cells per m}^2$$

$$\text{Citroën C-Zero: } n_{cells} / A_{roof} = 54 / 1.54 \text{ m}^2 = 35 \text{ PV cells per m}^2$$

Nominal power per m²:

$$\text{Toyota Prius: } P_{mpp} / A_{roof} = 248 \text{ W} / 1.81 \text{ m}^2 = 137 \text{ W per m}^2$$

$$\text{Toyota Auris: } P_{mpp} / A_{roof} = 273 \text{ W} / 1.90 \text{ m}^2 = 143 \text{ W per m}^2$$

$$\text{Nissan Leaf: } P_{mpp} / A_{roof} = 207 \text{ W} / 1.61 \text{ m}^2 = 128 \text{ W per m}^2$$

$$\text{Citroën C-Zero: } P_{mpp} / A_{roof} = 224 \text{ W} / 1.54 \text{ m}^2 = 145 \text{ W per m}^2$$

4.6 The Effective Area of Photovoltaics

4.6.1 Orientation of Photovoltaics towards the Sun

As discussed above, the five or six PV cells in each row face the sun under different longitudinal angles. It is worth noting that PV cells produce the highest amount of output power under given environmental conditions if the beam radiation arrives under a 90 degree angle, as illustrated in Figure 29. Since the solar altitude is varying throughout the day and also depends on the geographical location, the position of PV cells needs to be alternated continuously so that the maximum amount of power can be obtained.

However, tracking the sun with PV cells requires additional effort and increases costs of PV installations. As a compromise, PV cells can be aligned under suitable angles towards the sun so that reasonable output performances can be achieved throughout the day without alternating the position of PV cells. On buildings with flat roofs, the opportunity is given to choose the angle of photovoltaics wisely. On houses with gable or saddle roofs, the degree of freedom to vary the angle of photovoltaics is much lower. Similarly, on top of cars, the orientation of PV cells towards the sun depends on the shape of the roof.

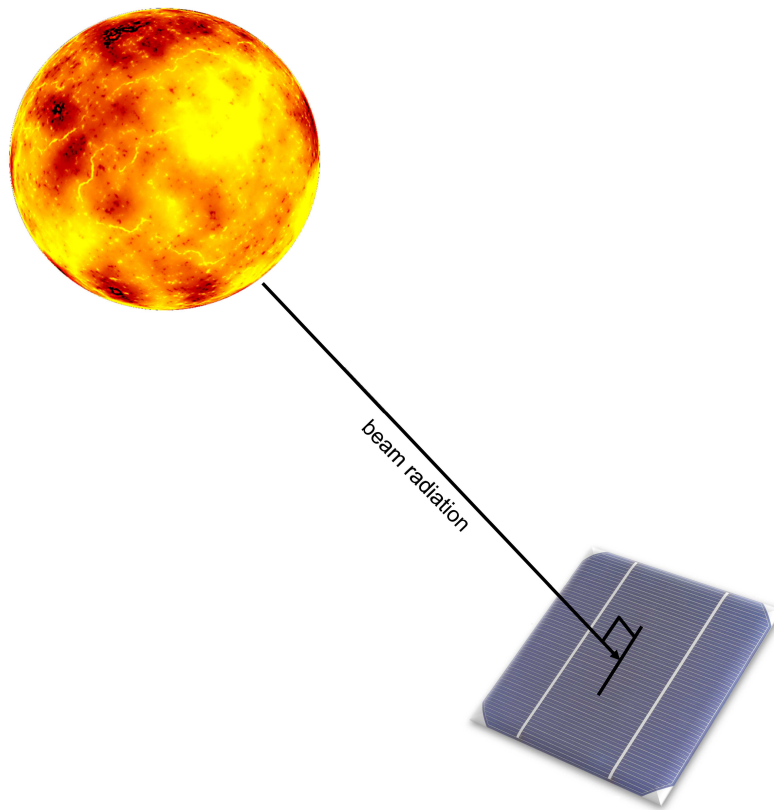


Figure 29: Illustration of the optimal orientation of one PV cell towards the sun

4.6.2 Calculation of the Effective Area of Photovoltaics

The effective area (A_{eff}) is used as an indicator and provides information about the potential of PV installations on automobiles. The factor is useful to estimate the amount of power which can be gained under the given longitudinal angles in comparison to the power which could be obtained if PV cells had optimal angles towards the sun. The effective area is calculated in MATLAB[®] by using the perpendicular area. Here, diffuse illumination is not taken into account.

$$A_{eff} = \cos(\alpha + \beta - 90^\circ) \quad (15)$$

where A_{eff} is the effective area of the PV cell and α is the sun elevation. As discussed above, the longitudinal angles of the available rows with PV cells vary on different BEVs and HEVs. Table 15-18 present the calculated effective areas at different solar altitudes. In Table 15, it can be seen that in the morning and evening when the solar altitude is low, the effective area of PV cells which are not facing the sun is relatively low. If the sun is directly above the car at a 90 degree angle, the effective areas of PV cells in different rows are very similar. Then, the highest effective area is obtained in row number (06) in which $\beta = 0^\circ$. In this row, the orientation of PV cells becomes optimal.

Table 15: Calculated effective areas of PV cells on top of a Toyota Prius

	solar altitude angle								
	20 °	40 °	60 °	75 °	90 °	105 °	120 °	140 °	160 °
row (01)	57.36 %	81.92 %	96.59 %	100.00 %	96.59 %	86.60 %	70.71 %	42.26 %	8.72 %
row (02)	52.99 %	78.80 %	95.11 %	99.86 %	97.81 %	89.10 %	74.31 %	46.95 %	13.92 %
row (03)	48.48 %	75.47 %	93.36 %	99.45 %	98.77 %	91.35 %	77.71 %	51.50 %	19.08 %
row (04)	39.07 %	68.20 %	89.10 %	97.81 %	99.86 %	95.11 %	83.67 %	60.18 %	29.24 %
row (05)	37.46 %	66.91 %	88.29 %	97.44 %	99.94 %	95.63 %	84.80 %	61.57 %	30.90 %
row (06)	34.20 %	64.28 %	86.60 %	96.59 %	100.00 %	96.59 %	86.60 %	64.28 %	34.20 %
row (07)	29.24 %	60.18 %	83.87 %	95.11 %	99.86 %	97.81 %	89.10 %	68.20 %	39.07 %
row (08)	22.50 %	54.46 %	79.86 %	92.71 %	99.25 %	99.02 %	92.05 %	73.14 %	45.40 %
row (09)	19.08 %	51.50 %	77.71 %	91.35 %	98.76 %	99.45 %	93.36 %	75.47 %	48.48 %
row (10)	15.64 %	48.48 %	75.47 %	89.88 %	98.16 %	99.76 %	94.55 %	77.71 %	51.50 %

Table 16: Calculated effective areas of PV cells on top of a Toyota Auris

	solar altitude angle								
	20 °	40 °	60 °	75 °	90 °	105 °	120 °	140 °	160 °
row (01)	57.36 %	81.92 %	96.59 %	100.00 %	96.59 %	86.60 %	70.71 %	42.26 %	8.72 %
row (02)	46.95 %	74.31 %	92.72 %	99.25 %	99.03 %	92.05 %	78.80 %	52.99 %	20.79 %
row (03)	42.26 %	70.71 %	90.63 %	98.48 %	99.62 %	93.97 %	81.92 %	57.36 %	25.88 %
row (04)	40.67 %	69.47 %	89.88 %	98.16 %	99.76 %	94.55 %	82.90 %	58.78 %	27.56 %
row (05)	34.20 %	64.28 %	86.60 %	96.59 %	100.00 %	96.59 %	86.60 %	64.28 %	34.20 %
row (06)	34.20 %	64.28 %	86.60 %	96.59 %	100.00 %	96.59 %	86.60 %	64.28 %	34.20 %
row (07)	29.24 %	60.18 %	83.87 %	95.11 %	99.86 %	97.81 %	89.10 %	68.20 %	39.07 %
row (08)	27.56 %	58.78 %	82.90 %	94.55 %	99.76 %	98.16 %	89.88 %	69.47 %	40.67 %
row (09)	24.19 %	55.92 %	80.90 %	93.36 %	99.45 %	98.77 %	91.35 %	71.93 %	43.84 %
row (10)	22.50 %	54.46 %	79.86 %	92.71 %	99.25 %	99.02 %	92.05 %	73.14 %	45.40 %
row (11)	20.79 %	52.99 %	78.80 %	92.05 %	99.03 %	99.25 %	92.72 %	74.31 %	46.95 %

Table 17: Calculated effective areas of PV cells on top of a Nissan Leaf

	solar altitude angle								
	20 °	40 °	60 °	75 °	90 °	105 °	120 °	140 °	160 °
row (01)	52.99 %	78.80 %	95.11 %	99.86 %	97.81 %	89.10 %	74.31 %	46.95 %	13.92 %
row (02)	42.26 %	70.71 %	90.63 %	98.48 %	99.62 %	93.97 %	81.92 %	57.36 %	25.88 %
row (03)	39.07 %	68.20 %	89.10 %	97.81 %	99.86 %	95.11 %	83.67 %	60.18 %	29.24 %
row (04)	34.20 %	64.28 %	86.60 %	96.59 %	100.00 %	96.59 %	86.60 %	64.28 %	34.20 %
row (05)	29.24 %	60.18 %	83.87 %	95.11 %	99.86 %	97.81 %	89.10 %	68.20 %	39.07 %
row (06)	27.56 %	58.78 %	82.90 %	94.55 %	99.76 %	98.16 %	89.88 %	69.47 %	40.67 %
row (07)	25.88 %	57.36 %	81.92 %	93.97 %	99.62 %	98.48 %	90.63 %	70.71 %	42.26 %
row (08)	25.88 %	57.36 %	81.92 %	93.97 %	99.62 %	98.48 %	90.63 %	70.71 %	42.26 %
row (09)	25.88 %	57.36 %	81.92 %	93.97 %	99.62 %	98.48 %	90.63 %	70.71 %	42.26 %
row (10)	24.19 %	55.92 %	80.90 %	93.36 %	99.45 %	98.77 %	91.35 %	71.93 %	43.84 %

Table 18: Calculated effective areas of PV cells on top of a Citroën C-Zero

	solar altitude angle								
	20 °	40 °	60 °	75 °	90 °	105 °	120 °	140 °	160 °
row (01)	57.36 %	81.92 %	96.59 %	100.00 %	96.59 %	86.60 %	70.71 %	42.26 %	8.72 %
row (02)	50.00 %	76.60 %	93.97 %	99.62 %	98.48 %	90.63 %	76.60 %	50.00 %	17.36 %
row (03)	42.26 %	70.71 %	90.63 %	98.48 %	99.62 %	93.97 %	81.92 %	57.36 %	25.88 %
row (04)	40.67 %	69.47 %	89.88 %	98.16 %	99.76 %	94.55 %	82.90 %	58.78 %	27.56 %
row (05)	32.56 %	62.93 %	85.72 %	96.13 %	99.98 %	97.03 %	87.46 %	65.61 %	35.84 %
row (06)	30.90 %	61.57 %	84.80 %	95.63 %	99.94 %	97.43 %	88.29 %	66.91 %	37.46 %
row (07)	25.88 %	57.36 %	81.92 %	93.97 %	99.62 %	98.48 %	90.63 %	70.71 %	42.26 %
row (08)	22.50 %	54.46 %	79.86 %	92.71 %	99.25 %	99.02 %	92.05 %	73.14 %	45.40 %
row (09)	20.79 %	52.99 %	78.80 %	92.05 %	99.03 %	99.25 %	92.72 %	74.31 %	46.95 %

4.6.3 Statistical Evaluation of the Calculated Effective Area of Photovoltaics

Here, a statistical evaluation of the calculated effective areas is presented. In this way, the opportunity is given to analyse the impact of the orientation of PV cells on top of the investigated BEVs and HEVs. Therefore, mean values of the effective areas (\bar{A}_{eff}) of rows with PV cells are calculated. Furthermore, the solar altitude angles are divided into two intervals, $[0^\circ, 90^\circ]$ and $[90^\circ, 180^\circ]$, respectively. These intervals offer the possibility to investigate the potential output power of PV cells if either the front or the back of the car faces the sun.

At first, the opportunities of a Toyota Prius are discussed. Figure 30 illustrates the effective PV cell areas at different solar altitude angles. Under a low solar altitude angle of $[0^\circ, 20^\circ]$, the first three rows have a significantly higher effective area than the other rows, while under a solar altitude angle of $[160^\circ, 180^\circ]$ the three last rows attain the largest effective area. As seen in Figure 30, the greatest variation in effective areas between different rows is observed between row number (03) and (04). Moreover, it is notable that the effective areas obtained in row number (08), (09), and (10) are very similar. This visualisation of effective areas at different solar altitude angles is helpful for choosing the proper interconnection of PV cells on the roof of vehicles.

Toyota Prius: statistical evaluation, \bar{A}_{eff}

row (01): $77.78 \pm 22.88 \%$ $[0^\circ, 90^\circ]$	$47.17 \pm 34.03 \%$ $[90^\circ, 180^\circ]$
row (02): $75.33 \pm 24.62 \%$ $[0^\circ, 90^\circ]$	$50.41 \pm 34.02 \%$ $[90^\circ, 180^\circ]$
row (03): $72.66 \pm 26.32 \%$ $[0^\circ, 90^\circ]$	$53.65 \pm 33.75 \%$ $[90^\circ, 180^\circ]$
row (04): $66.75 \pm 29.56 \%$ $[0^\circ, 90^\circ]$	$60.21 \pm 32.32 \%$ $[90^\circ, 180^\circ]$
row (05): $65.69 \pm 30.08 \%$ $[0^\circ, 90^\circ]$	$61.31 \pm 31.95 \%$ $[90^\circ, 180^\circ]$
row (06): $63.51 \pm 31.09 \%$ $[0^\circ, 90^\circ]$	$63.51 \pm 31.09 \%$ $[90^\circ, 180^\circ]$
row (07): $60.21 \pm 32.32 \%$ $[0^\circ, 90^\circ]$	$66.75 \pm 29.56 \%$ $[90^\circ, 180^\circ]$
row (08): $55.83 \pm 33.41 \%$ $[0^\circ, 90^\circ]$	$70.78 \pm 27.42 \%$ $[90^\circ, 180^\circ]$
row (09): $53.65 \pm 33.75 \%$ $[0^\circ, 90^\circ]$	$72.66 \pm 26.32 \%$ $[90^\circ, 180^\circ]$
row (10): $51.49 \pm 33.96 \%$ $[0^\circ, 90^\circ]$	$74.46 \pm 25.19 \%$ $[90^\circ, 180^\circ]$

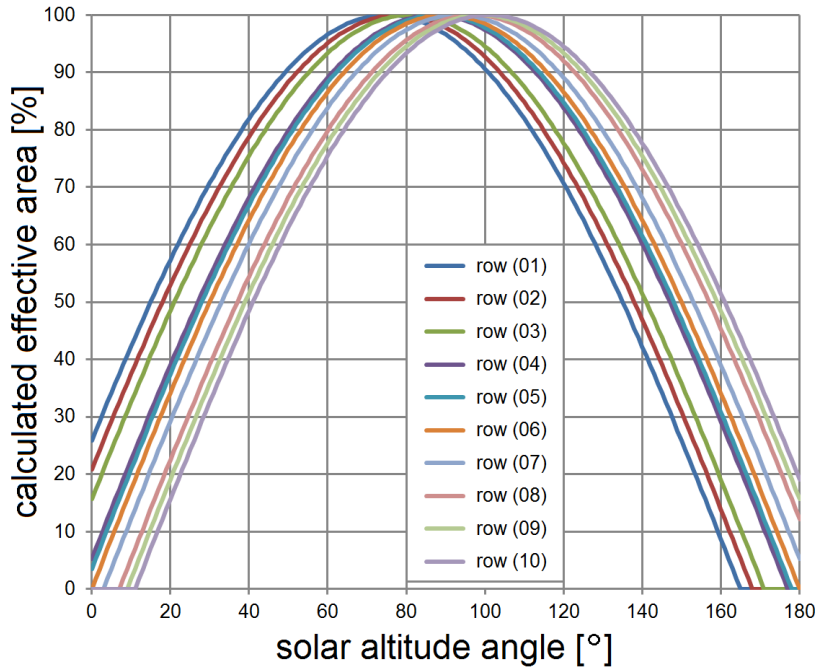


Figure 30: Effective PV cell areas on top of a Toyota Prius

On top of a Toyota Auris, the largest difference in effective areas is obtained between row number (01) and (02). The reason for this is the strong curve which the roof makes towards the windscreen. As seen in Figure 31, beside the notable difference between the first two rows, the differences from other rows to one other are lower compared to the variations on top of a Toyota Prius. If PV cells are connected with each other, these circumstances are expected to lower the mismatches within PV modules. The Toyota Auris provides the longest PV installation of the considered BEVs and HEVs in this investigation.

Toyota Auris: statistical evaluation, \bar{A}_{eff}

row (01): 77.78 ± 22.88 % [0 °, 90 °]	47.17 ± 34.03 % [90 °, 180 °]
row (02): 71.73 ± 26.88 % [0 °, 90 °]	54.74 ± 33.60 % [90 °, 180 °]
row (03): 68.80 ± 28.51 % [0 °, 90 °]	58.02 ± 32.94 % [90 °, 180 °]
row (04): 67.79 ± 29.04 % [0 °, 90 °]	59.12 ± 32.65 % [90 °, 180 °]
row (05): 63.51 ± 31.09 % [0 °, 90 °]	63.51 ± 31.09 % [90 °, 180 °]
row (06): 63.51 ± 31.09 % [0 °, 90 °]	63.51 ± 31.09 % [90 °, 180 °]
row (07): 60.21 ± 32.32 % [0 °, 90 °]	66.75 ± 29.56 % [90 °, 180 °]
row (08): 59.12 ± 32.65 % [0 °, 90 °]	67.79 ± 29.04 % [90 °, 180 °]
row (09): 56.93 ± 33.20 % [0 °, 90 °]	69.80 ± 27.97 % [90 °, 180 °]
row (10): 55.83 ± 33.41 % [0 °, 90 °]	70.78 ± 27.42 % [90 °, 180 °]
row (11): 54.74 ± 33.60 % [0 °, 90 °]	71.73 ± 26.88 % [90 °, 180 °]

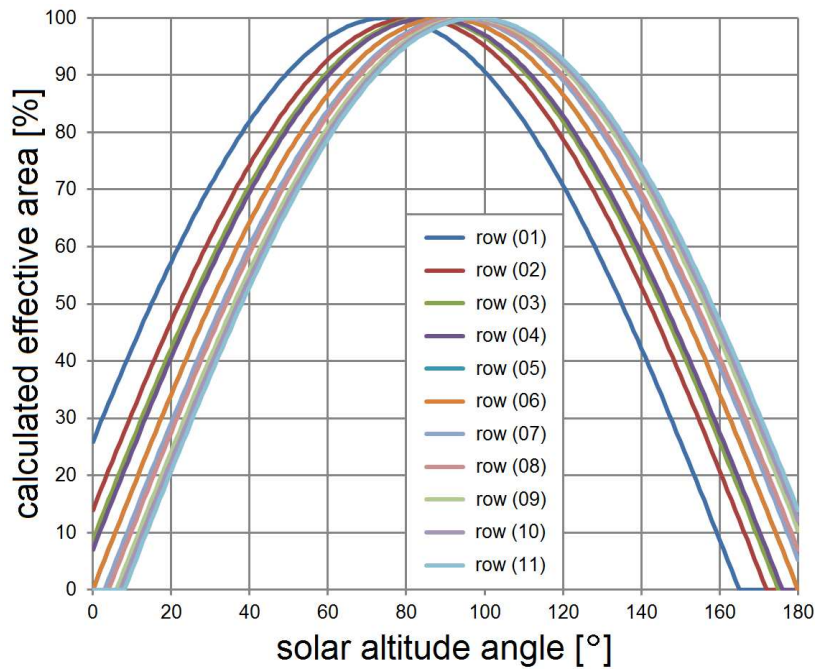


Figure 31: Effective area of PV cells on top of a Toyota Auris

Similar to the Toyota Auris, there is a large variation in the effective area between row number (01) and (02). However, as seen in Figure 32, the mismatch between other rows is small due to the very similar orientation of PV cells towards the sun. The longitudinal angle of PV cells varies only a few degrees at the rear of the car. Therefore, PV modules can be established, in which all PV cells face the sun under the same angle or with very similar angles. Beside row (01), even under low solar altitude angles, for example $\alpha = 10^\circ$ or $\alpha = 170^\circ$, all PV cells provide output power. Unfortunately, the available area to deploy PV cells is the smallest compared to other EVs and HEVs in this research work. This situation results in the smallest amount on nominal power due to the possibility of installing 31 PV cells per m^2 .

Nissan Leaf: statistical evaluation, \bar{A}_{eff}

row (01): $75.33 \pm 24.62\%$ [$0^\circ, 90^\circ$]	$50.41 \pm 34.02\%$ [$90^\circ, 180^\circ$]
row (02): $68.80 \pm 28.51\%$ [$0^\circ, 90^\circ$]	$58.02 \pm 32.94\%$ [$90^\circ, 180^\circ$]
row (03): $66.75 \pm 29.56\%$ [$0^\circ, 90^\circ$]	$60.21 \pm 32.32\%$ [$90^\circ, 180^\circ$]
row (04): $63.51 \pm 31.09\%$ [$0^\circ, 90^\circ$]	$63.51 \pm 31.09\%$ [$90^\circ, 180^\circ$]
row (05): $60.21 \pm 32.32\%$ [$0^\circ, 90^\circ$]	$66.75 \pm 29.56\%$ [$90^\circ, 180^\circ$]
row (06): $59.12 \pm 32.65\%$ [$0^\circ, 90^\circ$]	$67.79 \pm 29.04\%$ [$90^\circ, 180^\circ$]
row (07): $58.02 \pm 32.94\%$ [$0^\circ, 90^\circ$]	$68.80 \pm 28.51\%$ [$90^\circ, 180^\circ$]
row (08): $58.02 \pm 32.94\%$ [$0^\circ, 90^\circ$]	$68.80 \pm 28.51\%$ [$90^\circ, 180^\circ$]
row (09): $58.02 \pm 32.94\%$ [$0^\circ, 90^\circ$]	$68.80 \pm 28.51\%$ [$90^\circ, 180^\circ$]
row (10): $56.93 \pm 33.20\%$ [$0^\circ, 90^\circ$]	$69.80 \pm 27.97\%$ [$90^\circ, 180^\circ$]

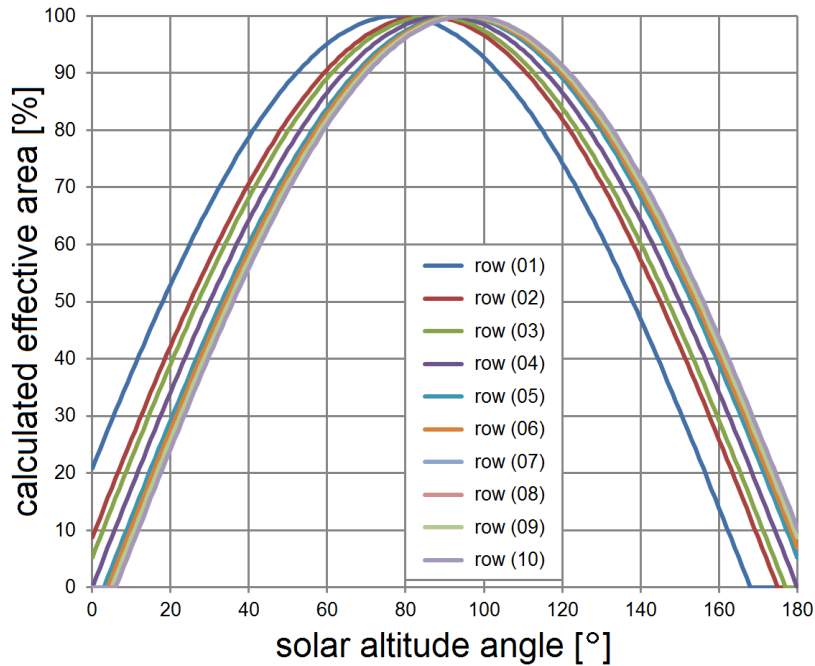


Figure 32: Effective area of PV cells on top of a Nissan Leaf

The shape of a Citroën C-Zero results in larger variations of available effective areas of PV cells. As seen in Figure 33, only in the rear of the car between row number (07) and (08), (08) and (09), the difference in A_{eff} is smaller than between other rows. The cause for this situation is the strong curved shape of the roof of the Citroën C-Zero. As obtained from Table 14, even though the available roof area is the smallest of the investigated EVs and HEVs, there can be still more PV cells installed on the roof than on Nissan Leaf due to the highest possible amount of PV cells per m^2 . However, the nine rows with PV cells is the shortest PV installation within this research work.

Citroën C-Zero: statistical evaluation, \bar{A}_{eff}

row (01): 77.78 ± 22.88 % [0 °, 90 °]	47.17 ± 34.03 % [90 °, 180 °]
row (02): 73.57 ± 25.76 % [0 °, 90 °]	52.57 ± 33.87 % [90 °, 180 °]
row (03): 68.80 ± 28.51 % [0 °, 90 °]	58.02 ± 32.94 % [90 °, 180 °]
row (04): 67.79 ± 29.04 % [0 °, 90 °]	59.12 ± 32.65 % [90 °, 180 °]
row (05): 62.41 ± 31.54 % [0 °, 90 °]	64.91 ± 30.59 % [90 °, 180 °]
row (06): 61.31 ± 31.95 % [0 °, 90 °]	65.69 ± 30.08 % [90 °, 180 °]
row (07): 58.02 ± 32.94 % [0 °, 90 °]	68.80 ± 28.51 % [90 °, 180 °]
row (08): 55.83 ± 33.41 % [0 °, 90 °]	70.78 ± 27.42 % [90 °, 180 °]
row (09): 54.74 ± 33.60 % [0 °, 90 °]	71.73 ± 26.88 % [90 °, 180 °]

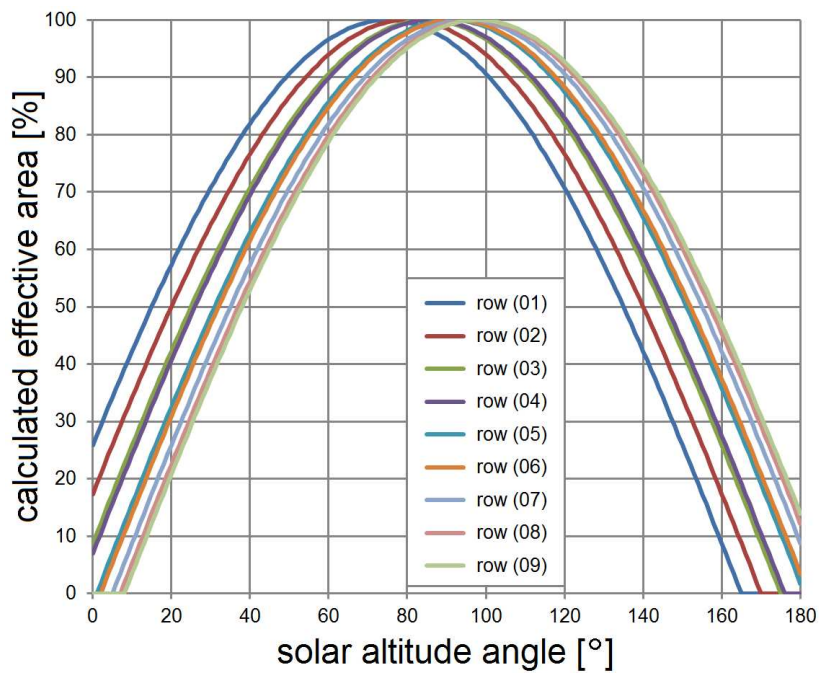


Figure 33: Effective area of PV cells on top of a Citroën C-Zero

4.6.4 Normalisation of the Effective Area of Photovoltaics

For a better comparison, the values in Table 15-18 are normalised by calculating the factor ΔA_{eff} . At a particular solar altitude angle, ΔA_{eff} indicates clearly in which row(s) the PV cells are orientated in the most suitable way towards the sun. The highest value is considered to be 100 % of the possible amount under the given solar altitude and the given orientation of PV cells due to the shape of the roof. As a result, the mismatch caused by the different longitudinal angles of PV cells can be analysed.

$$\Delta A_{eff} = \frac{A_{eff,i}}{A_{eff,max}} \quad \text{whereas } i = (01), (02), \dots, (08), (09), (10)^*, (11)^* \quad (16)$$

* ... if the row number is available

Table 19-22 present the normalised effective areas of the different BEVs and HEVs. The presented values are important for the establishment of interconnections of PV cells. In Table 14, $\Delta\beta$ varies between 18 ° and 26 ° and is in particular influenced by the orientation of the first and last row of PV cells. As seen, for example in Table 19 for a Toyota Prius, under low solar altitudes angles [0 °, 20 °] and [160 °, 180 °] the actual difference in the effective area is 80 % and larger than that. As seen in Table 21, in case of a Nissan Leaf, these variations are smaller compared to the other BEVs and HEVs.

Table 19: Normalised effective areas of PV cells on top of a Toyota Prius

	solar altitude angle								
	20 °	40 °	60 °	75 °	90 °	105 °	120 °	140 °	160 °
row (01)	100.00 %	100.00 %	100.00 %	100.00 %	96.59 %	86.81 %	74.79 %	54.38 %	16.93 %
row (02)	92.38 %	96.19 %	98.47 %	99.86 %	97.81 %	89.31 %	78.59 %	60.42 %	27.03 %
row (03)	84.52 %	92.13 %	96.67 %	99.45 %	98.77 %	91.57 %	82.19 %	66.27 %	37.05 %
row (04)	68.11 %	83.25 %	92.25 %	97.81 %	99.86 %	95.34 %	88.49 %	77.44 %	56.78 %
row (05)	65.31 %	81.68 %	91.41 %	97.44 %	99.94 %	95.86 %	89.69 %	79.23 %	60.00 %
row (06)	59.62 %	78.47 %	89.66 %	96.59 %	100.00 %	96.82 %	91.59 %	82.72 %	66.41 %
row (07)	50.98 %	73.46 %	86.83 %	95.11 %	99.86 %	98.05 %	94.24 %	87.76 %	75.86 %
row (08)	39.23 %	66.48 %	82.68 %	92.71 %	99.25 %	99.26 %	97.36 %	94.12 %	88.16 %
row (09)	33.26 %	62.87 %	80.45 %	91.35 %	98.76 %	99.69 %	98.74 %	97.12 %	94.14 %
row (10)	27.27 %	59.18 %	78.13 %	89.88 %	98.16 %	100.00 %	100.00 %	100.00 %	100.00 %

Table 20: Normalised effective areas of PV cells on top of a Toyota Auris

	solar altitude angle								
	20 °	40 °	60 °	75 °	90 °	105 °	120 °	140 °	160 °
row (01)	100.00 %	100.00 %	100.00 %	100.00 %	96.59 %	87.25 %	76.26 %	56.87 %	18.57 %
row (02)	81.85 %	90.71 %	95.99 %	99.25 %	99.03 %	92.75 %	84.99 %	71.31 %	44.28 %
row (03)	73.68 %	86.32 %	93.83 %	90.63 %	99.62 %	94.68 %	88.35 %	77.19 %	55.12 %
row (04)	70.90 %	84.80 %	93.05 %	89.88 %	99.76 %	95.26 %	89.41 %	79.10 %	58.70 %
row (05)	59.62 %	78.47 %	89.66 %	86.60 %	100.00 %	97.32 %	93.40 %	86.50 %	72.84 %
row (06)	59.62 %	78.47 %	89.66 %	86.60 %	100.00 %	97.32 %	93.40 %	86.50 %	72.84 %
row (07)	50.98 %	73.46 %	86.83 %	83.87 %	99.86 %	98.55 %	96.94 %	93.49 %	86.62 %
row (08)	48.05 %	71.75 %	85.83 %	82.90 %	99.76 %	98.90 %	89.88 %	69.47 %	40.67 %
row (09)	42.17 %	68.26 %	83.76 %	80.90 %	99.45 %	99.52 %	98.52 %	96.80 %	93.38 %
row (10)	39.23 %	66.48 %	82.68 %	79.86 %	99.25 %	99.77 %	99.28 %	98.43 %	96.70 %
row (11)	36.24 %	64.69 %	81.58 %	78.80 %	99.03 %	100.00 %	100.00 %	100.00 %	100.00 %

Table 21: Normalised effective areas of PV cells on top of a Nissan Leaf

	solar altitude angle								
	20 °	40 °	60 °	75 °	90 °	105 °	120 °	140 °	160 °
row (01)	100.00 %	100.00 %	100.00 %	100.00 %	97.81 %	90.21 %	81.35 %	65.27 %	31.75 %
row (02)	79.75 %	89.73 %	95.29 %	98.62 %	99.62 %	95.14 %	89.68 %	79.74 %	59.03 %
row (03)	73.73 %	86.55 %	93.68 %	97.95 %	99.86 %	96.29 %	91.59 %	83.66 %	66.70 %
row (04)	64.54 %	81.57 %	91.05 %	96.73 %	100.00 %	97.79 %	94.80 %	89.36 %	78.01 %
row (05)	55.18 %	76.37 %	88.18 %	95.24 %	99.86 %	99.03 %	97.54 %	94.81 %	89.12 %
row (06)	52.01 %	74.59 %	87.16 %	94.68 %	99.76 %	99.38 %	98.39 %	96.58 %	92.77 %
row (07)	48.84 %	72.79 %	86.13 %	94.10 %	99.62 %	99.71 %	99.21 %	98.30 %	96.40 %
row (08)	48.84 %	72.79 %	86.13 %	94.10 %	99.62 %	99.71 %	99.21 %	98.30 %	96.40 %
row (09)	48.84 %	72.79 %	86.13 %	94.10 %	99.62 %	99.71 %	99.21 %	98.30 %	96.40 %
row (10)	45.65 %	70.96 %	85.06 %	93.49 %	99.45 %	100.00 %	100.00 %	100.00 %	100.00 %

Table 22: Normalised effective areas of PV cells on top of a Citroën C-Zero

	solar altitude angle								
	20 °	40 °	60 °	75 °	90 °	105 °	120 °	140 °	160 °
row (01)	100.00 %	100.00 %	100.00 %	100.00 %	96.61 %	87.25 %	76.26 %	56.87 %	18.57 %
row (02)	87.17 %	93.51 %	97.29 %	99.62 %	98.50 %	91.31 %	82.61 %	67.29 %	36.98 %
row (03)	73.68 %	86.32 %	93.83 %	98.48 %	99.64 %	94.68 %	88.35 %	77.19 %	55.12 %
row (04)	70.90 %	84.80 %	93.05 %	98.16 %	99.78 %	95.26 %	89.41 %	79.10 %	58.70 %
row (05)	56.76 %	76.82 %	88.75 %	96.13 %	100.00 %	97.76 %	94.33 %	88.29 %	76.34 %
row (06)	53.87 %	75.16 %	87.79 %	95.63 %	99.96 %	98.17 %	95.22 %	90.04 %	79.79 %
row (07)	45.12 %	70.02 %	84.81 %	93.97 %	99.64 %	98.17 %	95.22 %	90.04 %	79.79 %
row (08)	39.23 %	66.48 %	82.68 %	92.71 %	99.27 %	99.77 %	99.28 %	98.43 %	96.70 %
row (09)	36.24 %	64.69 %	81.58 %	92.05 %	99.05 %	100.00 %	100.00 %	100.00 %	100.00 %

4.6.5 Measurement of the Theoretical Output Power of Photovoltaics

As shown above, it is simple to calculate the effective areas and normalise the computed results. However, this raises the question are these values a suitable indicator for the amount of power which can be gained based on the established orientation of PV cells towards the sun. Solar radiation level (λ) is directly proportional to the short-circuit current (I_{sc}) and, therefore, to the amount of theoretical power (P_{th}). Furthermore, the effective area correlates to the amount of sunlight which can be collected with the sunlight under the given longitudinal angle, and thus also to P_{th} .

On the Toyota Prius, which is shown in Figure 34, 9 rows of PV cells were installed where each cell row contained five PV cells. As a result, the PV installation consisted of 45 PV cells as the chosen setup allowed the study of the impact of interconnection of PV cells easier. Unfortunately, the lower amount of PV cells affects the computed normalised effective areas for solar altitude angles in the range of $[90^\circ, 180^\circ]$ and so, recalculated values are given in Table 23.



Figure 34: Experimental vehicle

Table 23: Normalised effective areas of PV cells on top of a Toyota Prius (9 rows)

	solar altitude angle								
	20 °	40 °	60 °	75 °	90 °	105 °	120 °	140 °	160 °
row (01)	100.00 %	100.00 %	100.00 %	100.00 %	96.59 %	87.08 %	75.74 %	56.00 %	17.99 %
row (02)	92.38 %	96.19 %	98.47 %	99.86 %	97.81 %	89.59 %	79.60 %	62.21 %	28.71 %
row (03)	84.52 %	92.13 %	96.67 %	99.45 %	98.77 %	91.86 %	83.24 %	68.24 %	39.36 %
row (04)	68.11 %	83.25 %	92.25 %	97.81 %	99.86 %	95.64 %	89.62 %	79.74 %	60.31 %
row (05)	65.31 %	81.68 %	91.41 %	97.44 %	99.94 %	96.16 %	90.83 %	81.58 %	63.74 %
row (06)	59.62 %	78.47 %	89.66 %	96.59 %	100.00 %	97.12 %	92.76 %	85.17 %	70.54 %
row (07)	50.98 %	73.46 %	86.83 %	95.11 %	99.86 %	98.35 %	95.44 %	90.37 %	80.59 %
row (08)	39.23 %	66.48 %	82.68 %	92.71 %	99.25 %	99.57 %	98.60 %	96.91 %	93.65 %
row (09)	33.26 %	62.87 %	80.45 %	91.35 %	98.76 %	100.00 %	100.00 %	100.00 %	100.00 %

In experiments, the open-circuit voltage (V_{oc}) and short-circuit current (I_{sc}) were measured to compute the theoretical amount of output power (P_{th}). The measurement results are also normalised to allow a comparison with the normalised effective areas. This was achieved with the help of factor ΔP_{th} . Here, 100 % represents the maximum amount of theoretical power ($P_{th,max}$), which can be gained from a PV cell in a particular row i under a certain solar altitude angle.

$$\Delta P_{th} = \frac{P_{th,i}}{P_{th,max}} \quad \text{whereas } i = (01), (02), \dots, (08), (09) \quad (17)$$

Figure 35 illustrates the setup of the measurement and how the angle α was obtained. Data was gathered at various solar altitude angles under outdoor environmental conditions. Here, the difference between the calculated normalised effective area (ΔA_{eff}) and the measured normalised theoretical amount of power (ΔP_{th}) are presented. The error $\varepsilon_{results}$ describes how well the calculated percentage values of effective areas match the measured percentage values of power levels.

$$\varepsilon_{results} = \Delta A_{eff} - \Delta P_{th} \quad (18)$$

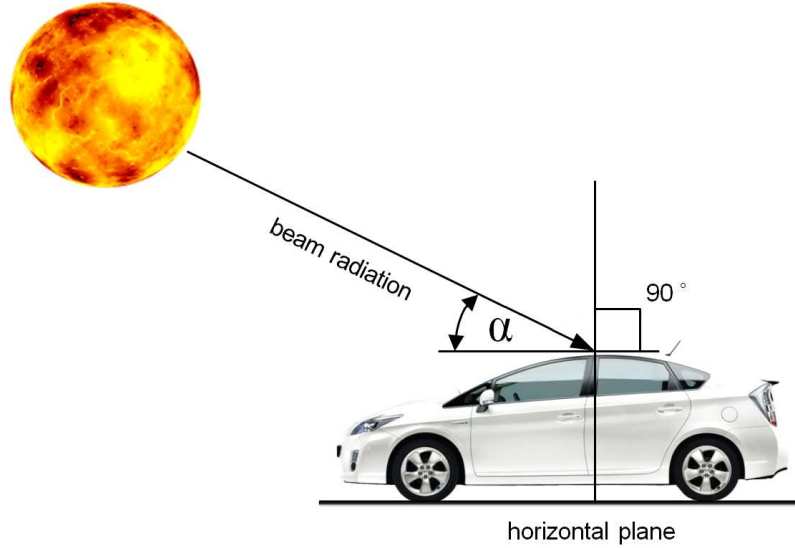


Figure 35: Illustration of the measurement setup

Table 24 presents a statistical evaluation of errors which were obtained from comparisons between calculations and experimental measurements at the same solar altitude angle. It can be seen that the results confirm the possibility to estimate the amount of theoretical power with the computation of effective areas. Hence, additional experiments are not required to estimate the output performance of PV cells on the top of a Toyota Auris, Nissan Leaf and Citroën C-Zero. Instead, the effective areas which are calculated in MATLAB[®] can be used to predict the output power of photovoltaics on top of those vehicles. This opportunity can also be helpful to evaluate the potential for any other curved surface on which photovoltaics can be deployed.

Table 24: Comparison of ΔA_{eff} with ΔP_{th}

	$\varepsilon_{results}$ [%]
row (01)	+ 0.63 ± 1.72
row (02)	- 1.82 ± 1.23
row (03)	- 0.67 ± 1.53
row (04)	- 0.70 ± 1.71
row (05)	+ 1.48 ± 1.47
row (06)	+ 1.76 ± 1.87
row (07)	- 1.02 ± 2.01
row (08)	+ 1.75 ± 1.78
row (09)	- 0.33 ± 1.48

4.7 System Structures of Photovoltaics

4.7.1 Parallel Connections of Photovoltaics

As mentioned above, if two PV cells are connected in parallel, the short-circuit current (I_{sc}) doubles [15]. If a parallel interconnection of several PV cells is established, as illustrated in Figure 36, the new short-circuit current ($I_{sc,new}$ [A]) of the system structure will be the sum of the individual currents, obtained as follows:

$$I_{sc,new} = \sum_{i=1}^n I_{sc,(i)} \quad \text{whereas} \quad i = 1, 2, \dots, n \quad (19)$$

The size of $I_{sc,new}$ depends on the amount n of PV cells which are connected in parallel with each other and on the size of the individual short-circuit currents ($I_{sc,(i)}$ [A]) of PV cells. Variations in output parameters are expected due to tolerance limits from PV manufacturers [15].

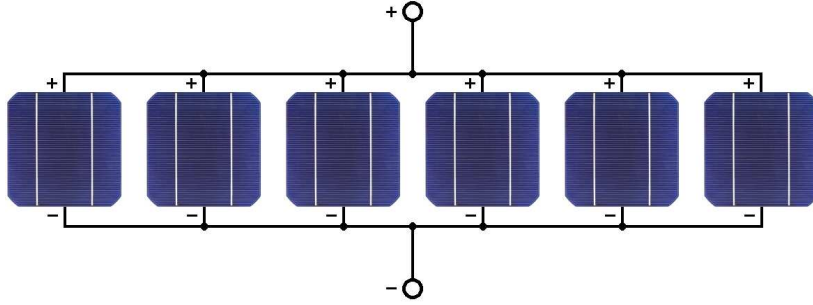


Figure 36: Illustration of parallel connections of photovoltaics

The new open-circuit voltage ($V_{oc,new}$) of a parallel interconnection of n PV cells will be lower than the open-circuit voltage of the PV cell with the highest voltage and larger than the PV cell with the lowest voltage. $V_{oc,new}$ will be an average out of open-circuit voltages ($V_{oc,(i)}$ [V]) of individual PV cells, calculated as follows:

$$V_{oc,new} = \frac{1}{n} \sum_{i=1}^n V_{oc,(i)} \quad \text{whereas} \quad i = 1, 2, \dots, n \quad (20)$$

The new theoretical output power ($P_{th,new}$ [W]) can be calculated in the same way as the output power of one PV cell.

$$P_{th,new} = V_{oc,new} \times I_{sc,new} \quad (21)$$

4.7.2 Series Connections of Photovoltaics

In a series connection of two PV cells, the open-circuit voltage (V_{oc}) doubles. Commonly, series interconnections are established, because of low open-circuit voltages of single PV cells. If several PV cells are interconnected in series, as illustrated in Figure 37, the new open-circuit voltage ($V_{oc,new}$) of the system structure will be the sum of the individual voltages, calculated as follows:

$$V_{oc,new} = \sum_{i=1}^n V_{oc,(i)} \quad \text{whereas } i = 1, 2, \dots, n \quad (22)$$

$V_{oc,new}$ depends on the amount n of PV cells which are connected in series with each other and the size of the individual open-circuit voltages ($V_{oc,(i)}$) of PV cells. Again, variations in output performances are expected due to tolerance limits from PV manufacturers [15].

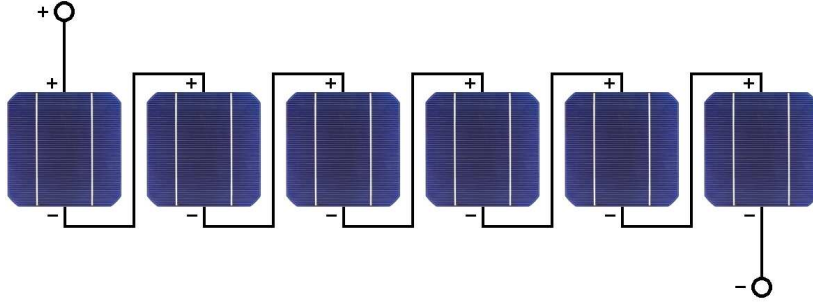


Figure 37: Illustration of series connections of photovoltaics

The new short-circuit current ($I_{sc,new}$) of a series interconnection of n PV cells depends on the PV cell with the lowest short-circuit current ($I_{sc,min}$ [A]) of the system structure. Unfortunately, $I_{sc,new}$ does not increase significantly if the current levels of other PV cells ($I_{sc,(i)}$) are much greater than $I_{sc,min}$.

$$I_{sc,new} = I_{sc,min} \quad (23)$$

The new theoretical output power ($P_{th,new}$ [W]) of the series interconnection can be obtained as follows:

$$P_{th,new} = V_{oc,new} \times I_{sc,min} \quad (24)$$

4.7.3 Amount of PV Cells in PV Modules

As mentioned before, PV cells are commonly connected in series with each other to achieve a suitable high open-circuit voltage (V_{oc}). At the beginning of this research work, interconnections of four and six PV cells were investigated. Therefore, an experimental structure was built in which 24 PV cells can be connected in different ways with each other. Figure 38 presents the schematics of the evaluation platform for measurements. The matrix contains 132 switches; the minimum amount of switches required to have all flexibilities for establishing interconnections. As a result, different amount of PV cells can be connected in different ways with each other. In theory, any possible configuration can be verified by alternating the configuration of the switches. Table 25-28 present the settings for several basic types of connections of PV cells.

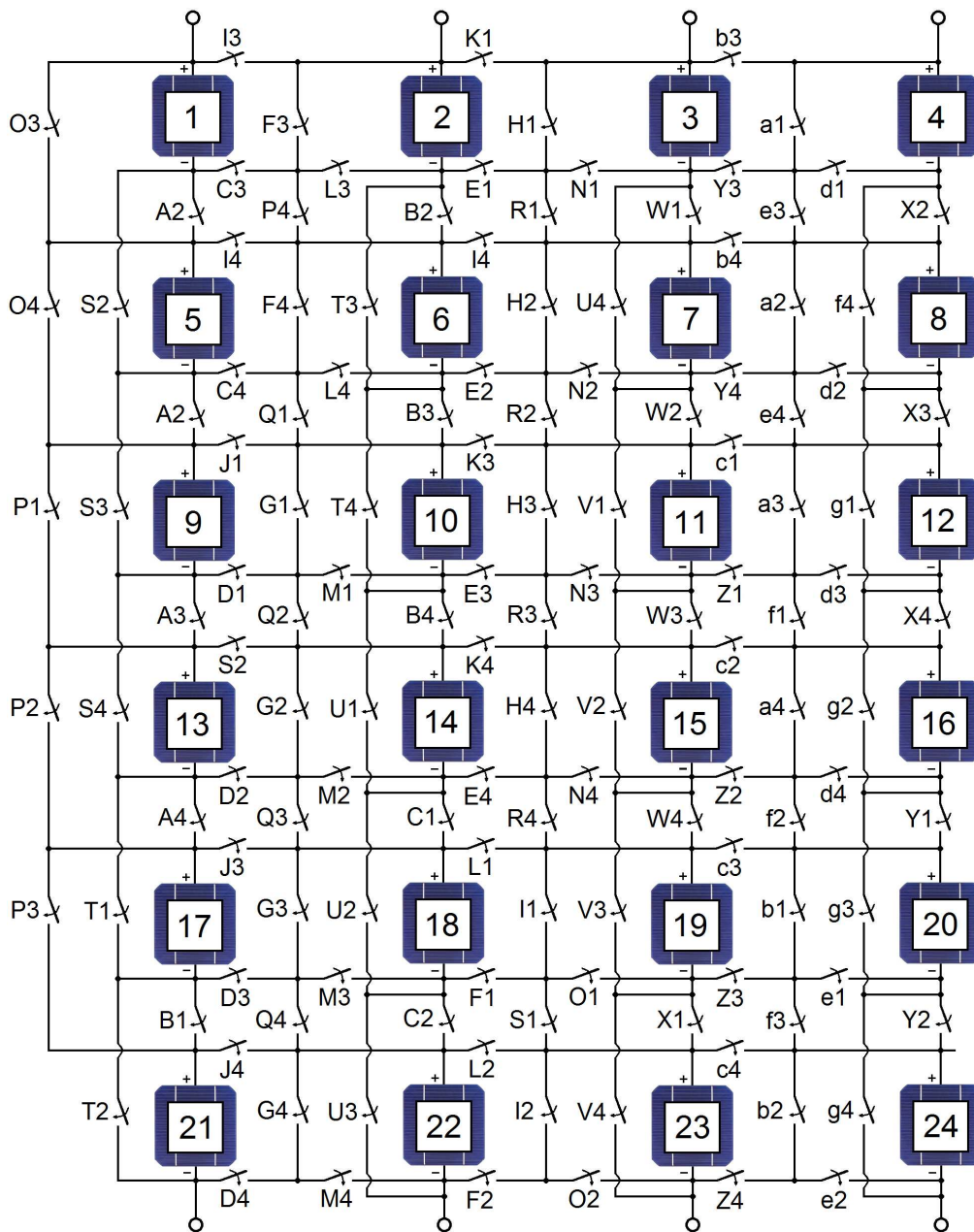


Figure 38: Schematic of the evaluation platform for different types of interconnections

Table 25: Series interconnection of six PV cells, 4 PV modules

PV module (1)	PV cell (01), (05), (09), (13), (17), (21)
PV module (2)	PV cell (02), (06), (10), (14), (18), (22)
PV module (3)	PV cell (03), (07), (11), (15), (19), (23)
PV module (4)	PV cell (04), (08), (12), (16), (20), (24)
A1, A2, A3, A4, B1, B2, B3, B4, C1, C2	on
W1, W2, W3, W4, X1, X2, X3, X4, Y1, Y2	on
all other switches	off

Table 26: Series interconnection of four PV cells, 6 PV modules

PV module (1)	PV cell (01), (02), (03), (04)
PV module (2)	PV cell (05), (06), (07), (08)
PV module (3)	PV cell (09), (10), (11), (12)
PV module (4)	PV cell (13), (14), (15), (16)
PV module (5)	PV cell (17), (18), (19), (20)
PV module (6)	PV cell (21), (22), (23), (24)
C3, C4, D1, D2, D3, D4, E1, E2, E3, E4	on
F1, F2, F3, F4, G1, G2, G3, G4, H1, H2, H3, H4, I1, I2	on
Y3, Y4, Z1, Z2, Z3, Z4, a1, a2, a3, a4, b1, b2	on
all other switches	off

Table 27: Parallel interconnection of six PV cells, 4 PV modules

PV module (1)	PV cell (01), (05), (09), (13), (17), (21)
PV module (2)	PV cell (02), (06), (10), (14), (18), (22)
PV module (3)	PV cell (03), (07), (11), (15), (19), (23)
PV module (4)	PV cell (04), (08), (12), (16), (20), (24)
C3, C4, D1, D2, D3, D4, E1, E2, E3, E4, F1, F2	on
I3, I4, J1, J2, J3, J4, K1, K2, K3, K4, L1, L2, L3, L4	on
M1, M2, M3, M4, N1, N2, N3, N4, O1, O2	on
Y3, Y4, Z1, Z2, Z3, Z4, b3, b4, c1, c2, c3, c4	on
d1, d2, d3, d4, e1, e2	on
all other switches	off

Table 28: Parallel interconnection of four PV cells, 6 PV modules

PV module (1)	PV cell (01), (02), (03), (04)
PV module (2)	PV cell (05), (06), (07), (08)
PV module (3)	PV cell (09), (10), (11), (12)
PV module (4)	PV cell (13), (14), (15), (16)
PV module (5)	PV cell (17), (18), (19), (20)
PV module (6)	PV cell (21), (22), (23), (24)
F3, F4, G1, G2, G3, G4, H1, H2, H3, H4, I1, I2	on
O3, O4, P1, P2, P3, P4, Q1, Q2, Q3, Q4	on
R1, R2, R3, R4, S1, S2, S3, S4, T1, T2, T3, T4	on
U1, U2, U3, U4, V1, V2, V3, V4	on
a1, a2, a3, a4, b1, b2	on
e3, e4, f1, f2, f3, f4, g1, g2, g3, g4	on
all other switches	off

4.7.4 Interconnection of Photovoltaics on the Experimental Vehicle

As seen in Table 27 and 28, more effort is required to establish parallel interconnections than series connections of PV cells. On the experimental vehicle, a Toyota Prius, five PV modules were installed. One PV module contains nine PV cells to achieve an open-circuit voltage (V_{oc}) of about 5 V. Each PV module is connected to a dc/dc boost converter which converts the input voltage (V_{in} [V]) to an output voltage (V_{out} [V]) of about 12 V, which is suitable high enough for the auxiliary on-board power supply. Then, all five PV modules are connected in parallel with each other. On the evaluation platform, a similar type of connection can be established. At first, the series connections are established, as shown in Table 25. Afterwards, the switches D4, F2, I3, K1, M4, O2, Z4, b3, and e2 are closed. As a result, four PV modules with six PV cells are connected in parallel. Similarly, a configuration out of six PV modules with four PV cells can be made.

Figure 39 illustrates the alignment of PV modules on top of the experimental vehicle [8]. There are two PV modules with 9×1 PV cells (in $n_{cells,l} \times n_{cells,w}$) on the outside of the roof and three PV modules with 3×3 PV cells (in $n_{cells,l} \times n_{cells,w}$) on the inside of the roof. Certainly, there are also other, more complicated system structures possible. However, the choice of this configuration allows studying the impacts on the output performance due to different orientations of individual PV cells towards the sun. Especially, the performances of PV module (1) and (5) are of interest, since these PV modules contain PV cells from every row with PV cells [8].

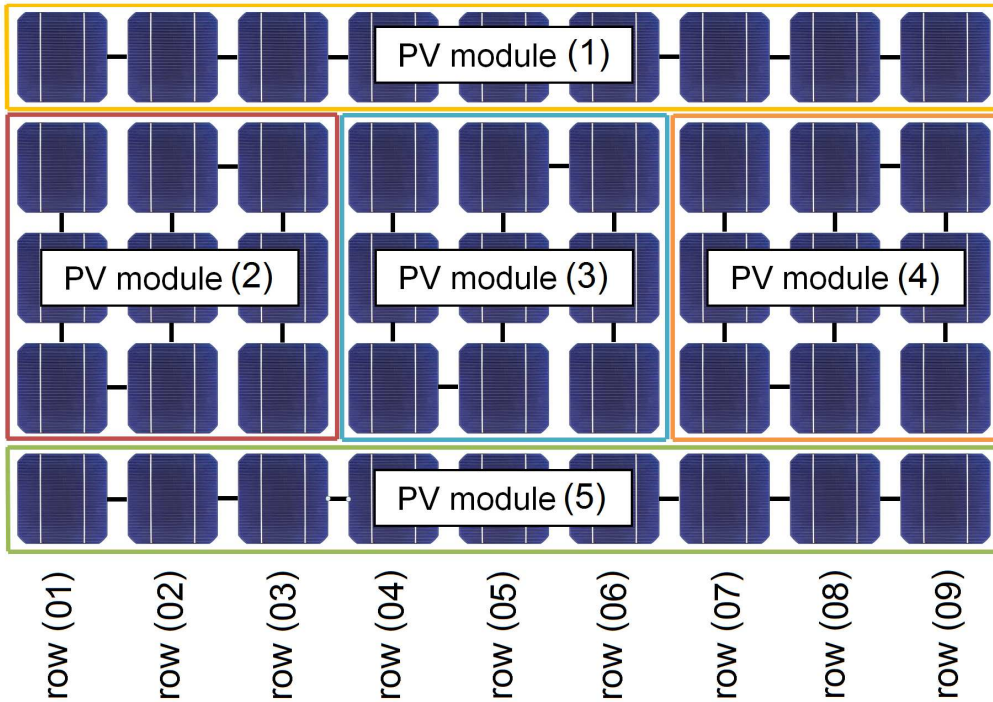


Figure 39: Alignment of PV modules on the roof of the experimental vehicle

Table 29 presents the measurement results of the theoretical output power at a solar altitude angle (α) of 40° . The presented values are already normalised to obtain ΔP_{th} . As seen in Table 29, the lowest amount of power is obtained from the PV cell in row number (09). In this way, it is expected that less power can be achieved from PV modules which contain PV cells from this row number than from other PV modules which do not include PV cells from row number (09). As obtained from Equation (24), the short-circuit current of the interconnection ($I_{sc,new}$) in PV module (1), (4), and (5), will be determined by the short-circuit current of PV cell in row number (09), which is the lowest current available in these system structures ($I_{sc,min}$).

Table 29: ΔP_{th} at $\alpha = 40^\circ$ for PV cells

row (01)	row (02)	row (03)	row (04)	row (05)	row (06)	row (07)	row (08)	row (09)
100.00 %	96.88 %	92.75 %	84.38 %	81.25 %	78.13 %	73.88 %	67.75 %	63.63 %

Table 30 presents the measurements results which are normalised with respect to the PV module with the highest theoretical output power ($P_{th,max}$). In the experiment, the PV module which contains only PV cells from the number (01), (02), and (03) delivered the best output performance. At a given solar altitude angle of 40° , PV module (2) provided about 16 % more power than PV module (3), and about 31 % more power than PV modules (1), (4), and (5). These circumstances indicate that connecting PV cells with various different orientations towards the sun has a significant impact on output performances.

Table 30: ΔP_{th} at $\alpha = 40^\circ$ for PV modules

PV module (1)	PV module (2)	PV module (3)	PV module (4)	PV module (5)
68.57 %	100.00 %	84.20 %	68.57 %	68.57 %

4.8 Static and Dynamic Environmental Conditions

4.8.1 Test Profiles for MPPT Algorithms

As discussed in Chapter 3, the output power of photovoltaics varies with changes in ambient conditions. In particular the solar radiation level (λ) causes a quick change in the amount of current (I_{sc}) and voltage (V_{oc}) which can be gained from PV cells [55], [56]. The position of the MPP (V_{mpp} and I_{mpp}) moves and thus, the operating voltage (V_{op}) needs to be continuously alternated. Here, MPP trackers ensure operating is as close to the MPP as possible. It is worth noting that there are numerous MPPT strategies available [55]. Due to this variety of algorithms, it is difficult to estimate the impact of fast changing ambient conditions on the performance of a MPP tracker and the difference on the output power which can be gained from photovoltaics, is obtained as follows:

$$\eta_{MPPT} = \frac{\int_0^T P_{out}(t) dt}{\int_0^T P_{mpp}(t) dt} \quad (25)$$

Test profiles were proposed which are helpful when investigating the response time and convergence speed of MPPT techniques [69], [70]. In this work, the alternation rate of solar radiation level (r_λ [$\frac{W}{m^2}/sec$]) is calculated in which r_λ expresses the change in the amount of sunlight during a certain period of time. The proposed test profiles in [69] and [70] differ from each other, for example, in the highest possible rate of change ($r_{\lambda,max}$). $r_{\lambda,max}$ varies between 100 and 200 $\frac{W}{m^2}/sec$. Additionally, beside different values for slow alternation rates of solar radiation levels ($r_{\lambda,min}$), test protocols can also include steady-state conditions [69]. Test profiles simulate environmental conditions of a partly cloudy, partly sunny day and the conditions such as partly cloudy, partly sunny days where the conditions are continuously changing, causing the MPP tracker to continuously alternate the operating voltage (V_{op}).

$$\begin{aligned} r_\lambda &= \left. \frac{d\lambda}{dt} \right|_{\lambda_1}^{\lambda_2} & \text{whereas } \lambda_2 > \lambda_1 & \text{for upward ramps} \\ r_\lambda &= \left. \frac{d\lambda}{dt} \right|_{\lambda_1}^{\lambda_2} & \text{whereas } \lambda_2 < \lambda_1 & \text{for downward ramps} \end{aligned} \quad (26)$$

Figure 40 illustrates one test profile that current exists in literature [70]. After an initial settling time, a sequence of upward and downward ramps begins which is continued n times. If the maximum solar radiation level (λ_{max} [W/m^2]) is reached after the time for the upward ramp (t_{up} [s]), the solar radiation level is lowered for the time of the downward ramp (t_{down} [s]) until the initial value (λ_{init} [W/m^2] = λ_{min} [W/m^2]) is obtained again. In [70], no steady-state conditions are considered.

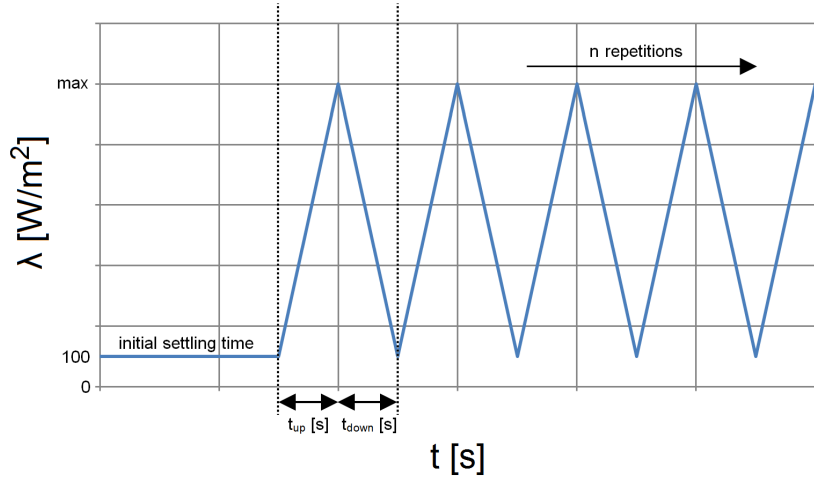


Figure 40: MPPT test profile 1, sequence with n repetitions

Figure 41 shows a test sequence in which steady-state conditions are considered. Here, the solar radiation level does not alternate strictly between a minimum and maximum. Instead, a test pattern is proposed in which slow and fast ramps are used to verify the performance of MPPT algorithms. The test pattern is specified in detail in [69]. The specification includes accurate time periods, for example between upward/downward ramps and steady-state conditions. The most important parameters of the test profile are as follows:

$$\begin{aligned} \lambda_{min} &= 200 \text{ W/m}^2 \\ \lambda_{max} &= 1000 \text{ W/m}^2 \\ r_{\lambda} &= 10 \frac{\text{W/m}^2}{\text{sec}} \quad \text{for the slow upward/downward ramp} \\ r_{\lambda} &= 200 \frac{\text{W/m}^2}{\text{sec}} \quad \text{for the fast upward/downward ramp} \end{aligned}$$

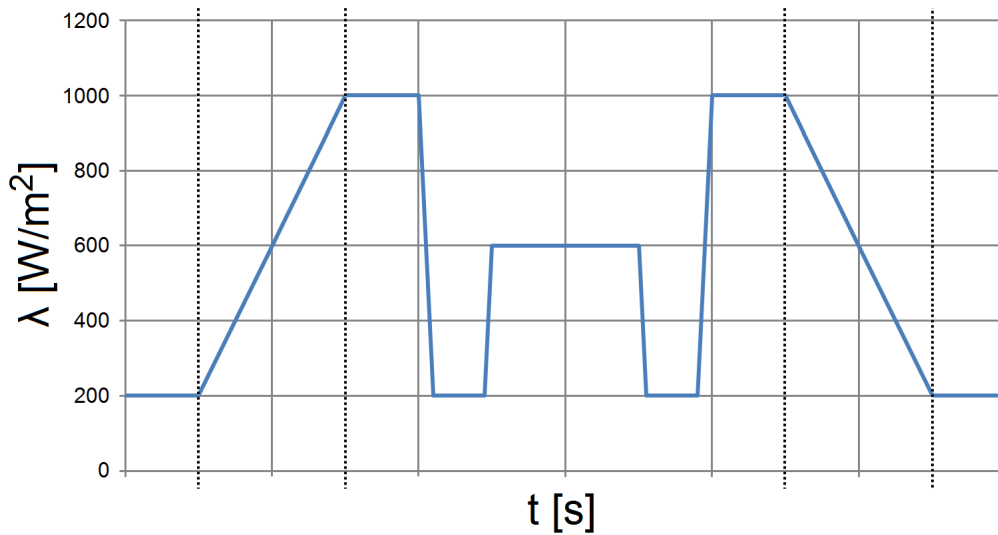


Figure 41: MPPT test profile 2, static and dynamic sections

4.8.2 Static Environmental Conditions

Here, the two considered test profiles in this work are discussed. At first, the focus lies on static environmental conditions in which the location of photovoltaics is fixed. Figure 42 shows an example of a typical partly sunny, partly cloudy day in July. Ambient data on the solar radiation level was collected in the City of Oulu, Finland. In particular during the afternoon, after 13:00, clouds frequently blocked sunlight and thus, the diffuse illumination was measured. The sampling rate of Figure 42 was 10 samples/sec. This sampling rate allowed suitable high resolution of data to be obtained.

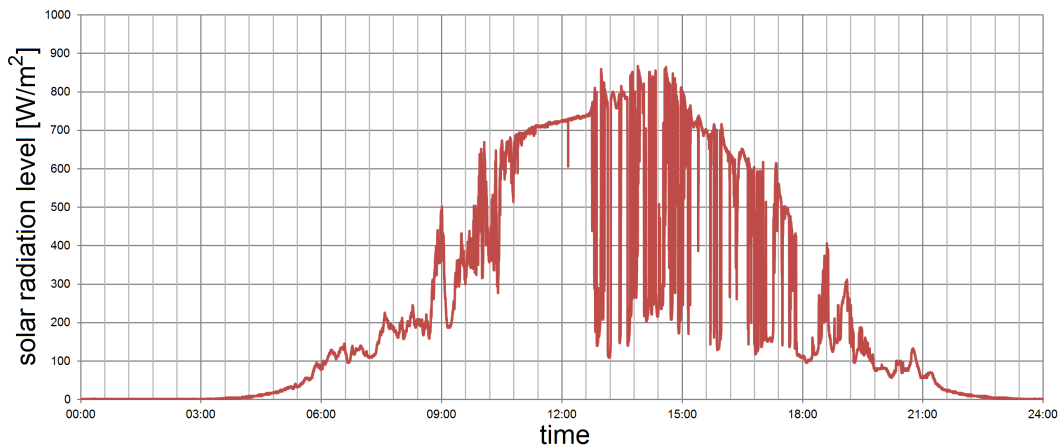


Figure 42: Static environmental conditions, full day example

In particular, during fast changing ambient conditions, such as on a partly sunny, partly cloudy day, with the aid of a MPP tracker a notable amount of power is still achieved from photovoltaics. Figure 43 looks more closely at one particular time period of the previously discussed day in July. The time frame is 4000 sec long and represents the time at around 13:00 to 14:00; in other words, when the ambient conditions change. After 14:00, longer periods of time with direct sunlight was obtained. As seen in Figure 43, steady-state conditions are unusual; the solar radiation level does not fall to an amount of $3/5$ of the maximum solar radiation level (λ_{\max}) and remains there for several seconds. Instead, the solar radiation level alternates between the current minimum and maximum. Even at λ_{\min} or λ_{\max} , the amount of sunlight is not 100 % constant, changes are possible, but are slowly in the rate of a few W/m^2 per second. In Figure 43, $r_{\lambda, \max}$ was as large as $253 \frac{\text{W}}{\text{m}^2}/\text{sec}$.

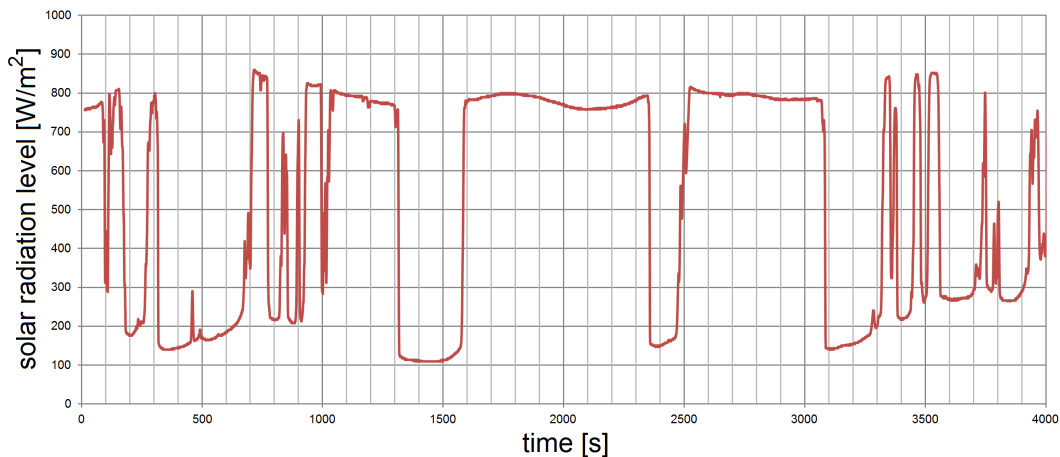


Figure 43: Static environmental conditions, part of a day example

4.8.3 Optical Sensor Unit

In [1], a sensor system was proposed which is capable to identify the amount of shading on top of BEVs and HEVs. The main sensor was a light-to-voltage converter and was used to make a decision between shadow (logical 0) and sunlight (logical 1). This type of detection requires a calibration of the threshold value which is similar to λ_{min} . However, as seen in Figure 42, λ_{min} varies between 100 and 200 W/m² and is not constant throughout the day. As a result, once the optical sensor unit is calibrated, after a few hours another calibration could be required to ensure the correctness of the measurements. Figure 44 illustrates the full measurement setup to obtain data from the optical sensor unit [1].

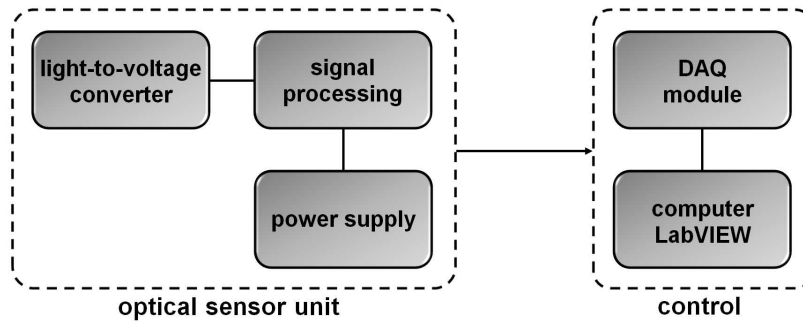


Figure 44: Block diagram of the optical sensor unit

The signal is not directly evaluated by the optical sensor unit. The output signal is measured by a data acquisition (DAQ) module which is connected to a computer with the LabVIEW™ program. Light-to-voltage converters are effective to measure the light intensity in the visible range of the human eye. Figure 45 illustrates the global sunlight spectrum and the visible light spectrum. Additionally, the spectral sensitivity of monocrystalline silicon (mono-Si) and amorphous silicon (a-Si) is shown. It can be seen that light-to-voltage converters do not cover the whole sunlight spectrum. A basic distinction between sunlight and shadow is possible; however, a more precise estimation is difficult with these types of sensors.

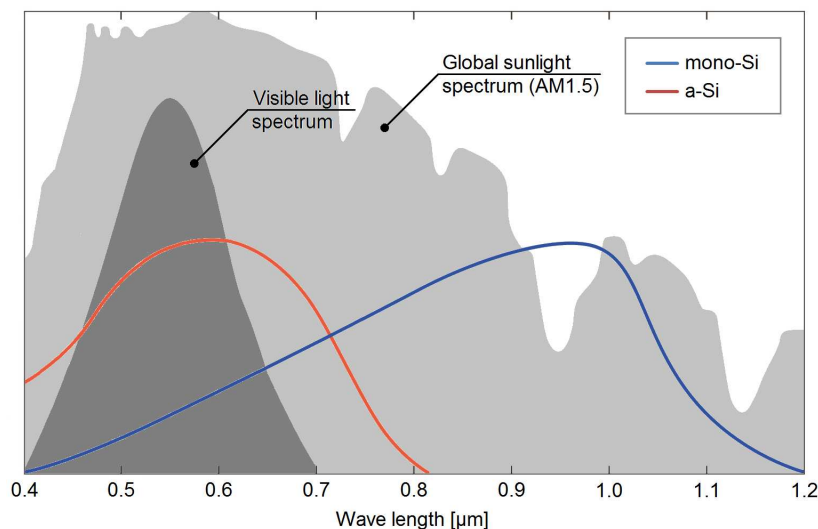


Figure 45: Spectrums of light sources and spectral sensitivity of photovoltaics

4.8.4 Dynamic Environmental Conditions

In [1], two optical sensor units (sensor 1 and sensor 2, respectively) were deployed on the roof of a vehicle to measure the amount of shading in urban and residential areas. The amount of output power of a PV installation on the roof of BEVs and HEVs is expected to change more frequently in driving conditions than when parked. These ambient conditions are considered as dynamic environmental conditions, since the location of photovoltaics is no longer fixed and is moving with the car. Here, the speed of the vehicle will have an impact on the alternation rate r_λ . However, there are several factors for the presence of shadows on roads which have to be taken into account and which have an influence on the result, such as:

- driving direction
- speed of the vehicle
- size of the vehicle
- time of the day
- time of the year
- geographical location
- traffic conditions
- weather conditions

As mentioned before, it is crucial to achieve a suitable high accuracy of the data. Therefore, in this work, an improved optical sensor unit was built which is referred as an environmental monitoring unit. The proposed and fully tested measurement platform offers several advantages to the measurement architecture from [1]. At first, the sampling rate of 2 samples/sec was increased to 20 samples/sec in the environmental monitoring unit. Secondly, four instead of two sensors were placed on top of a vehicle: two at the front (one in the left corner, one in the right corner) and two at the rear of the car (one also in the left corner, one in the right corner). The speed of the vehicle was varied between 25 km/h up to 60 km/h.

Instead of a light-to-voltage converter, a PV cell was used as the main sensor; referred as solar radiation sensor. One of the advantages of the use of a PV cell is that the short-circuit current (I_{sc}) of the cell is directly proportional to the amount of sunlight (λ). The spectral sensitivity of the PV cell corresponds to the sunlight spectrum. Hence, a clear statement on the actual solar radiation level can be made. Another advantage is that the PV cell can be used as an active sensor which means that an additional power supply is not required. Similarly, an individual reference voltage to evaluate the sensor information is not needed. Finally, the expensive DAQ module and the required computer were replaced by a microcontroller with the opportunity for data logging in real time. As a result, the environmental monitoring unit can be installed as an embedded system due to its simplified hardware. Figure 46 illustrates the system architecture of the designed measurement platform.

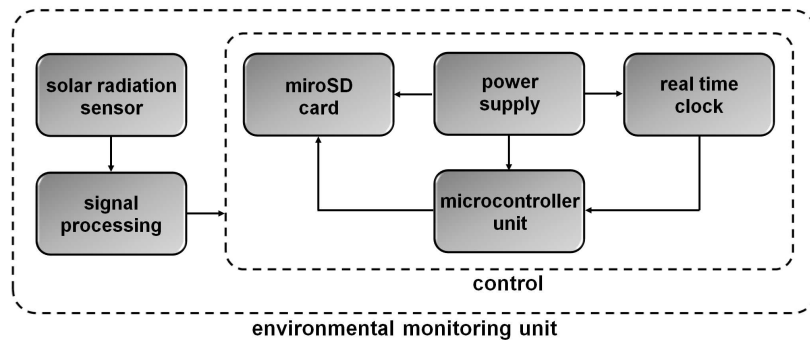


Figure 46: Block diagram of the environmental monitoring unit

It is worth noting that one solar radiation sensor only requires a single analog input of the microcontroller unit. Thus, all four sensors can be connected to a single MCU. These circumstances significantly simplify the hardware requirement. However, it is also possible to establish a large sensor network, for example, a WSN to measure the different amount of sunlight on the whole roof. In particular, long term measurements can be helpful to obtain statistical data over a longer period of time. The focus of this work is to identify suitable values for r_λ in dynamic environmental conditions. Thus, four sensors represent a suitable amount of sensors to evaluate the possible range of r_λ at different vehicle speeds.

Figure 47 illustrates an example of typical shading from trees in streets. The picture was taken in the City of Oulu, Finland around noon when the sky was clear. As mentioned above, in general, ambient conditions depend on various factors and even in the same geographical location, the environmental conditions can differ from street to street at the same time due to different surrounding objects next to the road. The amount of sunlight varies along the road which is shown in Figure 47. In the beginning, the roof of the vehicle is exposed to direct sunlight, but becomes partly shaded repeatedly as the car moves down the street.



Figure 47: Typical shading in a street in urban and residential areas

In the example street which is shown in Figure 47, two measurements were carried out. At first, the vehicle with four sensors was driving on the left-hand side in which more parts of the street are shaded at a speed of 25 km/h (measurement 1). Afterwards, the vehicle was driving on the right-hand side in which more sunlight is available at a speed of 30 km/h (measurement 2). Figure 48 shows the results of the first measurement during a time period of 50 seconds in which data from the four sensors was collected.

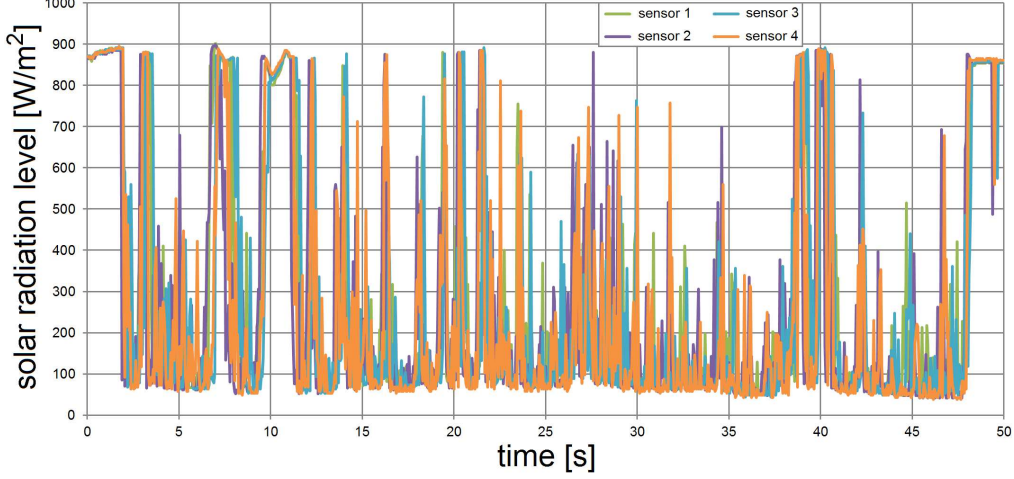


Figure 48: Dynamical environmental conditions, measurement 1

It can be seen that at the beginning and at the end of the measurement, all four sensors were in the sun and measured similar values on the amount of sunlight. However, it is difficult to state whether all four sensors have obtained a similar amount of sunlight throughout the measurement in the example street. Therefore, a statistical analysis was carried out which reveals that the mean value of the solar radiation level on each sensor ($\lambda_{sensor1}$ [W/m²], $\lambda_{sensor2}$ [W/m²], $\lambda_{sensor3}$ [W/m²], $\lambda_{sensor4}$ [W/m²]) was similar. $r_{\lambda,max}$ was as large as 812 W/m² in only 50 ms.

$$\lambda_{sensor1} = 295 \pm 274 \text{ W/m}^2$$

$$\lambda_{sensor2} = 290 \pm 267 \text{ W/m}^2$$

$$\lambda_{sensor3} = 297 \pm 271 \text{ W/m}^2$$

$$\lambda_{sensor4} = 293 \pm 263 \text{ W/m}^2$$

$$r_{\lambda,max} = 812 \text{ W/m}^2 \text{ in } 50 \text{ ms} \quad \text{for the fastest ramp}$$

Measurement 2 was carried out in the other direction of the example street which is shown in Figure 47. On the right-hand side of the street, the speed of the vehicle was higher and more sun was available. The time period of the measurement was 45 seconds and data was again collected from all four sensors. Figure 49 illustrates the measurement results. In measurement 2, more often and for a longer period of time the sensors measured direct sunlight compared to measurement 1. Taking a look on Figure 47 again, it can be seen that the shadow of trees does not cover the complete lane on the right-hand side. The distance from one sensor of the environmental monitoring unit to one other is about one metre.

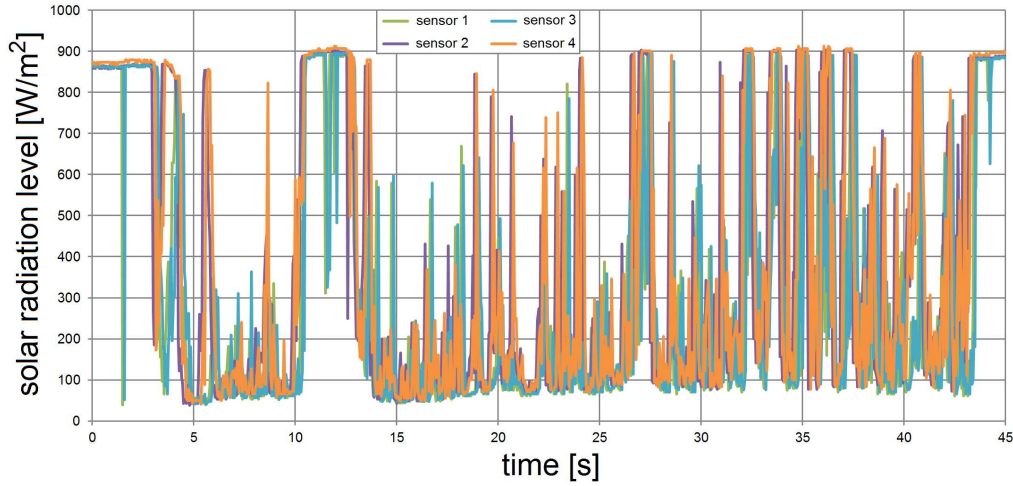


Figure 49: Dynamical environmental conditions, measurement 2

In the statistical analysis, $\lambda_{sensor1}$ and $\lambda_{sensor3}$ in measurement 2 are similar to the results in measurement 1. Both sensors are located on the left-hand side of the vehicle. However, $\lambda_{sensor2}$ and $\lambda_{sensor4}$ measured about 20 % more sunlight compared to $\lambda_{sensor1}$ and $\lambda_{sensor3}$. These results indicate that the roof of the vehicle is not evenly shaded and PV modules on the right-hand side can produce more power than PV modules on the left-hand side of the car. $r_{\lambda,max}$ was as large as 826 W/m^2 in only 50 ms.

$$\lambda_{sensor1} = 307 \pm 306 \text{ W/m}^2$$

$$\lambda_{sensor2} = 376 \pm 330 \text{ W/m}^2$$

$$\lambda_{sensor3} = 311 \pm 306 \text{ W/m}^2$$

$$\lambda_{sensor4} = 383 \pm 332 \text{ W/m}^2$$

$$r_{\lambda,max} = 826 \text{ W/m}^2 \text{ in } 50 \text{ ms} \quad \text{for the fastest ramp}$$

Shading of trees is not uniform and more or less shadow can appear on the road depending on the type of tree and the distance between trees. Figure 50 illustrates an example for a highway bridge in the City of Oulu, Finland. Under the bridge, no sunlight is available and therefore no diffuse illumination will be obtained. A measurement was carried out to evaluate the effect of shading from this type of solid object. In Figure 50, it can be seen that the two lanes of the highway are separated by a few metres from each other, which means during a short period of time, sunlight will be obtained before the roof of the vehicle falls again into shadow for a few more seconds.



Figure 50: Typical shading under a highway bridge

Figure 51 presents the measurement results in which the speed of the vehicle was 60 km/h (measurement 3). Sensor 1 and sensor 2 do not fall exactly at the same time into shadow, because the vehicle and the shadow of the bridge were not completely at a rectangular angle with each other. It is worth noting that the speed of the car was 16.67 m/s and the distance of one sensor to one other of one metre is rather small. If a longer vehicle, for example, a bus would drive under the bridge the difference would become more clear. However, in Figure 51, a small difference between $\lambda_{sensor1}$, $\lambda_{sensor2}$, $\lambda_{sensor3}$, and $\lambda_{sensor4}$ can be seen.

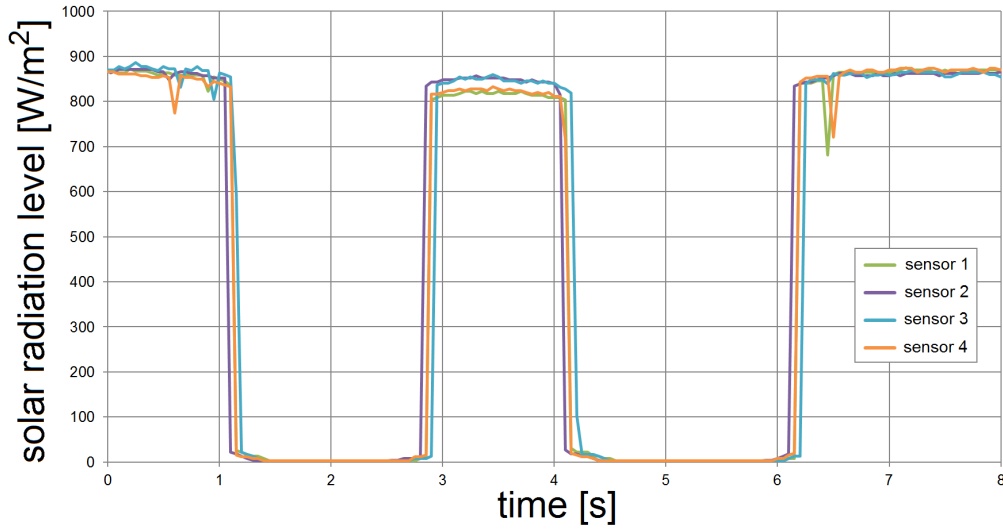


Figure 51: Dynamical environmental conditions, measurement 3

$$\lambda_{sensor1} = 420 \pm 447 W/m^2$$

$$\lambda_{sensor2} = 425 \pm 452 W/m^2$$

$$\lambda_{sensor3} = 424 \pm 451 W/m^2$$

$$\lambda_{sensor4} = 420 \pm 446 W/m^2$$

$$r_{\lambda,max} = 833 W/m^2 \text{ in } 50 ms \text{ for the fastest ramp}$$

4.8.5 Comparison between Static and Dynamic Environmental Conditions

The rates of change in ambient conditions in test profiles 1 and 2, respectively, are suitable high enough to cover real situations in static environmental conditions. The highest value for $r_{\lambda,max}$ was as large as $253 \frac{W}{m^2}/sec$ and about $50 \frac{W}{m^2}/sec$ higher than in the investigated test profile from [69] and about $100 \frac{W}{m^2}/sec$ higher than in the considered test profile from [70]. However, in general, the proposed alteration rate in [69] is appropriate to verify the response time of MPPT algorithms. The steady-state conditions at around $3/5$ of the current maximum solar radiation level λ_{max} are rather uncommon, as seen in Figure 42 and Figure 43. Commonly, on partly sunny, partly cloudy days, the amount of sunlight alternates between the minimum (diffuse illumination) and the maximum (direct sunlight).

In dynamic environmental conditions, the amount of sunlight changes more frequently. Instead of a time window of one second, the alteration rate r_{λ} is obtained in 50 ms. In this shorter time frame, the rate of change is four times higher under dynamic than under static environmental conditions. The speed of the vehicle has an impact on r_{λ} , however, as soon as the vehicle is driving, for example 25 km/h, the amount of sunlight of each PV cell can change quickly. Even at a day with clear sky, shading will be caused by many surrounding objects such as trees and buildings. Here, a test profile for MPPT algorithms could have a similar shape to the situation when a vehicle drives under a bridge, as seen in Figure 51.

4.9 Monitoring System for Photovoltaics

4.9.1 Purpose and Development of the Monitoring System

Even though the space for installing photovoltaics on top of BEVs and HEVs is limited, the ambient conditions can vary a lot throughout the available area of about 1.5 to 2 m². The height of vehicles is lower than buildings and thus, the PV installation can be partly shaded easier than PV modules on the roof of houses. For example in parking areas, surrounding objects such as trees and lamp posts can cause shadows on a single or a few PV cells of interconnections. As discussed above, in a series connection of PV cells, the output current depends on the performance of the weakest PV cell in the system structure [5], [8].

Environmental conditions also change during the day. For example, if a car is parked in the sun in the morning, during the day shadows can occur and reduce the amount of produced solar energy. Therefore, one of the main purposes of the monitoring system is to characterise possible scenarios which can cause shading on the roof of vehicles. An opportunity is to categorise and group possible ways shadows can occur on the top of the vehicle. This information is helpful for the alignment of photovoltaics and establishing system structures [8].

BEVs and HEVs represent a new environment for photovoltaics. In particular, the impacts on the output behaviour of photovoltaics caused by driving in urban and residential areas are different than those in parking conditions. The collection of environmental data is valuable, for example to verify the performance of MPPT algorithms [5]. In this work, the progress in the development of this measurement system is elaborated. At first, the first generation of monitoring systems is discussed; followed by the second generation of system.

The goal of the proposed monitoring system is to collect data on the amount of sunlight next to PV cells in different system structures, without disconnecting PV cells from the interconnection to obtain this type of information. Therefore, the system is divided into several units which measure the amount of sunlight individually. The obtained solar radiation level of these units is helpful for the estimation of the amount of solar energy which can be produced by the PV installation during the day and is useful to make a prediction on the percentage, for example, on how much the high-voltage battery can be charged.

Another valuable piece of information provided by the monitoring system is the benefit of disconnecting shaded PV cells from non-shaded PV cells. Currently, the short-circuit current (I_{sc}) of the system structure drops to the current level of the shaded PV cells. In the worst case scenario, one shaded PV cell reduces the performance of the eight other PV cells. In this situation, the output power is improved if the shaded PV cells are disconnected from the interconnection. This can be an opportunity to improve the output performance when unfavourable environmental conditions occur with an increased amount of hardware.

4.9.2 First Generation of the Monitoring System

Figure 52 shows the components of the proposed measurement system. Here, the architecture includes one main unit and three subunits. The sensor which is used to obtain the amount of sunlight is the same one as in the optical sensor unit. The signal quality is improved before data is transmitted over the LIN-bus to the main unit. The main unit also measures as the subunits the amount of sunlight with a light-to-voltage converter. A microcontroller unit in the main unit evaluates the four measurement results and based on a threshold value, a decision is made between shadow and sunlight. In [5], the differentiation is the opposite than the one in Chapter 4.8.3, sunlight is considered as logical 0 (referred as the situation that no changes in the environmental conditions detected) and shadow as logical 1 (to indicate that a change in ambient conditions has occurred and that a response of the system is required) [5].

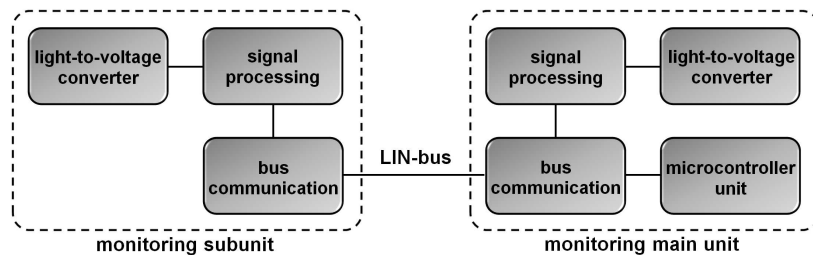


Figure 52: Components of the monitoring system, first generation

At the beginning of this research, one system structure contained six PV cells. As mentioned before, this amount was increased to meet the requirements on the input voltage (V_{in}) for the dc/dc converter. However, it was possible to evaluate the performance of the monitoring system with an interconnection of six PV cells. Figure 53 shows an experimental setup in which one monitoring subunit is located on the left-hand side while the main unit is placed on the other side of the structure [5]. If shadow appears from the left-hand side as illustrated in Figure 53, the monitoring subunit detects shadows and PV cell in row number (01) is disconnected.

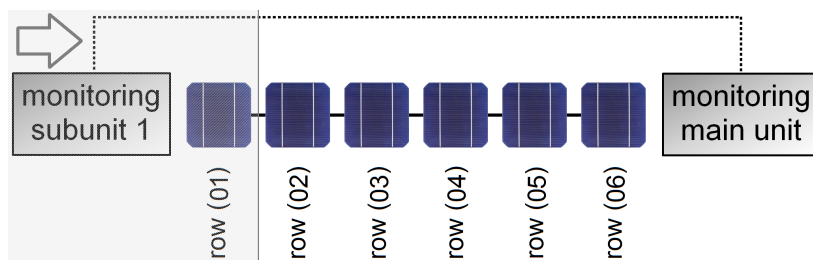


Figure 53: Experimental system structure of six PV cells

Table 31 summarises possible scenarios for the disconnection of shaded PV cells from non-shaded PV cells based on the sensor information of the monitoring units. As seen in Table 31, if either the PV cells in row number (01) or (06) fall into shadow, they are immediately disconnected. In the case shadow appears from the right-hand side, a measurement is triggered to obtain the voltage from the PV cell in row number (05). If the voltage is low, the PV cell is disconnected as well. If shadow on the left- and right-hand side is detected with the help of the monitoring subunit and main unit, the PV cells in row number (01) and (06) are disconnected from the interconnection [5].

Table 31: Disconnection logic for the experimental system structure of six PV cells

monitoring subunit	monitoring main unit	PV cell row number					
		(01)	(02)	(03)	(04)	(05)	(06)
0	0	c	c	c	c	c	c
0	1	c	c	c	c	a/d	d
1	0	d	a/d	c	c	c	c
1	1	d	c	c	c	c	d

0 ... sunlight obtained

1 ... shadow detected

c ... PV cell connected

d ... PV cell disconnected

a/d ... analog-to-digital conversion

Figure 54 illustrates the complete structure of the monitoring system. In each corner, either a monitoring subunit or the monitoring main unit is placed so that possible shading of PV cells can be detected. Here, the proposed system can function as a trigger to indicate possible mismatches in the amount of sunlight in system structures. The truth-table for the whole monitoring system is larger than the one shown in Table 31 [5]. In Figure 54, the switch boxes S represent the opportunity for different possible configurations which can be established in a test environment which is similar to the one shown in Chapter 4.7.3 and in Figure 38.

Measurement results which are presented in [5] indicate the possible increase in the amount of power in the MPP (P_{mpp}), in the case shaded PV cells are disconnected from non-shaded PV cells. If two PV cells fall into shadow, the gain in the amount of output power is significant. The presented values in [5] are for the experimental structure which is shown in Figure 53, in which six PV cells are connected with other. However, it is worth noting that an additional amount of hardware is required to enable the disconnection of individual PV cells.

In the first generation of the monitoring unit, the disconnection of up to two PV cells was considered allowing the remaining four PV cells to produce the required input voltage (V_{in}) for the dc/dc converter in the old specifications [5]. The proposed monitoring system can also be used for nine PV cells in which the PV cells in row number (02) and (03) are measured if shadow appears from the left-hand side (shadow detected on PV cell in row number (01)), and the PV cells in row number (07) and (08) are measured in the scenario of shadow from the right-hand side (shadow detected on PV cell in row number (09)).

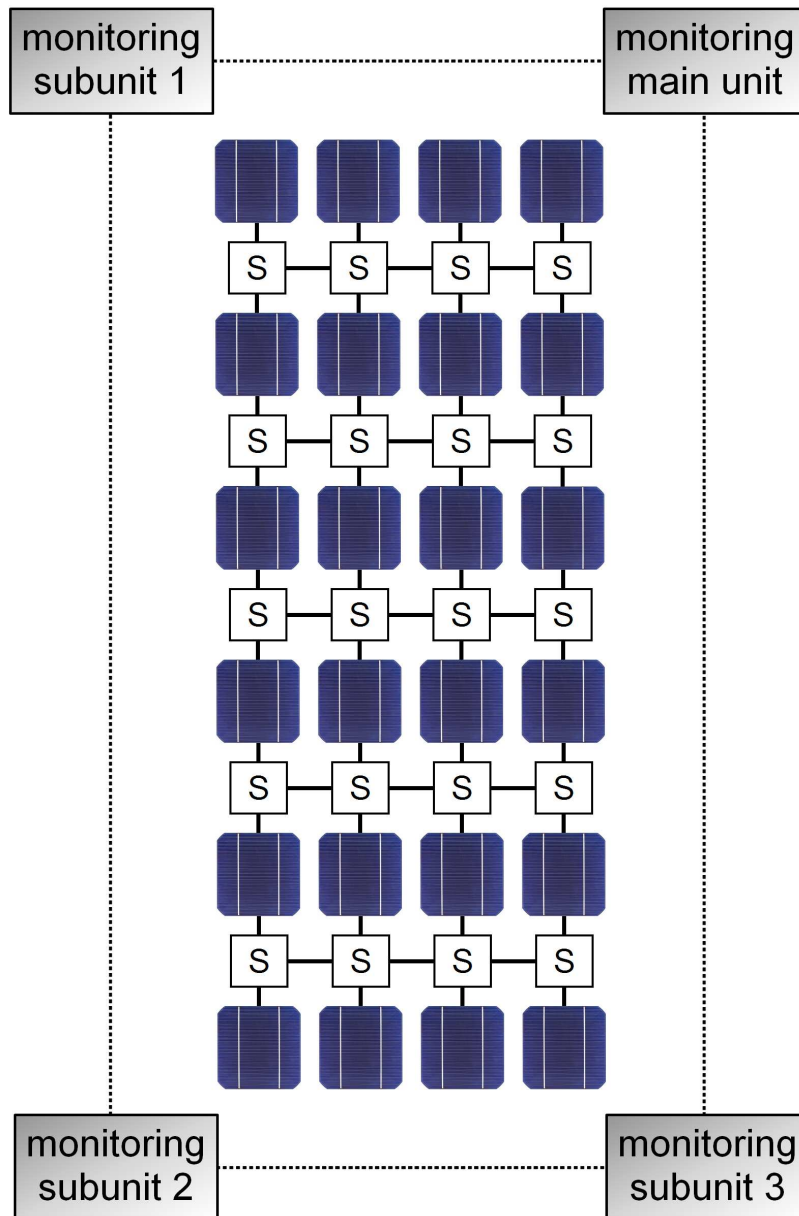


Figure 54: Complete structure of the monitoring system, first generation

4.9.3 Second Generation of the Monitoring System

For the second generation of the monitoring system, the light-to-voltage converter was replaced by a solar radiation sensor, the same one used in the environmental monitoring unit. Here, the goal is also to obtain more precise information about the current ambient conditions. Instead of a differentiation in two values, logical 0 and 1, the monitoring system measures the exact amount of illuminated PV cells which is currently obtained in the different row numbers. Figure 55 illustrates the components of the second generation of the monitoring system. It is worth noting that every unit is now similar to other ones and there is no classification of a main and several subunits as before. As seen in Figure 55, in each unit a MCU is present [8].

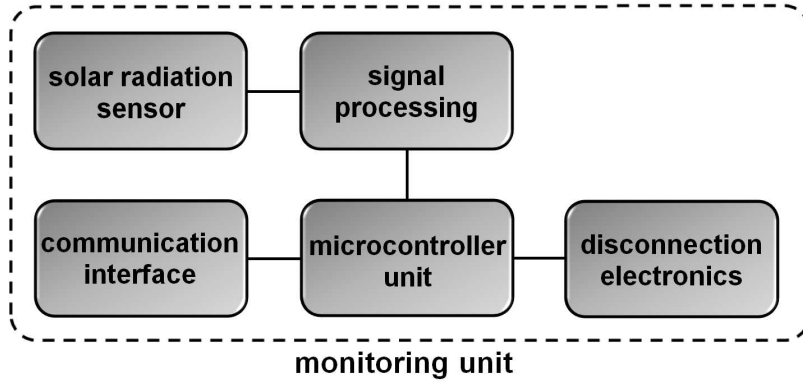


Figure 55: Complete structure of the monitoring system, second generation

Figure 56 and Figure 57 illustrate the monitoring system for the two system structures, 9×1 and 3×3 (in $n_{cells,l} \times n_{cells,w}$). Instead of two corner-orientated monitoring units, in the second generation of the system, monitoring units are located close to the PV cells which can be disconnected. Moreover, the second PV cell in the chain is no longer measured in case the first PV cell falls into shadow. In this way, the monitoring unit which obtains the same amount of sunlight as the PV cell next to them act as the trigger for disconnecting shaded PV cells from the interconnection. In the case of the system structure 9×1 (in $n_{cells,l} \times n_{cells,w}$), the solar radiation level is measured in PV cell row number (01), (02), (03), (07), (08), and (09). Hence, the opportunity is given to react to shading either from the left- or right-hand side. Up to three out of nine PV cells can be disconnected [8].

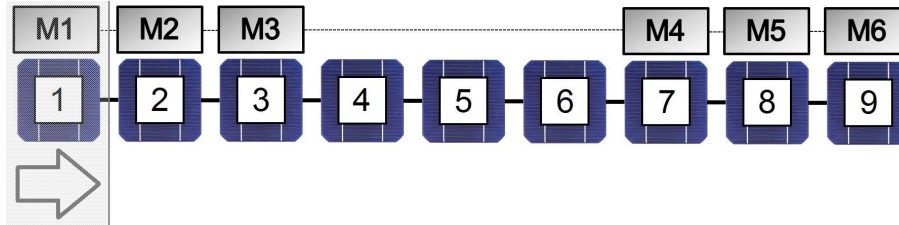


Figure 56: System structure 9×1 (in $n_{cells,l} \times n_{cells,w}$)

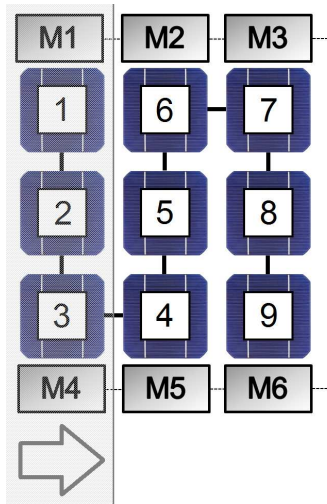


Figure 57: System structure 3 x 3 (in $n_{cells,l} \times n_{cells,w}$)

As mentioned before, on the roof of vehicles, shadow is likely to appear from the left- and right-side. As a result, PV cells in rows number (01) or (09) will be the first to fall into shadow. PV cells on top of cars can also be partly shaded, for example, by small objects such as trees and lamp posts. This means that any PV cell of the interconnection can be shaded at any time. Figure 58 and Figure 59 show an improved version of the proposed monitoring system which can also react to partial shading of any individual PV cell.

Instead of using nine monitoring units, more sensors are connected to the same monitoring unit at the same time. One monitoring unit has three distributed sensors which are sensed simultaneously. In the system structure 9 x 1 (in $n_{cells,l} \times n_{cells,w}$), monitoring unit 1 measures the amount of sunlight in PV cell row number (01), (02) and (03), while monitoring unit 2 obtains the solar radiation level in PV cell row number (04), (05), and (06) and monitoring unit 3 verifies the ambient conditions in the remaining rows with PV cells.

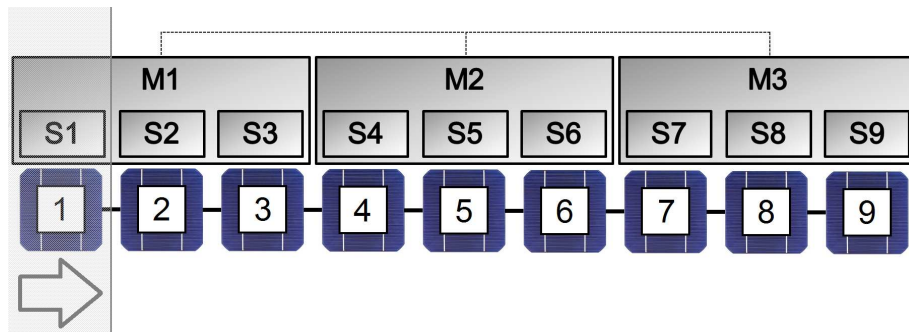


Figure 58: System structure 9 x 1 (in $n_{cells,l} \times n_{cells,w}$), improved version

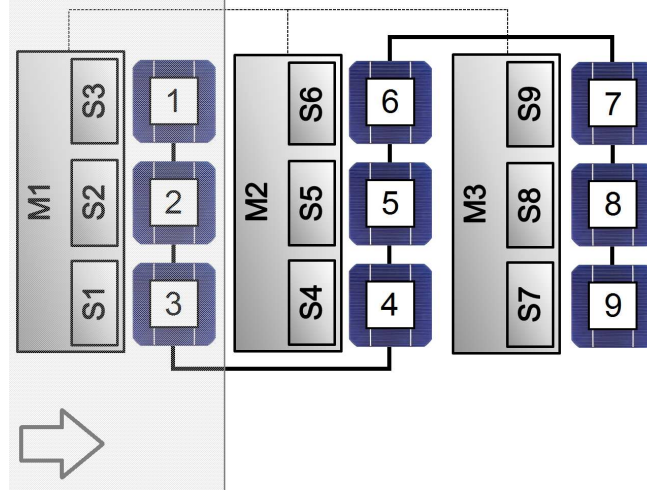


Figure 59: System structure 3 x 3 (in $n_{cells,l} \times n_{cells,w}$), improved version

The proposed monitoring system provides information on the overall illumination of system structures. Additionally, it is helpful to study the potential improvement if shaded PV cells are disconnected from non-shaded PV cells. It is worth noting that the non-linear curved shape of the roof of vehicles has an influence on the amount of sunlight each PV cell obtains in different row numbers [5], [8]. In flat PV modules, which are mounted for example onto the roof of buildings, each PV cell receives the same solar radiation level, expressed as follows:

$$\lambda_{(01)} = \lambda_{(02)} = \dots = \lambda_{(08)} = \lambda_{(09)} \quad (27)$$

However, the calculated normalised effective area ΔA_{eff} of PV module (1) and (5) indicates that each individual PV cell of the system structure obtains a different amount of sunlight. Hence, depending on the solar altitude angle, the PV cell in row number (01) or (09) receives the highest solar radiation level if the sun is not directly above the car at a 90 degree angle. The monitoring units in the different rows with PV cells calculate these differences in the amount of sunlight (ε [%]), as illustrated in Figure 60 [8].

$$\begin{aligned} \lambda_{(01)} > \lambda_{(02)} > \dots > \lambda_{(08)} > \lambda_{(09)} \quad \text{or} \\ \lambda_{(01)} < \lambda_{(02)} < \dots < \lambda_{(08)} < \lambda_{(09)} \end{aligned} \quad (28)$$

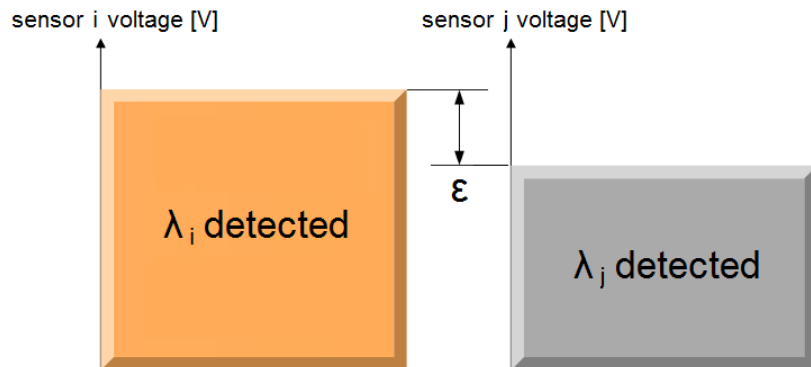


Figure 60: Principle of obtaining variations in the monitoring system

If one PV cells becomes shaded, the short-circuit current (I_{sc}) of the system structure drops to this current level and thus, the theoretical output power of the interconnection ($P_{th,a}$ [W]) is reduced, calculated as follows:

$$\begin{aligned} P_{th,a} &= N \times V_{oc} \times (k \times I_{sc}) \quad \text{whereas } k < 1 \\ I_{sc,min} &= k \times I_{sc} \end{aligned} \quad (29)$$

where N is the amount of PV cells in the interconnection. If the shaded PV cell is disconnected from the system structure, the voltage of this PV cell (V_{oc}) will be lost and theoretical output power ($P_{th,a}$ [W]) will be

$$P_{th,b} = (N - 1) \times V_{oc} \times I_{sc} \quad (30)$$

In this way, it is of interest to calculate the threshold or at which point it becomes beneficial to disconnect the shaded PV cells from the non-shaded PV cells, obtained as follows:

$$k < \frac{(N - 1)}{N} \quad (31)$$

Here, the difference in the amount of theoretical output power is calculated as a variation in output performance (ε_{shadow} [%]) between the situation when all PV cells are exposed to direct sunlight ($P_{th,sun}$ [W]) and one or more PV cells fall into shadow ($P_{th,shadow}$ [W]). The results are compared to the theoretical output power of system structures with disconnected, shaded PV cells ($P_{th,modified}$ [W]) to obtain again variations in output performances ($\varepsilon_{modified}$ [%]). Table 32 summarises the differences in case one or two PV cells are shaded. It can be seen that the increase in theoretical output is significant which can be achieved with additional hardware effort as the proposed monitoring system.

$$\varepsilon_{shadow} = \frac{P_{th,shadow}}{\frac{P_{th,sun}}{100}} \quad (32)$$

$$\varepsilon_{modified} = \frac{P_{th,modified}}{\frac{P_{th,sun}}{100}} \quad (33)$$

Table 32: Shadow in the system structure 9 x 1 (in $n_{cells,l} \times n_{cells,w}$)

shadow in row number	ε_{shadow}	$\varepsilon_{modified}$
(01)	15.92 %	89.06 %
(01), (02)	15.11 %	77.92 %
(09)	11.55 %	94.91 %
(08), (09)	14.55 %	90.59 %

5 Discussion

5.1 Summary of the Results and Contribution of the Doctoral Thesis

At the moment, research on PV installations on the top of BEVs and HEVs is still in its infancy. Since 2010 (the start of this thesis), more and more papers have been published on this research topic. In [1], an investigation on the amount of solar energy which can be produced on the roof of a vehicle was presented. In this work, more details were provided which indicate that the results presented in [1] are relatively optimistic.

- At first, the amount of PV cells was calculated for BEVs and HEVs which are currently available on the market. Analyses reveal that the amount of photovoltaics varies between different vehicles from the same and different manufacturers. Furthermore, the shape of the roof of current BEVs and HEVs was discussed. Here, the longitudinal angles of PV cells were given which indicate that each PV cell in different rows will have a different orientation towards the sun. Sometimes, the variation in longitudinal angles between different rows with PV cells is small; however, often the difference in the orientation is relatively large. These circumstances result in a reduced output performance compared to conventional, flat PV modules which are mounted, for example onto the roof of buildings. It was seen that the non-linear curved shape of the roof is common in today's BEVs and HEVs.
- Secondly, the effective area of photovoltaics was introduced as an indicator of the performance of PV cells on the roof of vehicles. Effective areas were calculated for different solar altitudes. It was shown that the difference in the effective area is larger at low solar altitude angles $[0^\circ, 40^\circ]$ and $[140^\circ, 180^\circ]$ and becomes smaller when the sun is more directly above the car $[40^\circ, 140^\circ]$. Using the experimental vehicle, a Toyota Prius, calculations of effective areas of photovoltaics were verified. Output power levels of PV cells were measured under different solar altitude angles and a statistical evaluation of the experiments was presented. It was shown that the calculated, normalised effective area (ΔA_{eff}) corresponds to measured, normalised theoretical output power (ΔP_{th}) in practise. As a result, for any shape of roof on a vehicle, the amount of power can be estimated at any solar altitude angle.
- Next, different types of system structures were presented since the way PV cells are interconnected has an impact on the output performance of the PV installation. Different types of system structures produce different output power levels due to the non-linear curved shape of the vehicles roof. It is worth noting that the alignment of PV cells and series connection has to be carried out carefully. The configuration of system structures depends on the required amount of PV cells in one PV module.
- The difference between static and dynamic environmental conditions was discussed. In static environmental conditions, the location of the PV installation is fixed, in other words, these types of conditions are given when the car is in parked. When driving in urban and residential areas, dynamic environmental conditions are present. It was shown that test profiles for MPPT algorithms are suitable for static, but not for dynamic environmental conditions. Measurement results were presented which show the amount of shading on the roof of a vehicle in different scenarios which can be found in urban and residential areas. Data was collected with an environmental monitoring unit which was designed within this work. The difference in alteration rates r_λ was given however it is suggested that more data for the design of a test profile for dynamic environmental conditions should be collected.

- Finally, a monitoring system was presented which is capable of collecting data on the amount of sunlight without the measurement of PV cells directly. This is particularly helpful when gathering more data in ambient conditions on the top of BEVs and HEVs since it was demonstrated that the output power increases if shaded PV cells are disconnected from non-shaded PV cells. This offers the opportunity to modify the interconnection of PV cells dynamically, in the case unfavourable environmental conditions occur.

5.2 Example Calculation

5.2.1 Background for the Calculation

Here, an example calculation is presented. The goal of this chapter is to link the different chapters of this thesis and to estimate the amount of solar energy which can be produced on top of HEVs and BEVs. The presented calculations are based on the content of the following chapters:

- possible reduction of emissions and fuel consumption (Chapter 1)
- energy demand of HEVs and BEVs (Chapter 2)
- energy storage devices in HEVs and BEVs (Chapter 2)
- output behaviour of photovoltaics (Chapter 3)
- use of a PV simulation model (Chapter 3)
- power of photovoltaics on top of vehicles (Chapter 4)
- impact of the non-linear curved shape of the roof (Chapter 4)
- calculation of the effective area (Chapter 4)
- connection between effective areas and output power levels (Chapter 4)
- impact of system structures (Chapter 4)
- influence of dynamic environmental conditions (Chapter 4)

5.2.2 PV Simulation Model of the Photovoltaics in this Research Work

At first, a PV simulation model was built of the PV cells which were used in this research work. The simplified model was chosen for computing the amount of power in the MPP under different ambient conditions (Chapter 3.2 and Chapter 3.5.4). Therefore, the values for the required parameters were obtained from the data sheet of the PV manufacturer [15]. Beside the values in Table 8, the values for the temperature coefficients (K_I and K_V) were required. The parameter A was assumed as 1.2 which is a typical value for monocrystalline silicon PV cells. The unknown value of the parameter R_s was calculated in such a way so that the simulated I-V curves matched the I-V curves from the data sheet of the PV manufacturer [15]. The influence of R_{sh} was neglected due to the use of the simplified PV model [15]. Figure 61 illustrates the I-V curves which were obtained from the data sheet of the PV manufacturer.

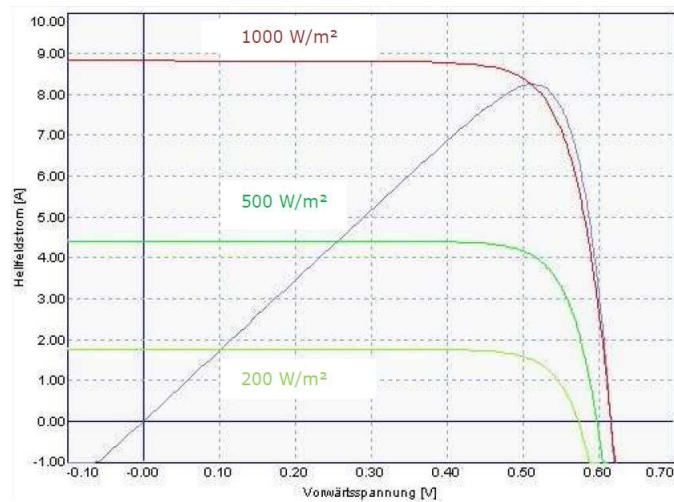


Figure 61: I-V curves from the data sheet of the PV manufacturer

The provided I-V curves were measured at a solar radiation level (λ) of 200, 500, and 1000 W/m^2 and at a PV cell temperature (T_c) of 298 K = 25 °C. Figure 62 illustrates the differences between the simulated I-V curves and obtained I-V curves from the data sheet of the PV manufacturer [15]. It can be seen that the simulation results match reasonably well the provided measurement results from the PV manufacturer.

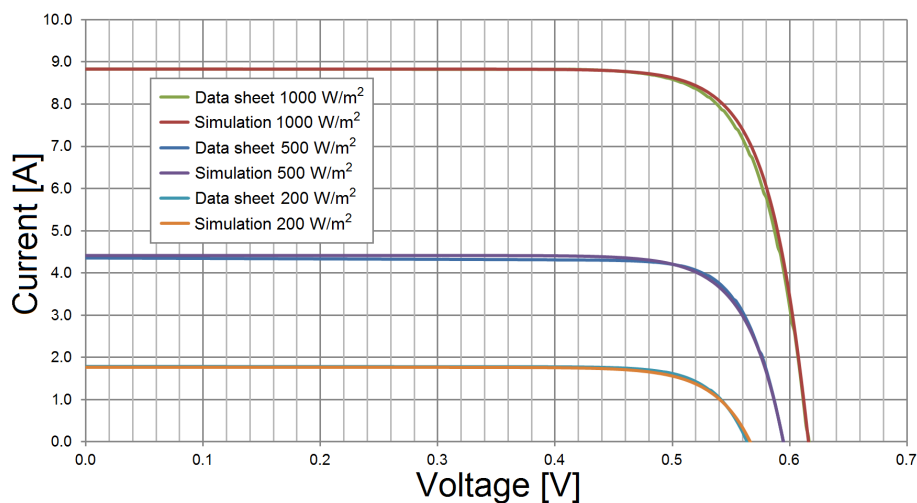


Figure 62: Difference between simulated and obtained I-V curves

As discussed in Chapter 3, there are two parameters (input parameter 1 and input parameter 2, respectively) required for computing the amount of output power of photovoltaics for an entire day. These parameters are the solar radiation level (λ) on the one hand and the PV cell temperature (T_c) on the other. Figure 63 presents the solar radiation level of a partly sunny, partly cloudy day. Data was collected at $\beta = 0^\circ$ in the City of Oulu, Finland in July. Figure 64 shows the PV cell temperature which was obtained during the same day at $\beta = 0^\circ$. The data represents the circumstances for photovoltaics on top of HEVs and BEVs under static environmental conditions (Chapter 4.8.2).

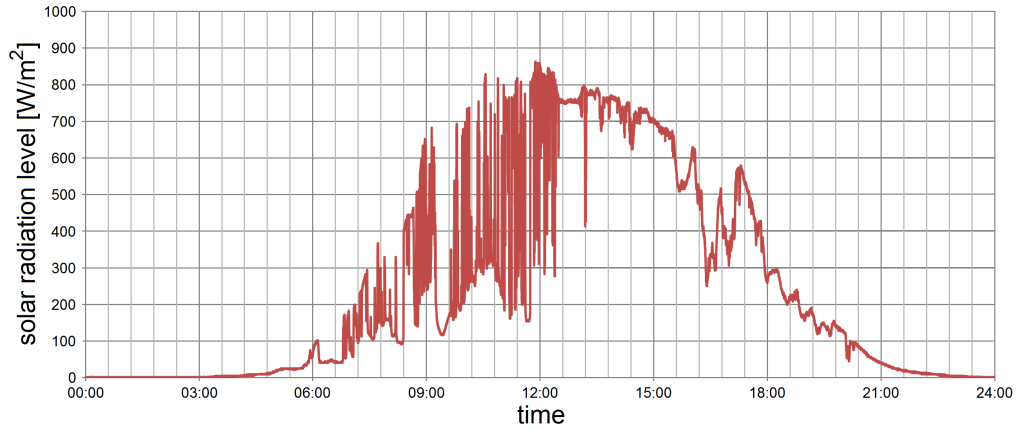


Figure 63: Input parameter 1: Solar radiation level (λ)

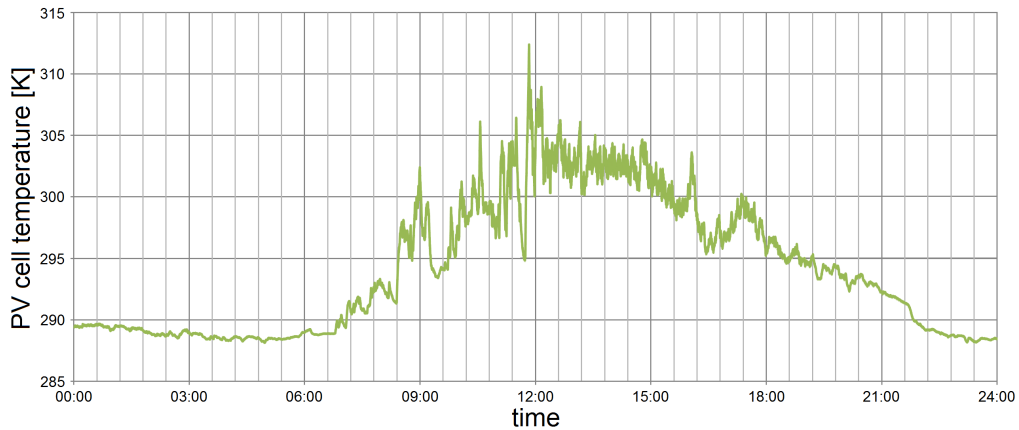


Figure 64: Input parameter 2: PV cell temperature (T_c)

After the verification of all parameters, the output power of one PV cell ($\beta = 0^\circ$) can be computed. Figure 65 presents the output power of one PV cell. The data is for the ideal case in which the operating voltage (V_{op}) was always equal to the voltage in the MPP (V_{mpp}). Hence, Figure 65 shows the maximum amount of power which can be obtained from one PV cell during the whole day under the given ambient conditions.

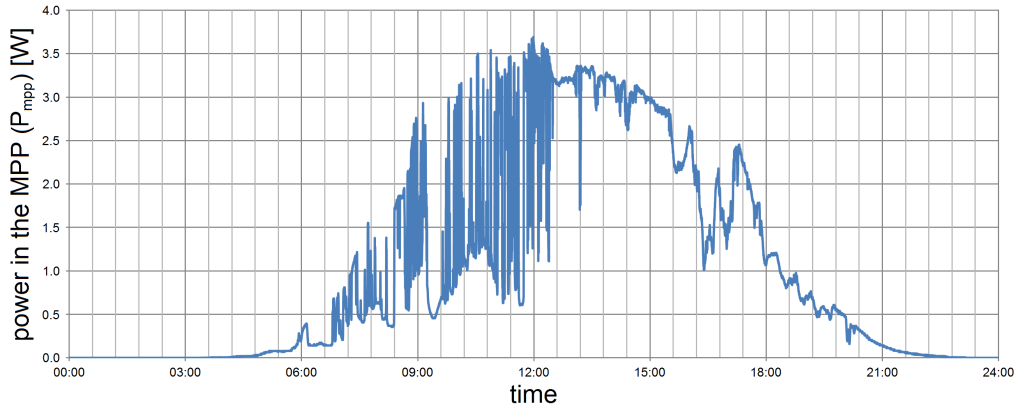


Figure 65: Output power of one PV cell (P_{mpp}), whole day

5.2.3 Estimation of the Output Power of the PV Installation

In Chapter 4.6, effective areas of PV cells (A_{eff}) were calculated for estimating the amount of output power of PV cells in different rows [8]. Non-linear curved shapes such as the roofs of vehicles cause different orientations of individual PV cells towards the sun (Chapter 4.5). As a result, the amount of power from single PV cell differs from one other in different rows. The effective area (A_{eff}) is calculated from Equation (15). Here, this equation is modified for the consideration of the sun azimuth (θ [$^\circ$]) and the cardinal direction of the vehicle's orientation (ψ [$^\circ$]), as follows:

$$A_{eff,new} = \cos(\alpha) \sin(\beta) \cos(\psi - \theta) + \sin(\alpha) \cos(\beta) \quad (34)$$

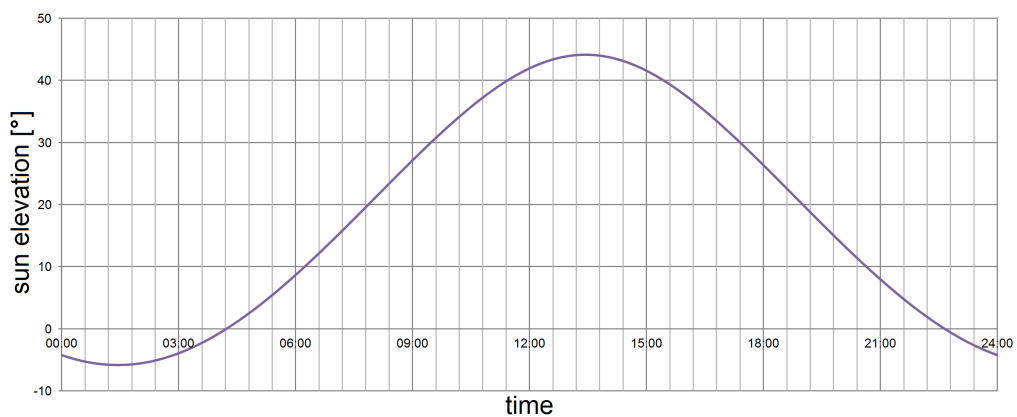


Figure 66: Sun elevation angle (α), whole day

As in the case of PV installations on the roof of houses, it is advisable to orientate the PV installation on top of a vehicle towards the south. However, due to the non-linear curved shape of the roof, this orientation brings more sunlight to the front rows and less sunlight to the rows in the back. Figure 67 illustrates the new calculated effective area ($A_{eff,new}$) if $\psi = 180^\circ$ (vehicle is oriented towards the south), while Figure 68 shows $A_{eff,new}$ at $\psi = 0^\circ$ (vehicle is oriented towards the north). It can be seen that effective areas differ considerably at noon. Usually, the sun azimuth (α) is 180° at noon, however, daylight saving time (DST) in July shifts this angle by one hour.

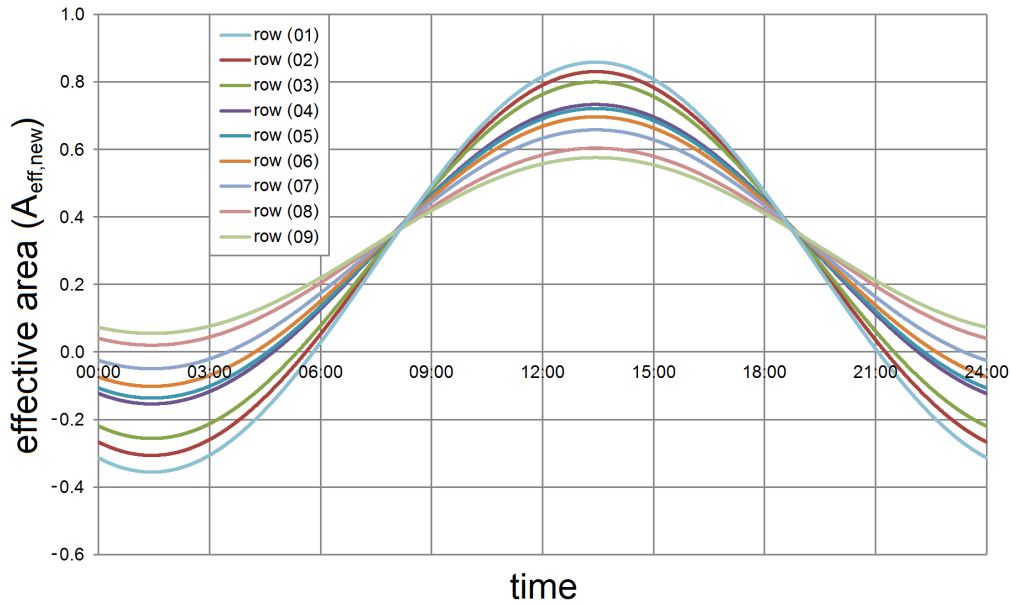


Figure 67: New calculated effective area ($A_{eff,new}$) with $\psi = 180^\circ$, whole day

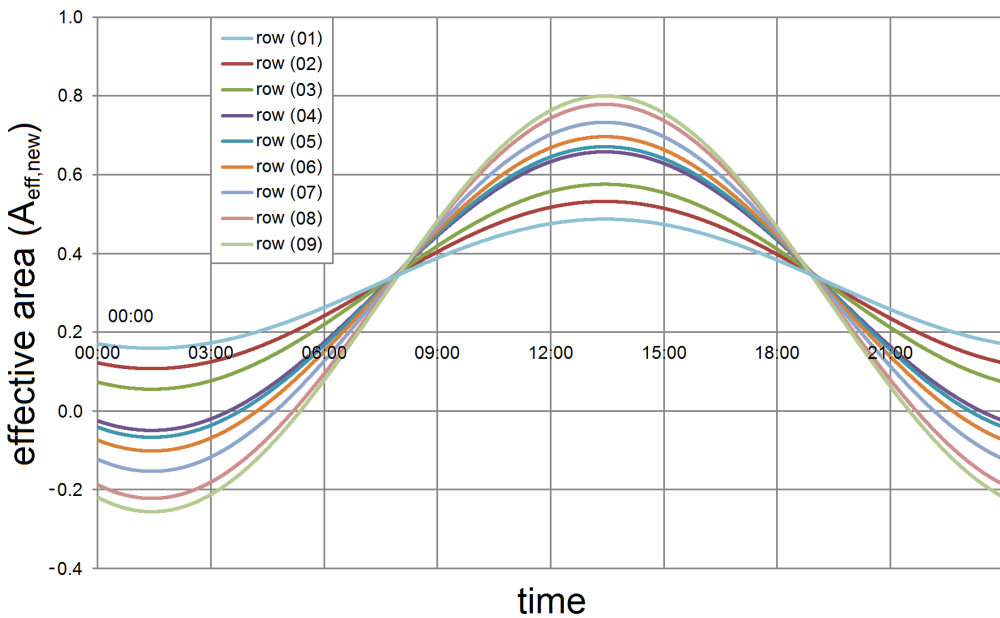


Figure 68: New calculated effective area ($A_{eff,new}$) with $\psi = 0^\circ$, whole day

Figure 69 illustrates $A_{eff,new}$ at $\psi = 90^\circ$ (when the vehicle's orientation is towards the east), and Figure 70 presents $A_{eff,new}$ at $\psi = 270^\circ$ (if the vehicle is oriented towards the west). It can be seen that the circumstances at these angles are comparable, however, effective areas are lower than at a vehicle's orientation towards the south.

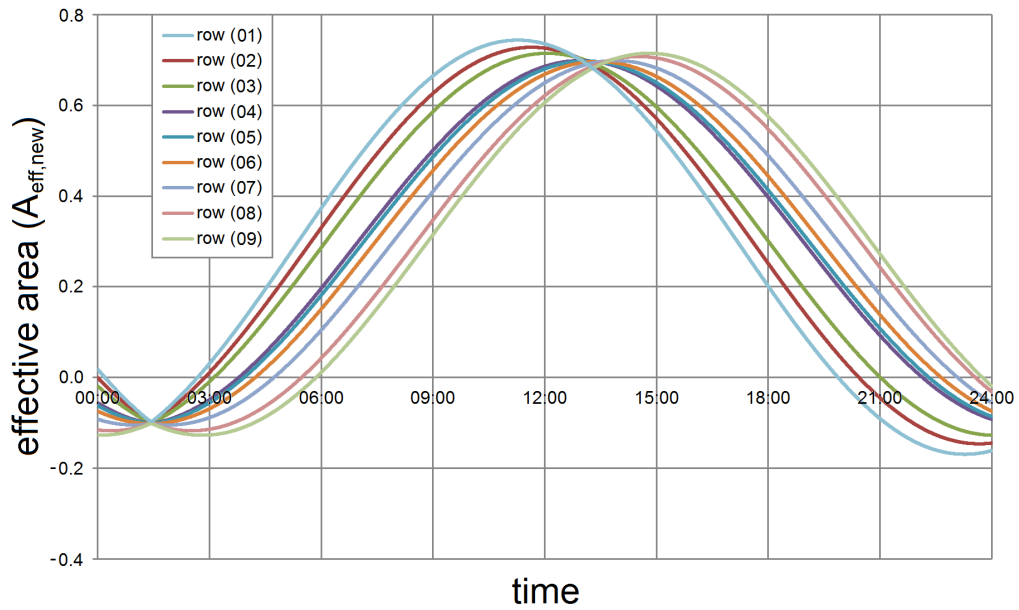


Figure 69: New calculated effective area ($A_{eff,new}$) with $\psi = 90^\circ$, whole day

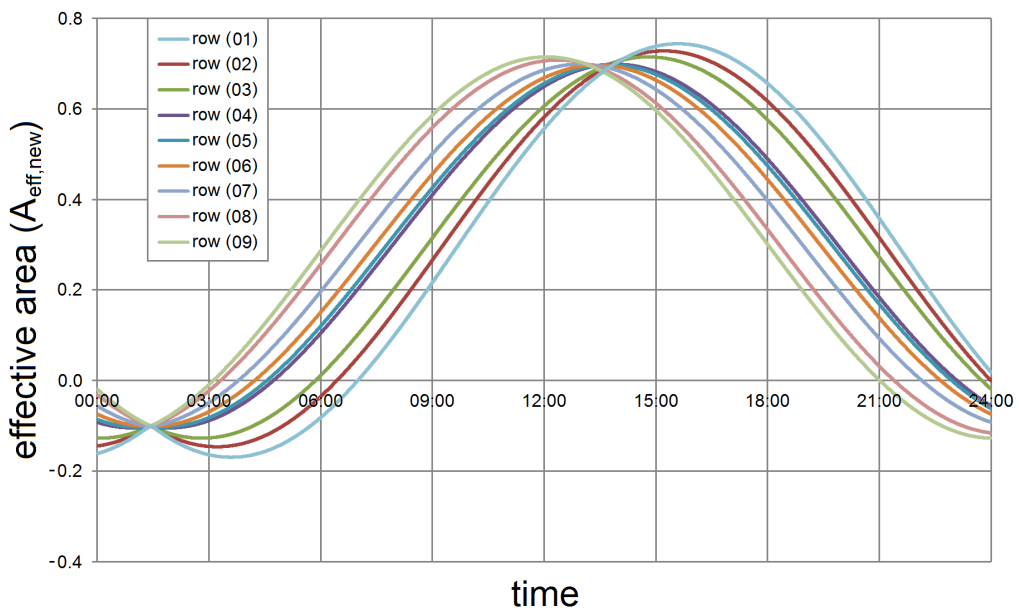


Figure 70: New calculated effective area ($A_{eff,new}$) with $\psi = 270^\circ$, whole day

In the following step, the amount of power is calculated which can be gathered by the PV installation during the whole day. Here, four different cardinal directions for the vehicle (south: $\psi = 180^\circ$; north: $\psi = 0^\circ$; east: $\psi = 90^\circ$; west: $\psi = 270^\circ$) are considered. The amount of power in the MPP (P_{mpp}) was calculated before for the PV cell in row number (06) in which $\beta = 0^\circ$. Here, variations in effective areas ($\Delta A_{eff,new}$ [%]) are calculated which provide an indication in the amount of power from PV cells in different rows, compared with the effective area in row number (06). Figure 72 presents the calculated output power in the MPP of PV cells in different rows.

$$\Delta A_{eff,new} = (A_{eff,new,i} - A_{eff,new,(06)}) \times 100 \quad \text{whereas } i = (01), (02), \dots, (09) \quad (35)$$

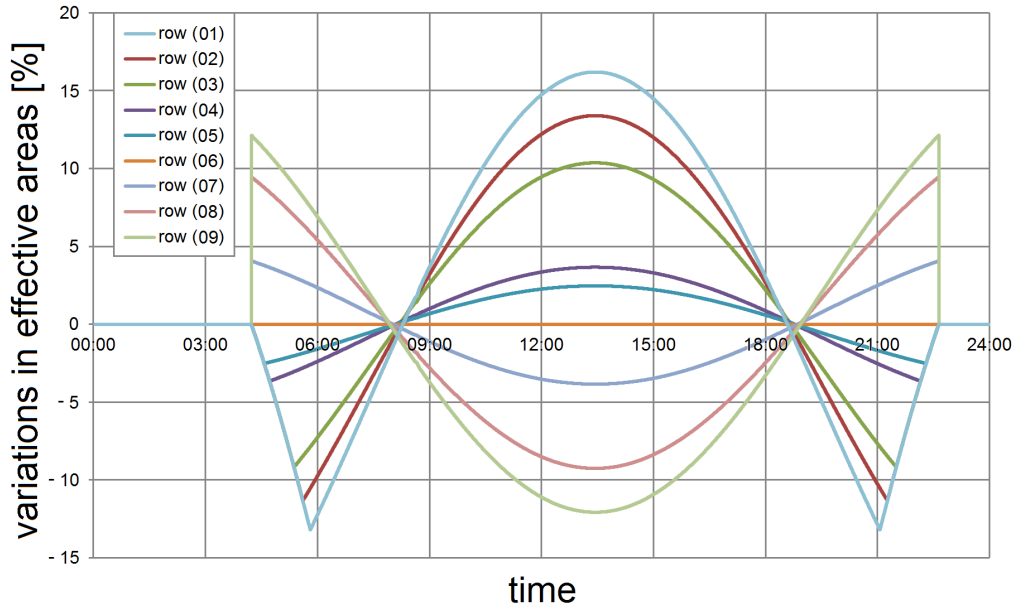


Figure 71: Variations in effective areas [%], whole day

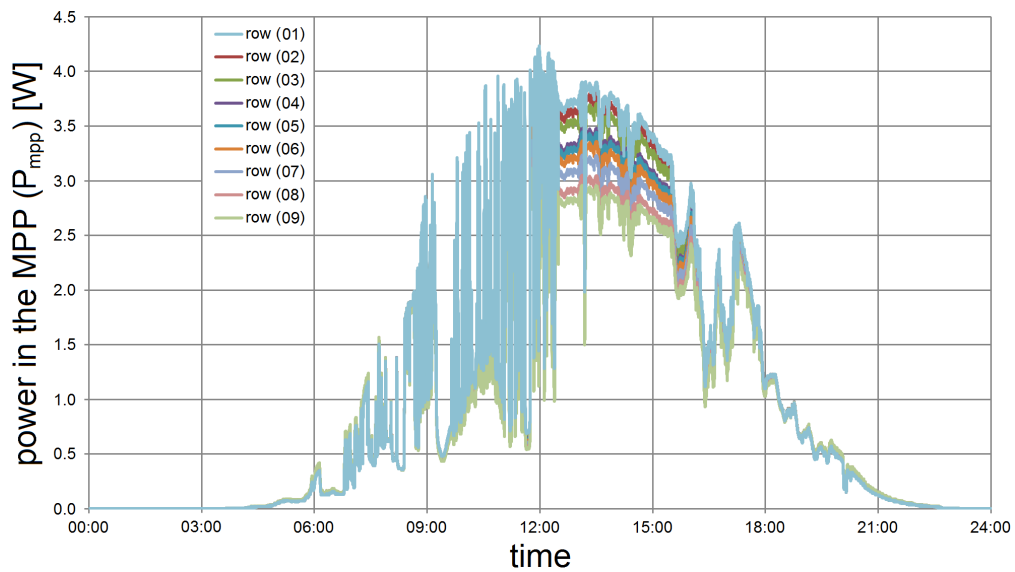


Figure 72: Output power of PV cells in different rows, whole day

The output power of PV modules can be calculated if the amount of power in the MPP (P_{mpp}) of PV cells in different rows is known. Here, the focus lies on the chosen alignment of system structures on top of the experimental vehicle. As mentioned before, in a series connection of PV cells, the weakest PV cell of the interconnection determines the output current (Chapter 4.7.4). At first, the available energy of PV modules is calculated without these considerations. Afterwards, the values are recalculated by taking the negative impacts of PV cells with a lower amount of sunlight into account.

$\psi = 180^\circ$ (south)	uncorrected	
PV module 1:	$E_{mpp,module1}$	= 0.2218 kWh
PV module 2:	$E_{mpp,module2}$	= 0.2373 kWh
PV module 3:	$E_{mpp,module3}$	= 0.2217 kWh
PV module 4:	$E_{mpp,module4}$	= 0.2065 kWh
PV module 5:	$E_{mpp,module5}$	= 0.2218 kWh
all PV modules:	$E_{mpp,total}$	= 1.1092 kWh

$\psi = 180^\circ$ (south)	corrected	
PV module 1:	$E_{mpp,module1}$	= 0.1994 kWh
PV module 2:	$E_{mpp,module1}$	= 0.2328 kWh
PV module 3:	$E_{mpp,module1}$	= 0.2185 kWh
PV module 4:	$E_{mpp,module1}$	= 0.2007 kWh
PV module 5:	$E_{mpp,module1}$	= 0.1994 kWh
all PV modules:	$E_{mpp,total}$	= 1.0508 kWh

$\psi = 0^\circ$ (north)	uncorrected	
PV module 1:	$E_{mpp,module1}$	= 0.2131 kWh
PV module 2:	$E_{mpp,module1}$	= 0.1945 kWh
PV module 3:	$E_{mpp,module1}$	= 0.2157 kWh
PV module 4:	$E_{mpp,module1}$	= 0.2292 kWh
PV module 5:	$E_{mpp,module1}$	= 0.2131 kWh
all PV modules:	$E_{mpp,total}$	= 1.0656 kWh

$\psi = 0^\circ$ (north)	corrected	
PV module 1:	$E_{mpp,module1}$	= 0.1862 kWh
PV module 2:	$E_{mpp,module1}$	= 0.1875 kWh
PV module 3:	$E_{mpp,module1}$	= 0.2130 kWh
PV module 4:	$E_{mpp,module1}$	= 0.2235 kWh
PV module 5:	$E_{mpp,module1}$	= 0.1862 kWh
all PV modules:	$E_{mpp,total}$	= 0.9963 kWh

$\psi = 90^\circ$ (east)	uncorrected	
PV module 1:	$E_{mpp,module1}$	= 0.2171 kWh
PV module 2:	$E_{mpp,module1}$	= 0.2142 kWh
PV module 3:	$E_{mpp,module1}$	= 0.2184 kWh
PV module 4:	$E_{mpp,module1}$	= 0.2188 kWh
PV module 5:	$E_{mpp,module1}$	= 0.2171 kWh
all PV modules:	$E_{mpp,total}$	= 1.0857 kWh
$\psi = 90^\circ$ (east)	corrected	
PV module 1:	$E_{mpp,module1}$	= 0.1928 kWh
PV module 2:	$E_{mpp,module1}$	= 0.2084 kWh
PV module 3:	$E_{mpp,module1}$	= 0.2156 kWh
PV module 4:	$E_{mpp,module1}$	= 0.2131 kWh
PV module 5:	$E_{mpp,module1}$	= 0.1928 kWh
all PV modules:	$E_{mpp,total}$	= 1.0226 kWh
$\psi = 270^\circ$ (west)	uncorrected	
PV module 1:	$E_{mpp,module1}$	= 0.2179 kWh
PV module 2:	$E_{mpp,module1}$	= 0.2178 kWh
PV module 3:	$E_{mpp,module1}$	= 0.2189 kWh
PV module 4:	$E_{mpp,module1}$	= 0.2169 kWh
PV module 5:	$E_{mpp,module1}$	= 0.2179 kWh
all PV modules:	$E_{mpp,total}$	= 1.0894 kWh
$\psi = 270^\circ$ (west)	corrected	
PV module 1:	$E_{mpp,module1}$	= 0.1938 kWh
PV module 2:	$E_{mpp,module1}$	= 0.2122 kWh
PV module 3:	$E_{mpp,module1}$	= 0.2160 kWh
PV module 4:	$E_{mpp,module1}$	= 0.2112 kWh
PV module 5:	$E_{mpp,module1}$	= 0.1938 kWh
all PV modules:	$E_{mpp,total}$	= 1.0271 kWh

It can be seen that the highest amount of power can be obtained if the vehicle is oriented towards the south. In other directions, the output power of the PV installation is lowered by up to 5 %. However, it is worth noting that output performances can be improved if the cardinal direction of the vehicle's orientation is changed during the day towards the current position of the sun. Hence, the information on the current sun azimuth (θ) can be useful to improve the output power of photovoltaics.

5.2.4 Impact of Different Ways of Aligning PV Modules

Here, possible variations in output performances are analysed on the example of three different ways of aligning PV modules on the roof of the Toyota Prius. Configuration (a) is similar to the chosen alignment of PV cells on top of the experimental vehicle, while in configuration (b) and (c) all PV modules are similar, but aligned differently. It is worth noting that due to the total amount of 60 PV cells, more PV cells are connected with each other than on the experimental vehicle. In the following steps, each time the total available output energy ($V_{opl} = V_{mpp}$) is calculated which can be obtained from each particular type of configuration.

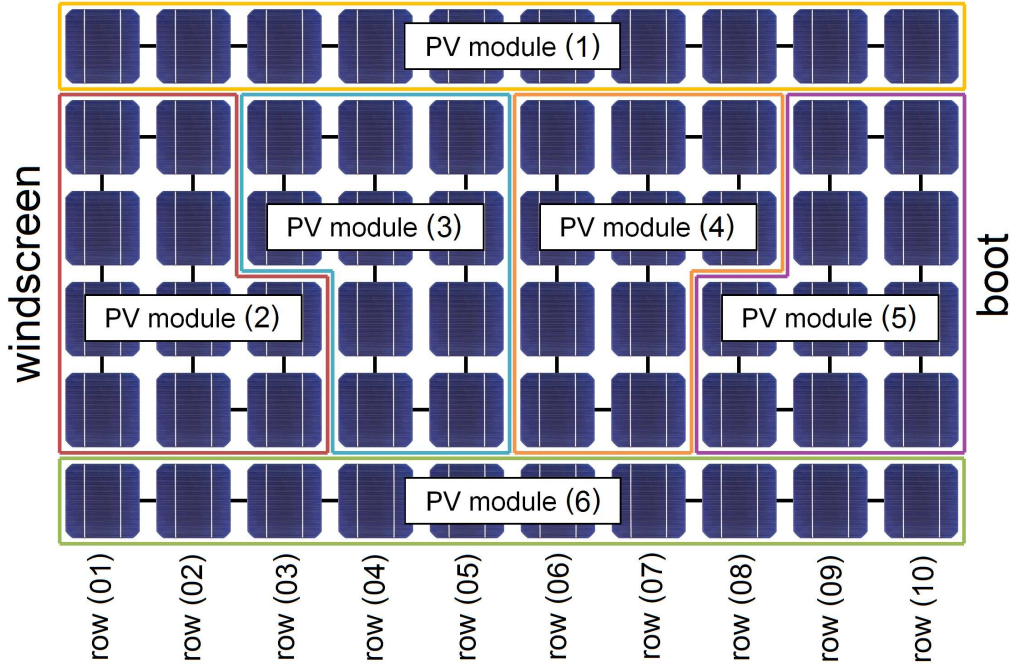


Figure 73: Different alignments of PV modules, configuration (a)

$\psi = 180^\circ$ (south)	corrected	
PV module 1:	$E_{mpp,module1}$	$= 0.2166 \text{ kWh}$
PV module 2:	$E_{mpp,module2}$	$= 0.2587 \text{ kWh}$
PV module 3:	$E_{mpp,module3}$	$= 0.2464 \text{ kWh}$
PV module 4:	$E_{mpp,module4}$	$= 0.2276 \text{ kWh}$
PV module 5:	$E_{mpp,module5}$	$= 0.2184 \text{ kWh}$
PV module 6:	$E_{mpp,module6}$	$= 0.2166 \text{ kWh}$
all PV modules:	$E_{mpp,total}$	$= 1.3842 \text{ kWh}$

In system configuration (b), 12 PV cells are connected with each other to establish one PV module. As a result, five instead of six PV modules are formed on top of the Toyota Prius. Here, PV cells in modules have a similar orientation towards the sun to fulfil the requirements on the input voltage of the dc/dc converter. In contrast to this configuration with PV modules vertically, PV modules in configuration (c) are aligned horizontally so that the difference in orientation ($\Delta\beta$) is the highest one (Chapter 4.5).

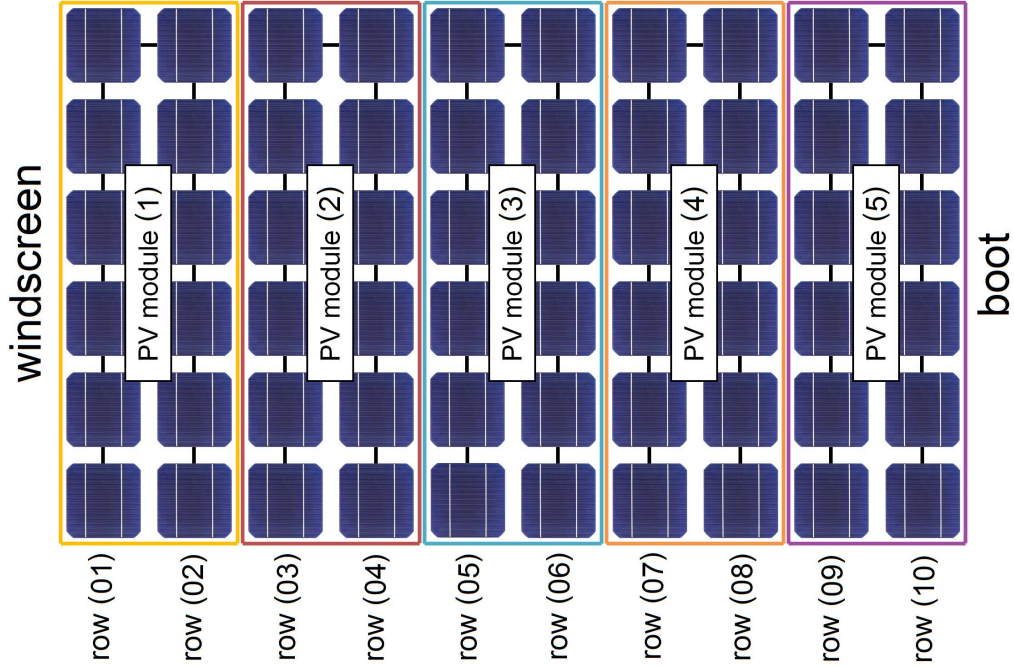


Figure 74: Different alignments of PV modules, configuration (b)

$\psi = 180^\circ$ (south)	corrected	
PV module 1:	$E_{mpp,module1}$	= 0.3163 kWh
PV module 2:	$E_{mpp,module2}$	= 0.2980 kWh
PV module 3:	$E_{mpp,module3}$	= 0.2915 kWh
PV module 4:	$E_{mpp,module4}$	= 0.2733 kWh
PV module 5:	$E_{mpp,module5}$	= 0.2622 kWh
all PV modules:	$E_{mpp,total}$	= 1.4413 kWh

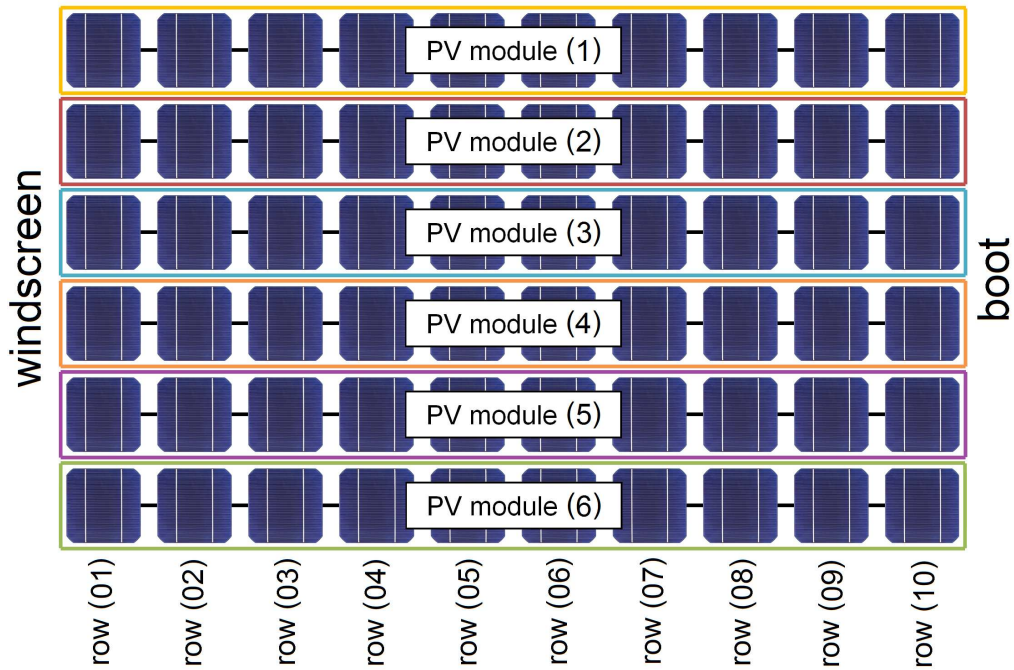


Figure 75: Different alignments of PV modules, configuration (c)

$\psi = 180^\circ$ (south)	corrected	
PV module 1:	$E_{mpp,module1}$	$= 0.2166 \text{ kWh}$
PV module 2:	$E_{mpp,module2}$	$= 0.2166 \text{ kWh}$
PV module 3:	$E_{mpp,module3}$	$= 0.2166 \text{ kWh}$
PV module 4:	$E_{mpp,module4}$	$= 0.2166 \text{ kWh}$
PV module 5:	$E_{mpp,module5}$	$= 0.2166 \text{ kWh}$
PV module 6:	$E_{mpp,module6}$	$= 0.2166 \text{ kWh}$
all PV modules:	$E_{mpp,total}$	$= 1.2996 \text{ kWh}$

If all PV cells are connected in parallel with each other, negative impacts of series connections can be avoided. However, in this case, the amount of wiring is significantly increased and the output voltage level is low (Chapter 4.7.3). $E_{mpp,total} = 1.4768 \text{ kWh}$ with all PV cells in parallel ($\psi = 180^\circ$). Compared to this output, the variation in power of different configurations can be calculated. It is seen that the difference in output power between all PV cells in parallel and configuration (b) is about 2 %.

$\psi = 180^\circ$ (south)	corrected	
all PV modules in configuration (a):		$- 6.27 \%$
all PV modules in configuration (b):		$- 2.40 \%$
all PV modules in configuration (c):		$- 12.00 \%$

5.2.5 Impacts on the Estimation of the Output Power

The calculations and considerations presented here are a way of estimating the amount of solar energy which can be produced on today's HEVs and BEVs. It is worth noting that the amount of available power from photovoltaics depends strongly on the geographical location of photovoltaics. In this section, there are four more factors discussed which have an impact on the results of calculations.

- Temperature of the PV cell (T_c)

In previous calculations, it was assumed that all PV cells operate at the same temperature as the PV cell with $\beta = 0^\circ$ (PV cell in row number (06) of the experimental vehicle). In reality, PV cells in different rows with different orientation angles operate at different temperature levels. T_c of individual PV cells varies in the order of a few degree Kelvin at $\alpha = 43^\circ$, as seen in Table 33. Additionally, differences in effective areas (ε_{area} [%]) are calculated at this sun elevation compared with the available effective area in row number (06). Figure 76 illustrates variation in output powers at different temperature levels if $\beta = 0^\circ$. Table 34 summarises variations in maximum output powers (ε_{power} [%]). It can be seen that the increase in effective area which is proportional to an increase in power (Chapter 4.6.5) outweighs the negative impacts of higher temperature of PV cells.

Table 33: Different temperatures of PV cells in different rows

	β	T_c	ε_{area}
row (01)	15 °	296.0 K	+ 24.35 %
row (02)	12 °	295.7 K	+ 18.62 %
row (03)	9 °	294.0 K	+ 15.54 %
row (04)	3 °	293.4 K	+ 5.48 %
row (05)	2 °	293.0 K	+ 3.68 %
row (06)	0 °	292.4 K	± 0.00 %
row (07)	- 3 °	291.4 K	- 7.72 %
row (08)	- 7 °	290.9 K	- 15.90 %
row (09)	- 9 °	290.1 K	- 20.14 %

Table 34: Variation in output power in the MPP at different PV cell temperatures

T_c	ε_{power}
296.0 K	- 1.37 %
295.7 K	- 1.25 %
294.0 K	- 0.66 %
293.4 K	- 0.39 %
293.0 K	- 0.22 %
292.4 K	± 0.00 %
291.4 K	+ 0.44 %
290.9 K	+ 0.63 %
290.1 K	+ 0.92 %

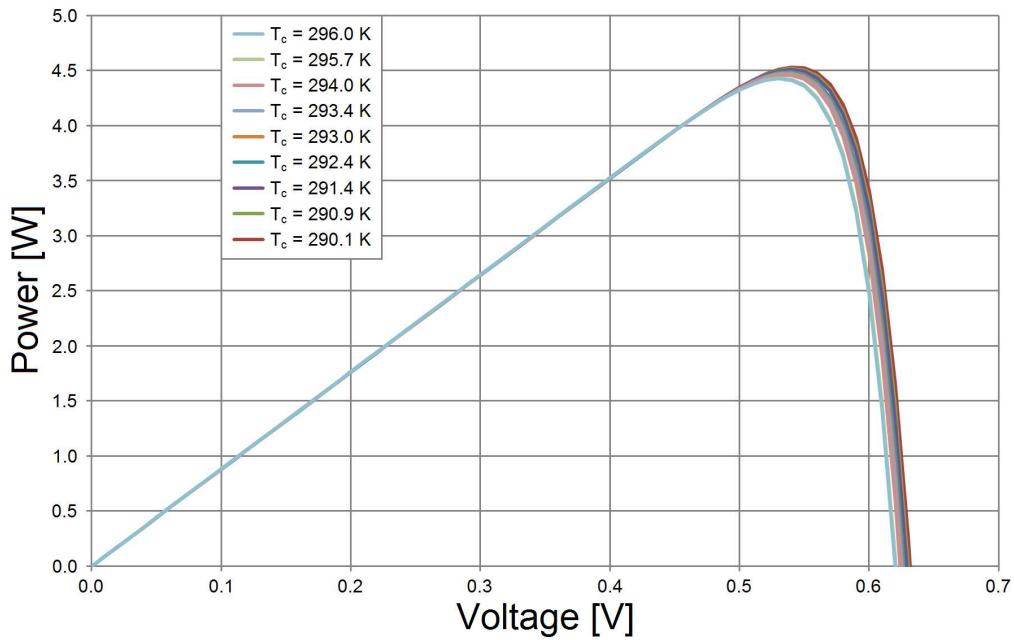


Figure 76: P-V curve of one PV cell at different temperatures

- Impact of Weather Conditions

In the presented calculations, the ambient conditions during a partly cloudy, partly sunny day were taken into account. If the sky had been clear, about 20 % more solar energy would have been gained. However, if it had been a predominantly cloudy day, the amount of output power would have been about 30 % lower. Weather conditions change from day to day and so does the amount of output of photovoltaics (Chapter 3.2).

Changes in ambient conditions also influence the efficiency of MPPT techniques (Chapter 3.4.4). In the calculations, the operating voltage (V_{op}) was always equal to the voltage in the MPP (V_{mp}). In reality, the amount of power will be reduced, even though a MPP tracker (η_{MPPT}) is used (Chapter 3 and Chapter 4.8). The variation in output power is expected in the order of 1–2 % and can increase significantly in dynamic environmental conditions (Chapter 4.8.4).

5.2.6 Use of the Solar Energy in HEVs and BEVs

On top of the Toyota Prius, an electrical power of about 200 Watt-Peak can be produced around noon. As stated in Chapter 2.1, an electrical power of 1 kW from the alternator is equal to about one litre of gasoline. This means that an electrical power of 100 W requires about 0.1 litre of fuel. If the possibility would be available to use the solar energy directly within the on-board power supply, about 0.2 litres on fuel consumption could be saved during driving in urban and residential areas. If the fuel consumption is reduced by 0.1 litres per 100 kilometres, about 2.32 g/km on CO₂-emissions can be saved (Chapter 1 and Chapter 2).

For pure-electric propulsion, on average 0.19 kWh per kilometre are required. Based on this assumption, the opportunity is given to estimate the all-electric driving range of HEVs and BEVs with the energy of photovoltaics for the example day. Here, the losses for charging the high-voltage battery ($\eta_{bat} \approx 0.8$ and $\eta_{dc/dc} \approx 0.85$) have to be taken into account (Chapter 4.2). In Table 35, the estimated all-electric driving range for the different HEVs and BEVs in this investigation are presented. The additional all-electric driving range with the help of solar energy can be estimated to be in the order of 3–6 kilometres per day for today's HEVs and BEVs.

Table 35: Comparison of additional all-electric driving distances for HEVs and BEVs

	Toyota Prius	Toyota Auris	Nissan Leaf	Citroën C-Zero
$\Delta\beta$	26 °	23 °	18 °	23 °
P_{th}	316 W	368 W	264 W	285 W
P_{mpp}	248 W	273 W	207 W	224 W
n_{cells}	60	66	50	54
$E_{mpp,total}$	1.46 kWh	1.62 kWh	1.20 kWh	1.41 kWh
driving range	5.2 km	5.8 km	4.3 km	5.0 km

6 Conclusion

The roof of today's BEVs and HEVs is not designed to install PV cells which are available on the current market. It is difficult to optimise the use of the area due to the fixed size of one PV cell. This situation results in different amount of PV cells per m^2 . Moreover, the non-linear curved shape of the roof does not support solar energy production. Instead, it complicates the establishment of system structures and causes the current to drop to the amount which can be gained from the weakest PV cell of the interconnection. It is crucial to optimise the limited area on top of BEVs and HEVs for solar energy production. As a result, a significant contribution to the required amount of electricity can be established. In this way, PV installation can function as an ERE and prolong the pure-electric driving distance. In the case of HEVs, fuel consumption can be reduced and emissions can be lowered.

The calculated normalised effective area of photovoltaics can be used to estimate the output power from any PV installation which is mounted to curved surfaces. The monitoring system offers an opportunity to collect data for statistical evaluations and improve the performance of photovoltaics. Therefore, additional hardware needs to be installed with the PV cells. The findings of this work are helpful to predict the output performance of photovoltaics under static and dynamic environmental conditions. Due to the numerous MPPT strategies, it is non-trivial to verify the impact on the performance of MPP trackers. Based on the high alternation rate of the solar radiation level, the degree of efficiency of the (η_{MPPT}) is expected to be lower during driving conditions compared when the vehicle is parked.

In future work, a more complex simulator will be programmed which is based on current PV simulation models and which considers the circumstances of photovoltaics within automobiles. Thus, it is possible to identify how much either the auxiliary or high-voltage battery can be charged exactly during a given period of time. Ideally, the simulation tool will also characterise parameters of MPPT algorithms. One suggestion is the use of one MPPT strategy for when the vehicle is in parked conditions, and another, modified MPPT technique for driving conditions. Overall, my diploma thesis indicated that automobiles represent a new environment for photovoltaics and several questions needed to be addressed for efficient solar energy production. This work successfully provided further details to answer these questions to make solar energy production feasible on top of BEVs and HEVs.

References

- [1] C. Schuss. *Improvement of the efficiency of an electric car by the use of electronics*. Diploma thesis, Graz University of Technology, 2010.
- [2] D.P. van Vuuren, N. Nakicenovic, K. Riahi, A. Brew-Hammond, D. Kammen, V. Modi, and K.R. Smith. An energy vision: the transformation towards sustainability - interconnected challenges and solutions. *Current Opinion in Environmental Sustainability*, 4(1):18–34, 2012.
- [3] J.M. Pearce. Photovoltaics - a path to sustainable futures. *Futures*, 34(7):663–674, 2002.
- [4] K.T. Chau and Y.S. Wong. Overview of power management in hybrid electric vehicles. *Energy Conversion and Management*, 43(15):1953–1968, 2002.
- [5] C. Schuss, B. Eichberger, and T. Rahkonen. A Monitoring System for the Use of Solar Energy in Electric and Hybrid Electric Vehicles. *Proceedings of the IEEE International Instrumentation and Measurement Technology Conference (I2MTC)*, pages 524–527, 2012.
- [6] E. Karden, S. Ploumen, B. Fricke, T. Miller, and K. Snyder. Energy storage devices for future hybrid electric vehicles. *Journal of Power Sources*, 168(1):2–11, 2007.
- [7] M.A. Hussin, A.N. Abdalla, R. Ishak, R. Abdullah, and Z.M. Ali. Study on Improving Electric Vehicle drive range using Solar Energy. *International Conference on Electrical, Control and Computer Engineering (InECCE)*, pages 373–376, 2011.
- [8] C. Schuss, H. Gall, K. Eberhart, H. Illko, and B. Eichberger. Alignment and Interconnection of Photovoltaics on Electric and Hybrid Electric Vehicles. *Proceedings of the IEEE International Instrumentation and Measurement Technology Conference (I2MTC)*, pages 153–158, 2014.
- [9] S. Küppers and G. Henneberger. Numerical Procedures for the Calculation and Design of Automotive Alternators. *IEEE Transactions on Magnetics*, 33(2):2022–2025, 1997.
- [10] A. Gimeno, G. Friedrich, and K. El-Kadri-Benkara. Experimental and numerical evaluation of iron losses in a claw pole car generator. *XIX International Conference on Electrical Machines (ICEM)*, pages 1–6, 2010.
- [11] P. Bolund and S. Hunhammar. Ecosystem services in urban areas. *Ecological Economics*, 29(2):293–301, 1999.
- [12] S. Yu, G. Dong, and L. Li. Transient characteristics of emissions during engine start/stop operation employing a conventional gasoline engine for hev application. *International Journal of Automotive Technology*, 9(5):543–549, 2008.
- [13] G. Haughton and C. Hunter. *Sustainable Cities (Regional Policy and Development)*. Jessica Kingsley, London, 1st edition, 1994.
- [14] L. E. Jackson. The relationship of urban design to human health and condition. *Landscape and Urban Planning*, 64(4):191–200, 2003.
- [15] C. Schuss, B. Eichberger, and T. Rahkonen. Measurement and Verification of Photovoltaic (PV) Simulation Models. *Proceedings of the IEEE International Instrumentation and Measurement Technology Conference (I2MTC)*, pages 188–193, 2013.

- [16] G. Leen and D. Heffernan. Expanding Automotive Electronic Systems. *Computer*, 35(1):88–93, 2002.
- [17] R. Bosch GmbH. *Automotive Electrics and Automotive Electronics: Systems and Components: Networking, Hybrid Drive*. Vieweg and Teubner, Wiesbaden, 5th edition, 2007.
- [18] A. Monot, N. Navet, B. Bavoux, and F. Simonot-Lion. Multisource Software on Multicore Automotive ECUs – Combining Runnable Sequencing With Task Scheduling. *IEEE Transactions on Industrial Electronics*, 59(10):3934–3942, 2012.
- [19] N. Navet, A. Monot, B. Bavoux, and F. Simonot-Lion. Multi-source and multicore automotive ECUs - OS protection mechanisms and scheduling. *IEEE International Symposium on Industrial Electronics (ISIE)*, pages 3734–3741, 2010.
- [20] P. Thoma. Future needs for automotive electronics. *IEEE International Conference on Computer Design: VLSI in Computers and Processors*, pages 532–539, 1994.
- [21] N. Yoshimatsu, T. Antoine, T. Kando, and K. Murakam. A Dynamic Reconfigurable Processor and a Design Tool for Next Generation ECUs. *International SOC Design Conference (ISoCC)*, pages 388–391, 2009.
- [22] A. Emadi, Y.J. Lee, and K. Rajashekara. Power Electronics and Motor Devices in Electric, Hybrid, and Plug-In Hybrid Electric Vehicles. *IEEE Transactions on Industrial Electronics*, 55(6):2237–2245, 2008.
- [23] F.L. Mapelli, D. Tarsitano, and M. Mauri. Plug-In Hybrid Electric Vehicle: Modeling, Prototype Realization, and Inverter Losses Reduction Analysis. *IEEE Transactions on Industrial Electronics*, 57(2):598–607, 2010.
- [24] D.-J. Kim, K.-H. Park, and Z. Bien. Hierarchical Longitudinal Controller for Rear-End Collision Avoidance. *IEEE Transactions on Industrial Electronics*, 54(2):805–817, 2007.
- [25] T. Bücher, C. Curio, J. Edelbrunner, C. Igel, D. Kastrup, I. Leefken, G. Lorenz, A. Steinhage, and W. von Seelen. Image Processing and Behavior Planning for Intelligent Vehicles. *IEEE Transactions on Industrial Electronics*, 50(1):62–75, 2003.
- [26] K. Çağatay Bayindir, M.A. Gözükcüçük, and A. Teke. A comprehensive overview of hybrid electric vehicle: Powertrain configurations, powertrain control techniques and electronic control units. *Energy Conversion and Management*, 52(2):1305–1313, 2006.
- [27] M. Broy, I.H. Krüger, A. Pretschner, and C. Salzmann. Engineering Automotive Software. *Proceedings of the IEEE*, 95(2):356–373, 2007.
- [28] C.C. Chan. The State of the Art of Electric, Hybrid, and Fuel Cell Vehicles. *Proceedings of the IEEE*, 95(4):704–718, 2007.
- [29] M. Schöllmann, C. Hoff, and J. Schriek. *Energiemanagement und Bordnetze 3: Innovative Ansätze für modernes Energiemanagement und zuverlässige Bordnetzarchitekturen*. Expert-Verlag, Renningen, 1st edition, 2009. [in German].
- [30] C.C. Chan. Powering Sustainable Mobility: Roadmaps of Electric, Hybrid, and Fuel Cell Vehicles. *Proceedings of the IEEE*, 97(4):603–607, 2009.
- [31] H. Hanselmann. Automotive Control: From Concept to Experiment to Product. *Proceedings of the IEEE International Symposium on Computer-Aided Control System Design*, pages 129–134, 1996.

- [32] J.T.B.A. Kessels, M.W.T. Koot, P.P.J. van den Bosch, and D.B. Kok. Online Energy Management for Hybrid Electric Vehicles. *IEEE Transactions on Vehicular Technology*, 57(6):3428–3440, 2008.
- [33] C.C. Chan, A. Bouscayrol, and K. Chen. Electric, Hybrid, and Fuel-Cell Vehicles: Architectures and Modeling. *IEEE Transactions on Vehicular Technology*, 59(2): 589–598, 2010.
- [34] L.T. Lam, R. Louey, N.P. Haigh, O.V. Lim, D.G. Vella, C.G. Phyland, L.H. Vu, J. Furukawa, T. Takada, D. Monma, and T. Kano. VRLA Ultrabattery for high-rate partial-state-of-charge operation. *Journal of Power Sources*, 174(1):16–29, 2007.
- [35] M. Schöllmann. *Energiemanagement und Bordnetze 2: Innovative Ansätze für modernes Energiemanagement und zuverlässige Bordnetzarchitekturen*. Expert-Verlag, Renningen, 1st edition, 2007. [in German].
- [36] M. Anderman. The challenge to fulfill electrical power requirements of advanced vehicles. *Journal of Power Sources*, 127(1–2):2–7, 2004.
- [37] E. Karden, P. Shinn, P. Bostock, J. Cunningham, E. Schoultz, and D. Kok. Requirements for future automotive batteries - A snapshot. *Journal of Power Sources*, 144(2):505–512, 2005.
- [38] B. Spier and G. Gutmann. 42-V battery requirements - lead-acid at its limits. *Journal of Power Sources*, 116(1–2):99–104, 2003.
- [39] K. Borgeest. *Elektronik in der Fahrzeugtechnik*. Vieweg und Teubner, Wiesbaden, 2nd edition, 2010. [in German].
- [40] P. Thounthong, S. Rael, and B. Davat. Energy management of fuel cell/battery/supercapacitor hybrid power source for vehicle applications. *Journal of Power Sources*, 193(1):376–385, 2009.
- [41] I. Husain. *Electric and Hybrid Vehicles: Design Fundamentals*. CRC press, Boca Raton, Florida, 2nd edition, 2011.
- [42] K.E. Aifantis, S.A. Hackney, and R.V. Kumar. *High Energy Density Lithium Batteries: Materials, Engineering, Applications*. Wiley-VCH Verlag GmbH & Co. KGaA, Weinheim, 1st edition, 2010.
- [43] A.S. Tannenbaum. *Computer Networks*. Prentice-Hall PTR, Boston, Massachusetts, 5th edition, 2010.
- [44] N. Navet, Y. Song, F. Simonot-Lion, and C. Wilwert. Trends in Automotive Communication Systems. *Proceedings of the IEEE*, 93(6):1204–1222, 2005.
- [45] F. Li, L. Wang, and C. Liao. CAN(Controller Area Network) Bus Communication System Based on Matlab/Simulink. *IEEE International Conference on Wireless Communications, Networking and Mobile Computing (WiCOM)*, pages 1–4, 2008.
- [46] R. Hedge and K.S. Gurumurthy. Load Balancing Across ECUs in Automotives. *International Conference on Communication Software and Networks (ICCSN)*, pages 404–408, 2009.
- [47] F. Zhang and S.T. Chanson. Power-Aware Processor Scheduling under Average Delay Constraints. *11th IEEE Real-Time and Embedded Technology and Applications Symposium (RTAS)*, pages 202–212, 2005.

- [48] T. Gustafsson and J. Hansson. Data Management in Real-Time Systems: a Case of On-Demand Updates in Vehicle Control Systems. *10th IEEE Real-Time and Embedded Technology and Applications Symposium (RTAS)*, pages 182–191, 2004.
- [49] Q.N. Ahmed and S.V. Vrbsky. Triggered Updates for Temporal Consistency in Real-Time Databases. *Real-Time systems*, 19(3):209–243, 2000.
- [50] C. Alippi and C. Galperti. An Adaptive System for Optimal Solar Energy Harvesting in Wireless Sensor Network Nodes. *IEEE Transactions on Circuits and Systems I: Regular Papers*, 55(6):1742–1750, 2008.
- [51] V. Raghunathan, A. Kansal, J. Hsu, J. Friedman, and M. Srivastava. Design considerations for solar energy harvesting wireless embedded systems. *Proceedings of the 4th International Symposium on Information Processing in Sensor Networks*, pages 457–462, 2005.
- [52] R.N. Hall. Silicon Photovoltaic Cells. *Solid State Electronics*, 24(7):595–616, 1981.
- [53] M.A. Green. General solar cell curve factors including the effects of ideality factor, temperature and series resistance. *Solid State Electronics*, 20(3):265–266, 1977.
- [54] Y. Gang and C. Ming. LabVIEW Based Simulation System for the Output Characteristics of PV Cells and the Influence of Internal Resistance on It. *WASE International Conference on Information Engineering (ICIE)*, pages 391–394, 2009.
- [55] T. Esram and P.L. Chapman. Comparison of Photovoltaic Array Maximum Power Point Tracking Techniques. *IEEE Transactions on Energy Conversion*, 22(2):439–449, 2007.
- [56] R. Decher. *Direct Energy Conversion: Fundamentals of Electric Power Production*. Oxford University Press, New York, New York, 1st edition, 1996.
- [57] M.A.S. Masoum, H. Dehbonei, and E.F. Fuchs. Theoretical and Experimental Analysis of Photovoltaic Systems With Voltage- and Current-Based Maximum Power-Point Tracking. *IEEE Transactions on Energy Conversion*, 22(8):514–522, 2002.
- [58] H.-L. Tsai, C.-S. Tu, and Y.-J. Su. Development of Generalized Photovoltaic Model Using MATLAB/SIMULINK. *Proceedings of the World Congress on Engineering and Computer Science (WCECS)*, pages 1–6, 2008.
- [59] J.A. Gow and C.D. Manning. Development of a photovoltaic array model for use in power-electronics simulation studies. *Electric Power Applications, IEE Proceedings*, 146(2):193–200, 1999.
- [60] F. Attivissimo, A. Di Nisio, M. Savino, and M. Spadavecchia. Uncertainty Analysis in Photovoltaic Cell Parameter Estimation. *IEEE Transactions on Instrumentation and Measurement*, 61(5):1334–1342, 2012.
- [61] L. Cristaldi, M. Faifer, A. Ferrero, and A. Nechifor. On-line monitoring of the efficiency of Photo-Voltaic panels for optimizing maintaince scheduling. *Proceedings of the IEEE International Instrumentation and Measurement Technology Conference (I2MTC)*, pages 954–959, 2010.
- [62] L. Cristaldi, M. Faifer, M. Rossi, and F. Ponci. A Simple Photovoltaic Panel Model: Characterization Procedure and Evaluation of the Role of Environmental Measurements. *IEEE Transactions on Instrumentation and Measurement*, 61(10):2632–2641, 2012.

- [63] H.-F. Tsai and H.-L. Tsai. Implementation and verification of integrated thermal and electrical models for commercial PV modules. *Solar Energy*, 86(1):654–665, 2012.
- [64] M.G. Wanzeller, R.N.C. Alves, J.V. da Fonseca Neto, and W.A. dos Santos Fonseca. Current Control Loop for Tracking of Maximum Power Point Supplied for Photovoltaic Array. *IEEE Transactions on Instrumentation and Measurement*, 53(4):1613–1622, 2004.
- [65] F. Adamo, F. Attivissimo, and M. Spadavecchia. A Tool for Photovoltaic Panels Modeling and Testing. *Proceedings of the IEEE International Instrumentation and Measurement Technology Conference (I2MTC)*, pages 1463–1466, 2010.
- [66] F. Adamo, F. Attivissimo, A. Di Nisio, and M. Spadavecchia. Characterization and Testing of a Tool for Photovoltaic Panel Modeling. *IEEE Transactions on Instrumentation and Measurement*, 60(5):1613–1622, 2011.
- [67] R. Ramaprabha, B. Mathur, M. Murthy, and S. Madhumitha. New Configuration of Solar Photo Voltaic Array to Address Partial Shaded Conditions. *3rd International Conference on Emerging Trends in Engineering and Technology (ICETET)*, pages 328–333, 2010.
- [68] I. Aharon and A. Kuperman. Topological Overview of Powertrains for Battery-Powered Vehicles With Range Extenders. *IEEE Transactions on Power Electronics*, 26(3):868–876, 2011.
- [69] M. Ropp, J. Cale, M. Mills-Price, M. Scharf, and S.G. Hummel. A test protocol to enable comparative evaluation of maximum power point trackers under both static and dynamic irradiance. *37th IEEE Photovoltaic Specialists Conference (PVSC)*, pages 3734–3737, 2011.
- [70] R. Bründlinger, N. Henze, H. Häberlin, B. Burger, A. Bergmann, and F. Baumgartner. prEN 50530 - the new European Standard for Performance Characterization of PV Inverters. *24th European Photovoltaic Solar Energy Conference*, pages 1–5, 2009.